Developing multilayer microfluidic platforms and advancing laser induced fluorescent detection and electrochemical detection to analyze intracellular protein kinases, reactive nitrogen and oxygen species in single cells

by

Damith Randika E.W. Patabadige

B.S., University of Colombo, 2006

AN ABSTRACT OF A DISSERTATION

Submitted in partial fulfillment of the requirements for the degree

DOCTOR OF PHILOSOPHY

Department of Chemistry
College of Arts and Sciences

KANSAS STATE UNIVERSITY
Manhattan, Kansas

2017

Abstract

Recent approaches in analytical separations are being advanced towards the "lab-on-a-chip" concept in which multiple lab functions are integrated into micro/nano fluidic platforms. Among the variety of separation techniques that can be implemented on microfluidic devices, capillary electrophoresis is the most popular as it provides high efficiency, simple, fast and low cost separations. In addition, integrating miniaturized fluid manipulation tools into microfluidic devices with separations is essential for a variety of biological applications. Chapter 1 discusses the fundamentals of capillary electrophoresis and miniaturized fluid manipulation tools and provides an over view of single cell analysis in microfluidics.

In chapter 2, the integration of miniaturized peristaltic pumps into multilayer microfluidic platforms is discussed. In addition, device characterization, precise fluid control and high throughput single cell analysis are discussed. As a proof of principle, T-lymphocytes were loaded with two fluorescent probes Carboxyfluorescein diacetate (CFDA) and Oregon green (OG). Thousands of single cells were automatically transported, lysed on these devices and analytes from the lysate were electrophoretically separated. 1120 cells were analyzed over the course of 80 min (14 cells/min) and separation characteristics of analytes released from individual cells were investigated.

In the third chapter, the development of microfluidic platforms for the electrochemical detection of nitric oxide (NO) and other reactive nitrogen species (RNS) at the single cell level is discussed. A microfluidic system was developed to perform rapid cell lysis followed by electrochemical detection. Miniaturized microband electrodes were designed and integrated with a microfluidic separation channel. Three alignment techniques (in-channel, end-channel and off-channel configurations) were used to detect the electrochemical response of the analyte of interest.

Furthermore, a model analyte (CFDA) was used to demonstrate the potential of performing the simultaneous dual detection with electrochemical and laser induced fluorescence detection. In addition, the same microfluidic platform was adapted to detect intracellular superoxide using laser induced fluorescence.

In the fourth chapter, the off-chip integration of optical fiber bridges with multilayer microfluidic chips is discussed. A multimode optical fiber (~10cm long) was integrated between the single cell lysing spot and a spot downstream of the separation channel in order to detect both intact cells and the analyte in the lysate. This technique was used to create two detection spots on the microfluidic platform with the use of a single excitation source and single detector. Fluorescently labeled T-lymphocytes were automatically transported and lysed in a manner similar to that described in chapter 2. Hundreds of single cells were analyzed and the absolute migration time was determined for the analytes in the lysate. In addition, the separation characteristics of fluorescently labeled protein kinase B peptide substrates were investigated. Furthermore, this technique was used to measure cell size and the velocity of intact cells (discussed in 5^{th} chapter) by making use of a light tunneling concept available in multimode optical fibers.

All the experiments presented in this dissertation exploit the use of multilayer microfluidic platforms to investigate intracellular components in single cells in a high throughput manner that has several advantages over current conventional techniques.

Developing multilayer microfluidic platforms and advancing laser induced fluorescent detection and electrochemical detection to analyze intracellular protein kinases, reactive nitrogen and oxygen species in single cells

by

Damith Randika E.W. Patabadige

B.S., University of Colombo, 2006

A DISSERTATION

submitted in partial fulfillment of the requirements for the degree

DOCTOR OF PHILOSOPHY

Department of Chemistry
College of Arts and Sciences

KANSAS STATE UNIVERSITY
Manhattan, Kansas

2017

Approved by:

Major Professor
Christopher T. Culbertson

Copyright

Abstract

Recent approaches in analytical separations are being advanced towards the "lab-on-a-chip" concept in which multiple lab functions are integrated into micro/nano fluidic platforms. Among the variety of separation techniques that can be implemented on microfluidic devices, capillary electrophoresis is the most popular as it provides high efficiency, simple, fast and low cost separations. In addition, integrating miniaturized fluid manipulation tools into microfluidic devices with separations is essential for a variety of biological applications. Chapter 1 discusses the fundamentals of capillary electrophoresis and miniaturized fluid manipulation tools and provides an over view of single cell analysis in microfluidics.

In chapter 2, the integration of miniaturized peristaltic pumps into multilayer microfluidic platforms is discussed. In addition, device characterization, precise fluid control and high throughput single cell analysis are discussed. As a proof of principle, T-lymphocytes were loaded with two fluorescent probes Carboxyfluorescein diacetate (CFDA) and Oregon green (OG). Thousands of single cells were automatically transported, lysed on these devices and analytes from the lysate were electrophoretically separated. 1120 cells were analyzed over the course of 80 min (14 cells/min) and separation characteristics of analytes released from individual cells were investigated.

In the third chapter, the development of microfluidic platforms for the electrochemical detection of nitric oxide (NO) and other reactive nitrogen species (RNS) at the single cell level is discussed. A microfluidic system was developed to perform rapid cell lysis followed by electrochemical detection. Miniaturized microband electrodes were designed and integrated with a microfluidic separation channel. Three alignment techniques (in-channel, end-channel and off-channel configurations) were used to detect the electrochemical response of the analyte of interest.

Furthermore, a model analyte (CFDA) was used to demonstrate the potential of performing the simultaneous dual detection with electrochemical and laser induced fluorescence detection. In addition, the same microfluidic platform was adapted to detect intracellular superoxide using laser induced fluorescence.

In the fourth chapter, the off-chip integration of optical fiber bridges with multilayer microfluidic chips is discussed. A multimode optical fiber (~10cm long) was integrated between the single cell lysing spot and a spot downstream of the separation channel in order to detect both intact cells and the analyte in the lysate. This technique was used to create two detection spots on the microfluidic platform with the use of a single excitation source and single detector. Fluorescently labeled T-lymphocytes were automatically transported and lysed in a manner similar to that described in chapter 2. Hundreds of single cells were analyzed and the absolute migration time was determined for the analytes in the lysate. In addition, the separation characteristics of fluorescently labeled protein kinase B peptide substrates were investigated. Furthermore, this technique was used to measure cell size and the velocity of intact cells (discussed in 5^{th} chapter) by making use of a light tunneling concept available in multimode optical fibers.

All the experiments presented in this dissertation exploit the use of multilayer microfluidic platforms to investigate intracellular components in single cells in a high throughput manner that has several advantages over current conventional techniques.

Table of Contents

List of Figures

List of Tables

Acknowledgements

I would like to thank Graduate School and Department of Chemistry, Kansas State University for accepting my application and granting me this great opportunity to peruse Doctoral degree in Analytical Chemistry.

Dr. Christopher Culbertson, I would like to convey my heartiest gratitude for your expert opinions, guidance and valuable advices during my PhD research career. I was able to dramatically improve my knowledge as an Analytical Chemist because of your expert supervision during last five years. Thank you for everything you have provided. Also, I would like to thank past and recent group members of Dr. Culbertson's group including Dr. Anne Culbertson, Dr. Eve Metto, Tom Mickleburg, Samantha Warnecke, Kathleen Sellens , Jay Sibbits and Shu Jia. Also, office staff in Department of Chemistry and technical staff (Tobbe, Jim and Ron); thank you very much for all the help that you have provided me.

Our collaborators from KU, including Dr. Sue Lunte, Joe Siegel and all the other group members thank you very much for your faithful collaboration that we have built up more than five years. Especially, Dr. Sue Lunte, your expert opinions were help me a lot to troubleshoot many research issues and significantly improve my knowledge in the field of electrochemistry. Also, I would like to thank our another faithful collaborator, Laser and Plasma Institute, Iran. Especially, Dr. Jalal Sedeghi and Dr. Hamid Latifi, your expert knowledge in the field of fiber optics, helped me to produced novel ideas and advancing our laser induced fluorescent detection systems.

At last but certainly not least, I would like to thank my parents, my wife and my daughter Sanuki.

Dedication

To my loving father and mother, Leelarathna and Indrani, thank you for all the efforts that you've made for me.

Chapter 1 - Introduction

1.1 Analytical Separations

Analytical separation techniques are used in laboratory and industrial applications and play key roles in the isolation and purification of samples or compounds. Drug screening, drug discovery, clinical applications, protein/ DNA analysis, forensic and environmental studies utilize a variety of separation techniques[1] (e.g. electrophoresis, chromatographic techniques, extraction, sedimentation, distillation, evaporation, filtration, sublimation, osmosis) depending upon the characteristics of the analyte and the purpose of analysis. In large-scale separations, especially in industrial applications, solvent extraction is one of the popular techniques. Solvent extraction is based on differences in the degree of solubility of analytes in two immiscible liquids. Simply, this is known as the "like-dissolves-like" concept. In other words, polar molecules prefer to interact with polar solvents and non-polar molecules interact with non-polar solvents. This same principle applies to chromatography-based separations. In chromatography, different degrees of molecular interactions with the stationary phase and the mobile phase govern the elution time of the analytes. For example, in normal polarity mode, more polar molecules elute at higher retention times compared to non-polar molecules since the stationary phase is polar and the mobile phase is non-polar. A variety of other chromatographic mechanisms can also be applied to separations including adsorption, ion-exchange, size exclusion and immunoaffinity depending on nature of the application. Over the past 5 decades, improvements in chromatographic performance have resulted in instrumentation and methods such as High Performance Liquid Chromatography (HPLC), Ultra High performance Liquid Chromatography (UPLC) and mass spectroscopy coupled Gas Chromatography (GC-MS) that are capable of high throughput and high efficiency analyses. These techniques are popular in many research and development applications, including pharmaceutical

development, environmental analyses and forensic studies since they provide powerful separations in near real time.[2] These techniques, however, have several drawbacks including high cost, time consuming sample pretreatments and the need for advanced instrumentation.

The "Lab-on-a-chip" concept provides an alternative approach to overcome some of the limitations of current commercial chromatographic instrumentation. Using this approach multiple chemical handling and analysis functions are integrated into small devices with molded or etched channels in a manner similar to the integration of the multiple electronic processing steps that occur in microprocessors. The ability to integrate multiple separation and detection techniques into a miniaturized system reduces cost, minimizes the sample size needed, decreases reagent volumes and results in a small working footprint for the device. In such devices, most commonly, fluid and sample manipulation are performed by utilizing capillary or microfluidic manifolds. Fluid manipulation, separation and device fabrication techniques will be discussed in more detail under the following sections.

1.2 Fluid Trasport in Capillaries

Spontaneous fluid flow through capillary channels can occur due to pressure gradients. In capillary channels, fluid flow is laminar in which fluid propagation occurs in thin parallel layers. Lateral mixing between layers occurs only through molecular diffusion. As the velocity and viscosity vary, the lateral mixing becomes more violent and leads to turbulent flow. The flow nature (whether it is laminar or turbulent) can be quantitatively evaluated using Reynolds number (R_e).

$$R_e = Lv\rho / \eta \tag{1.1}$$

where, L - length of the capillary, v - average velocity of the fluid, ρ -density of the fluid

η- viscosity of the fluid. Typically, in microfluidic/ capillary channels, the R_e is in the range of 0.1-100. When R_e>2000, flow patterns become turbulent.

Proper fluid manipulation is one of the key factors for biological automation in microfluidics. Most commonly, fluid manipulation in capillary/ microchannels is performed via two techniques known as electrokinetic flow and pressure driven flow.

1.2.1 Pressure Induced Flow

When a fluid is moving through a capillary it experiences two different forces due to the pressure gradient and friction.[3] The force exerted by the pressure (F_p) can be defined in terms of pressure drop (Δp) and surface area of the capillary. Assuming the capillary is cylindrical with radius (r_c),

$$F_p = \Delta p \pi r_c^2 \tag{1.2}$$

The drag force (F_d), depends on the length of the capillary (L), the viscosity of the fluid (η) and the shear rate $\left(\frac{dv}{dr}\right)_0$ at the capillary wall.

$$F_d = -2\pi r_c L \eta \left(\frac{dv}{dr}\right)_0 \tag{1.3}$$

At the steady state, $F_p = F_d$

By using eq 1.2 and eq 1.3, the shear rate can be derived as,

$$\left(\frac{dv}{dr}\right)_0 = \left(-\frac{\Delta p r}{2L\eta}\right) \tag{1.4}$$

Integration of eq 1.4 yields a relationship between velocity (v) and the radius (r), which is applicable for any arbitrary cylindrical fluid plug (eq 1.5).

$$v = \left(-\frac{\Delta p r^2}{4L\eta} \right) + c \tag{1.5}$$

where, constant (c) can be evaluated using boundary conditions.

when, $r = r_c, v = 0$.

$$\therefore c = \left(\frac{\Delta p r_c^{\,2}}{4L\eta} \right) \tag{1.6}$$

hence, eq 1.5 can be rewritten as,

$$v = \left(\frac{\Delta p}{4L\eta} \right) \left(r_c^{\,2} - r^2 \right) \tag{1.7}$$

Eq 1.7 implies that the velocity of the fluid has a parabolic flow profile (**Figure 1.1**).

Therefore, the maximum velocity (v_{max}) due to the pressure driven flow can be given as,

$$v_{max} = \left(\frac{\Delta p r_c^{\,2}}{4L\eta} \right) \text{ (at, } r = 0 \text{)} \tag{1.8}$$

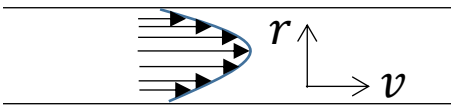

Figure 1.1: Velocity profile of pressure induced flow. Size of the arrows indicates the magnitude of the velocity vector in unidirectional flow.

Pressure induced fluid manipulation significantly reduces peak resolution due to the band broadening resulting from parabolic flow.[4] This phenomenon can even be observed in high performance separation techniques such as HPLC, UPLC and GC. An alternate method to improve separations in terms of band broadening is capillary electrophoresis.

1.2.2 Capillary Electrophoresis(CE)

In CE, charged ions are separated in the presence of an electric field. The capillary wall consists of silanol groups (Si-OH) and a negative charge on the surface is formed via ionization of silanol groups at pH's > 3.[4] In capillary electrophoresis, a buffer solution is pumped through the capillary via electroosmosis.

Electroosmosis arises from the double layer that is formed near the capillary surface. This double layer is formed when positively charged ions in the buffer solution are attracted to the negatively charged surface (**Figure 1.2**). These charges arrange to form 2 layers – one partially desolvated and immobile and the other fully solvated and mobile.

"The potential difference across interface of the outer Helmholtz layer and the diffuse layer is known as zeta potential (ζ)".[4] Beyond the compact electric double layer (Stern layer), another layer is formed with mobilized ions known as the diffuse layer. The potential of these layers varies as a function of distance from the capillary wall. In the Stern layer, the potential drops linearly whereas in the diffusive layer it decays exponentially.

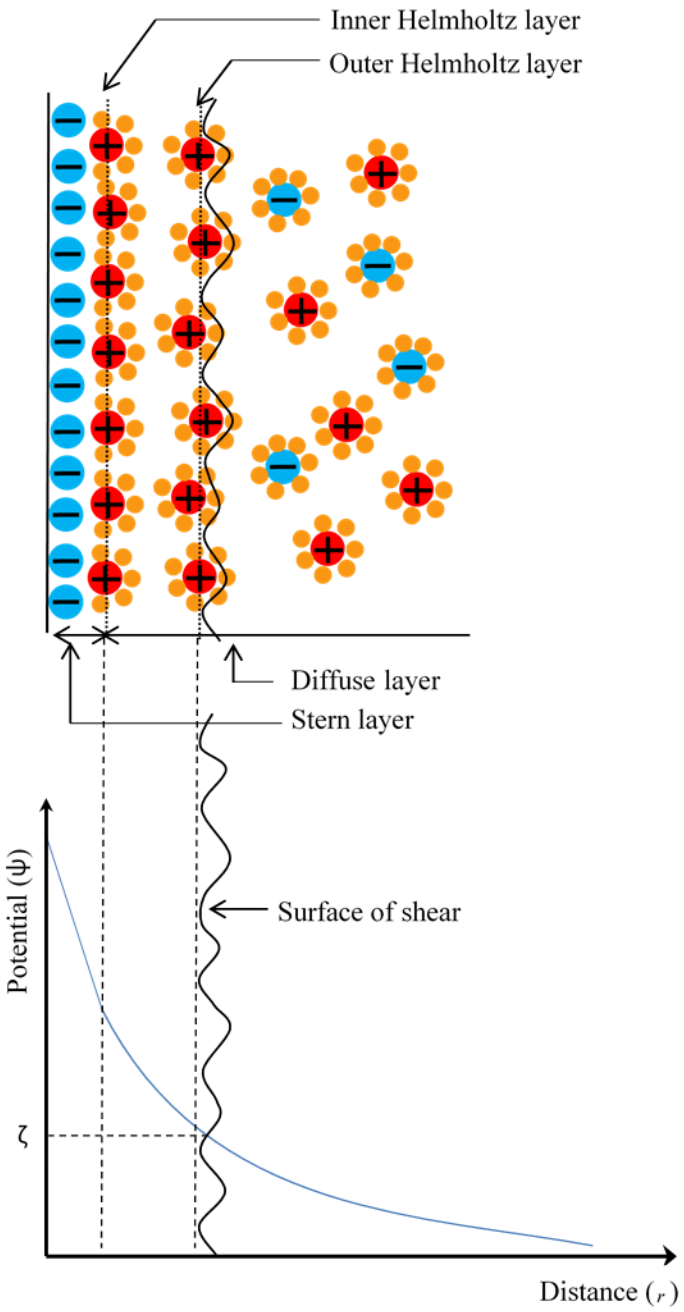

Figure 1.2: Schematic representation of the electric double layer and the diffuse layer. Potential (Ψ) varies as a function of distance measured from the capillary wall. In the inner Helmholtz layer, potential drops linearly, whereas, in the outer Helmholtz layer, potential drops exponentially. The Zeta potential (ξ) represent, the potential develops in the interface of outer Helmholtz layer and the diffuse layer.[4]

In the presence of an electric field the solvated cations, which are in excess in the mobile part of the double layer, are attracted to the cathode and generate a bulk flow of buffer in that direction. This phenomenon is known as electroosomotic flow(EOF). In the presence of an applied electric field, charged analyte ions will migrate based on their charge/hydrodynamic drag ratio. Positively charged ions move towards the cathode and negatively charged species move towards the anode. Neutral species are not affected since they do not experience any force due to the electric field. Charge, size and the viscosity of the medium determine the velocity of each species. For example, the higher the charge, the faster the migration. The larger the size, the lower the migration due to frictional force. Electroosmotic flow is typically greater than electrophoretic migration, thus positive, neutral and negatively charged species all migrate toward the cathode where they can be detected. This phenomenon allows the separation of charged and neutral species.[4] Listed below in order of increasing migration velocity.

Negatively charge ions < Neutral spices < Positively charge ions

$\longrightarrow$

Migration velocity increases

Electrophoretic velocity (υ_e) and electroosmotic velocity (υ_{eo}) are a function of the electric field (E), electrophoretic mobility(μ_e) and electroosmotic flow mobility(μ_{eo}) as shown in the following equations.[4, 5]

$$\upsilon_e = \mu_e E \tag{1.9}$$

$$\upsilon_{eo} = \mu_{eo} E \tag{1.10}$$

The vector quantity total velocity is given by equation 7.

$$\upsilon = \upsilon_e + \upsilon_{eo} \tag{1.11}$$

Neutral species are simply carried along in the electroosmotic flow.

μ_e is proportional to the electric force (F_E) experienced by the molecules and inversely proportional to the frictional force of the medium (F_F). F_E is given as,

$$F_E = qE \tag{1.12}$$

where, q is the charge of the particle.

The frictional force that is experienced by the particle can be given as,

$$F_F = -6\pi\eta r\upsilon_e \quad \text{(Stoke's law)} \tag{1.13}$$

At steady state, the net force experienced by a charge particle is zero.

i.e $$6\pi\eta r\upsilon_e = qE \tag{1.14}$$

where, r is radius of the particle. By solving equations (1.9) and (1.14),

$$\mu_e = q / 6\pi\eta r \tag{1.15}$$

μ_{eo} is a function of zeta potential (ξ), dielectric constant (ε), viscosity of the medium (η).

$$\mu_{eo} = \xi\varepsilon / \eta \tag{1.16}$$

For given electrophoretic separation, the migration time (t) can be given as follows:

$$t = \frac{l}{(\mu_e + \mu_{eo})E} \tag{1.17}$$

where, l is length to the detector.

1.3 Separation Principles

1.3.1 Band Dispersion

In CE separations, analyte response is recorded in the time domain. Under the ideal conditions, peak shape resembles a Gaussian distribution because of the random band broadening process. Base line peak width (W) is defined in terms of the standard deviation (σ) of the peak.

$$W = 4\sigma \tag{1.18}$$

However, under experimental conditions, peak shape can deviate from the Gaussian shape. Such deviations can be quantified in terms of peak skewness and peak tailing.

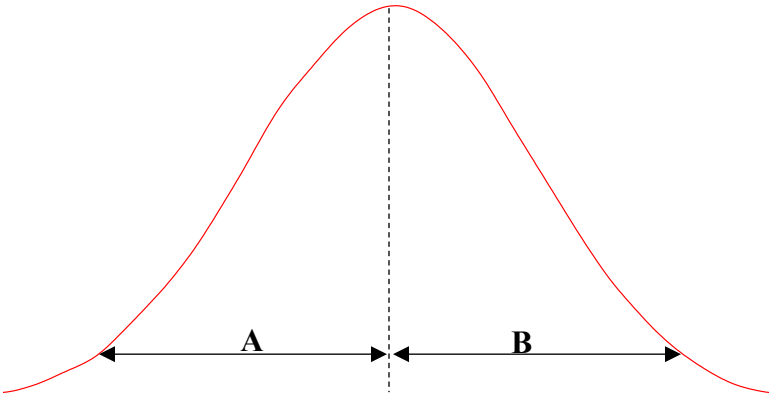

Figure 1.3: Description of peak shape in terms of peak width

If $B > A$,

$$\text{Peak tailing} = A + B/2A \tag{1.19}$$

$$\text{Peak skewness} = B/A \tag{1.20}$$

1.3.2 Separation Efficiency

The number of theoretical plates (N) is a measure the efficiency of the separation. This can be defined as,

$$N = {}^{l}\!/_{\sigma^2} \tag{1.21}$$

Plate height (H) is inversely proportional to the number of theoretical plates.

$$H = {}^{l}\!/_{N} \tag{1.22}$$

1.3.3 Resolution

Peak resolution measures separation quality and it reflects the peak resolving ability. R_s can be mathematically defined as follows.

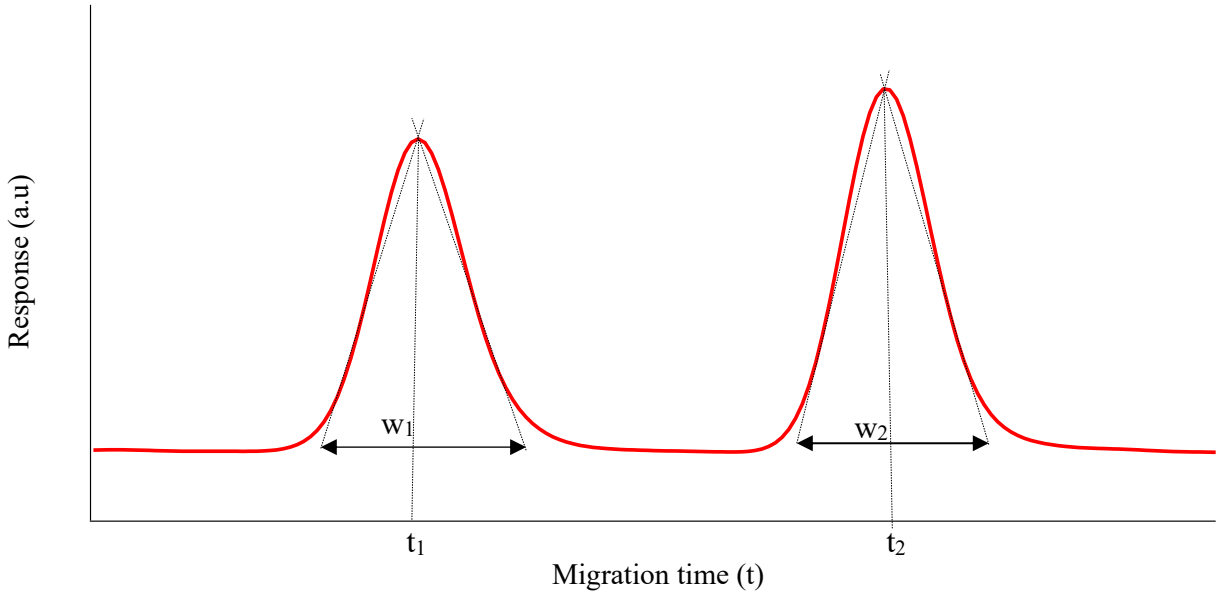

Figure 1.4: Schematic representation of typical electropherogram of the separation of two analytes. Baseline resolution is defined in terms of migration time and peak width or temporal standard deviation

$$R_s = \frac{2(t_2 - t_1)}{(w_1 + w_2)} = \frac{(t_2 - t_1)}{4\sigma} \tag{1.23}$$

where, σ is the temporal standard deviation

t_1 and t_2 are migration times of the first analyte and the second analyte respectively. w_1 and w_2 are the baseline widths of the first and the second analyte respectively.

Complete baseline resolution can be observed when $R_s > 1.5$. If $R_s < 1.5$, that is indicative of peak overlap.

1.3.4 Band Broadening Factors

The Van deemter equation is useful to determine the effect of band broadening in both CE and HPLC.

$$HETP = A + Bu + C/u \tag{1.24}$$

where,

$HETP$ - height equivalent to a theoretical plate

A is the Packing factor, B is the longitudinal diffusion coefficient and C is the mass transfer coefficient

In CE ,there is no column packing and analytes are driven to the detector using electroosmotic flow. Therefore, both the A and C terms will cancel and only the B term remains. The B term arises due to the random diffusion of molecules, explained by the second law of thermodynamics (i.e entropy of the universe increases in any spontaneous process).

In capillary electrophoresis, band broadening is small due to the flat fluid flow profile (**figure 1.5**), whereas, in HPLC, the parabolic flow profile leads to significant dispersion, resulting in band broadening.

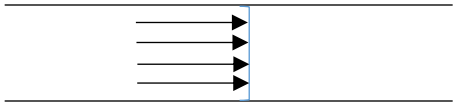

Figure 1.5: The velocity profile of electroosmotic flow. Size of the arrows indicates the magnitude of the velocity vector.

The longitudinal diffusion ($\sigma^2_{Diffussion}$) can be defined with diffusion coefficient (D) and the migration time (t).

$$\sigma^2_{Diffusion} = 2Dt \tag{1.25}$$

D is a function of Boltzmann constant (k), temperature (T), viscosity of the liquid (η) and radius of the moving particle (r).

$$D = kT/6\pi\eta r \tag{1.26}$$

Longitudinal diffusion is an unavoidable band broadening source. This is due to the concentration gradient of analyte band in the axial direction. This is a random diffusion process and can easily be explained with the second law of thermodynamics. Even under the ideal separation conditions, longitudinal diffusion contributes to the band dispersion.

However, several other factors contribute to band broadening in CE apart from longitudinal diffusion. These band broadening sources are independent each other and these quantities are additive.

They are injection plug length (σ^2_{inj}), electrodispersion ($\sigma^2_{electrodispersion}$), temperature gradient effects (σ^2_{temp}), detection window length ($\sigma^2_{detection}$) and adsorption (σ^2_{ads}).[4, 5]

1.3.4.1 Injection plug length

If the injection plug length is greater than the length of longitudinal diffusion, band broadening occurs and eventually leads to loss of resolution. However, this is usually not significant unless the separation distances are short and that it is constant whereas other sources like diffusion occur constantly over the course of the separation. This band dispersion source is negligible under most of the separation conditions (unless extremly fast separations are performed).

Total variance of injection plug length (w) can be written as,

$$\sigma^2_{inj} = w^2/12 \qquad (1.27)$$

1.3.4.2 Electrodispersion

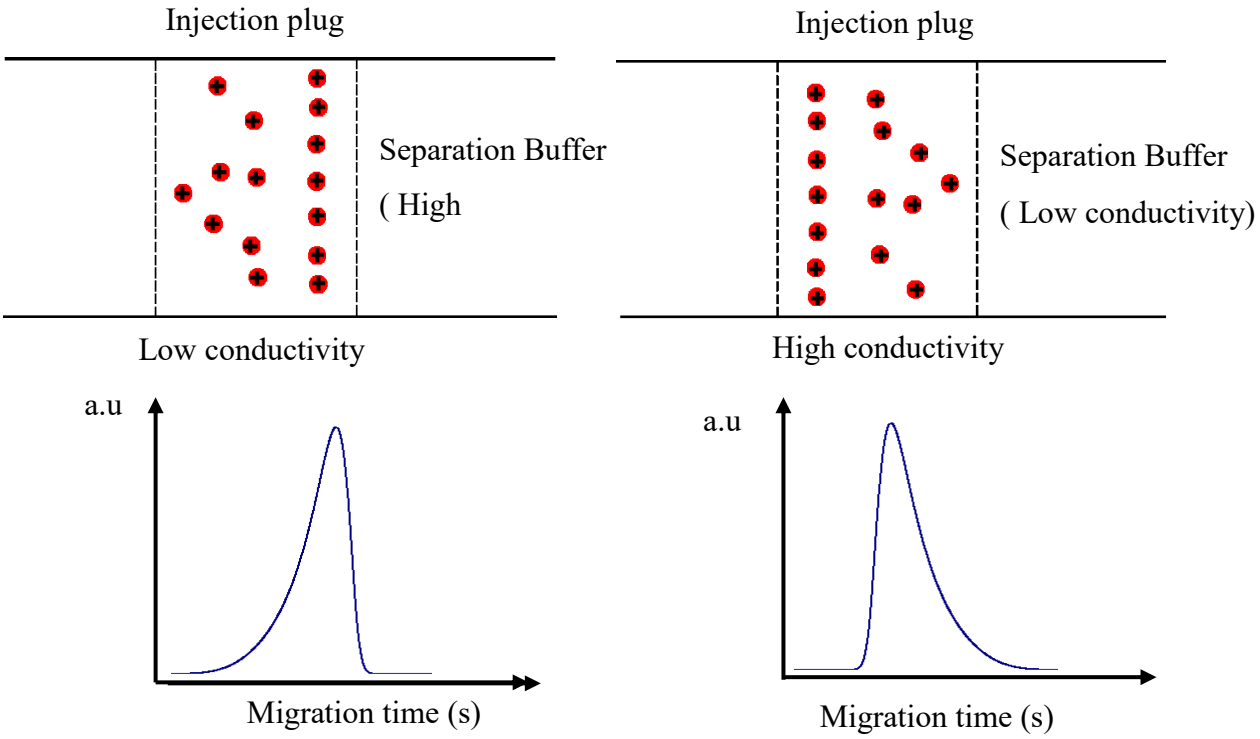

Figure 1.6: Schematic of peak tailing due to conductivity mismatch between mobile phase and the sample

The conductivity mismatch of the sample buffer and the separation buffer leads electrodispersion if the conductivity of the sample zone is higher than that of separation buffer. Thus peak tailing occurs in the beginning of the peak due to the diffusion of highly conductive ions and also back edge will be sharp (**see fig. 1.6 a**). In contrast, the front edge of the peak will be sharp if the conductivity of the sample zone is lower than that of the separation buffer since the low conductive ions will diffuse backward (**see fig. 1.6 b**). This can be minimized by dissolving the sample in same buffer as background buffer.[5] Since this is counteracting longitudinal diffusion (sample plug genarates one edge), this source is not additive with other band broadening sources.

1.3.4.3 Adsorption

In CE, microfluidic channels are usually made with materials such as fused silica, PDMS and polymethyl methacrylate (PMMA). When fused silica is used, free silanol groups on the surface consist of negative charges. Cationic substances can adsorb on the surface via electrostatic interactions. When using, elastomeric rubber materials, such as PDMS and PMMA, adsorption of large molecules, such as peptides and proteins, on the wall may occur due to the hydrophobic interactions. However, this is not significant unless extreme separation conditions (e.g. using a highly basic buffer solution). Variance of the adsorption process can be expressed as,

$$\sigma^2{}_{ads} = \frac{k^1 v l}{\left(1+k^1\right)^2}\left[\frac{\left(r^2+k^1\right)}{4D}+\frac{2}{K}\right] \tag{1.28}$$

where, $k^1 = \frac{\left(t_r - t_0\right)}{t_0}$ (capacity factor)

t_r - the elution time of the retained molecule

t_0 - the elution time of the unretained molecule

ν - the electroosmotic flow velocity

D - the diffusion coefficient

l - the length of the capillary

K - the dissociation constant

1.3.4.4 Temperature effects

When ionic species move through a solution, frictional drag generates heat in a process called Joule heating. Heat transfer among molecules increases the entropy and leads to band dispersion. The rate of heat generated per unit volume (J_Q) is defined as,

$$J_Q = {i^2}/{\kappa A^2} \tag{1.29}$$

where, i - current

A - cross sectional area

κ -conductivity

In addition, the temperature inside the capillary varies as a function of distance from the capilary wall. This temperature gradient (ΔT) generates band broadening due to the dispersion of the injection plug. Dispersion arises here because the temperature in the core of the lumen is higher than at the edges because of the heat dissipation. This means that the core is at a lower viscosity and therefore moves faster generating a parabolic flow profile. ΔT is a function of power density (Q), radius of the capillary (r), thickness of the polyimide coating, thermal conductivity (κ) and thermal transfer rate from the capillary (h).

$$\Delta T = \frac{Q r_1^2}{2}\left[\frac{1}{\kappa_1}\ln\left(\frac{r_2}{r_1}\right)+\frac{1}{\kappa_2}\ln\left(\frac{r_3}{r_2}\right)+\frac{1}{r_3}\left(\frac{1}{h_1}\right)\right] \tag{1.30}$$

κ_1 and κ_2 are thermal conductivities of fused silica and polyimide respectively, and r_1, r_2 and r_3 are the inner radius, outer radius and outer radius of polyimide coating, respectively.

This become more significant when using highly conductive separation buffer and a strong electric field. Also, this depends on rate of heat dissipation to the surrounding. However, this type of band broadening can be minimized by decreasing the conductivity of separation buffer and reducing the electric field strength of any given separation. Also, using glass microchannels helps very efficiently dissipate the heat to the surrounding due to larger mass and surface area.[5]

1.4 Microfluidics

Microfluidics is a broad dynamic field based on the concept of "Lab-on-a-chip" and is applicable in almost all scientific research areas.[1, 2] The idea behind such systems is to integrate multiple sample handling and analysis functions in a small device that typically has a footprint that is no more than several cm^2/$inches^2$ in size. These systems are also known as micro total analysis systems (μ-TAS). These devices were first developed as analogous to electronic chips thus they are also referred as lab-on-a-chip, lab chip and microchip. The invention of Micro Electro Mechanical Systems (MEMS) in the 1960's helped designing microfluidic based pressure sensors using similar fabrication process. Over next twenty years these systems were gradually adapted to perform gas chromatography based separation. The first reported microfluidic system was developed as a gas chromatograph by S.C Terry in 1979.[6] Recently, μ-TAS are utilized in variety of microscale sample/fluid manipulation and detection techniques in bioanalytical chemistry. For example, these μ-TAS have been adapted to cell culturing, cell sorting, DNA analysis, protein analysis and immunoassays.[1]

One of the most important features of microfluidic experiments is ability of performing with low sample/ reagent volumes. Recently, these devices have advanced to handle fluid volumes down to the picoliter scale. Some advantages of using microfluidic devices include automation, high throughput manipulation, biocompatibility and cost effectiveness. Such advantages have made these systems very popular across a variety of research areas.[2]

1.4.1 Microchip Fabrication

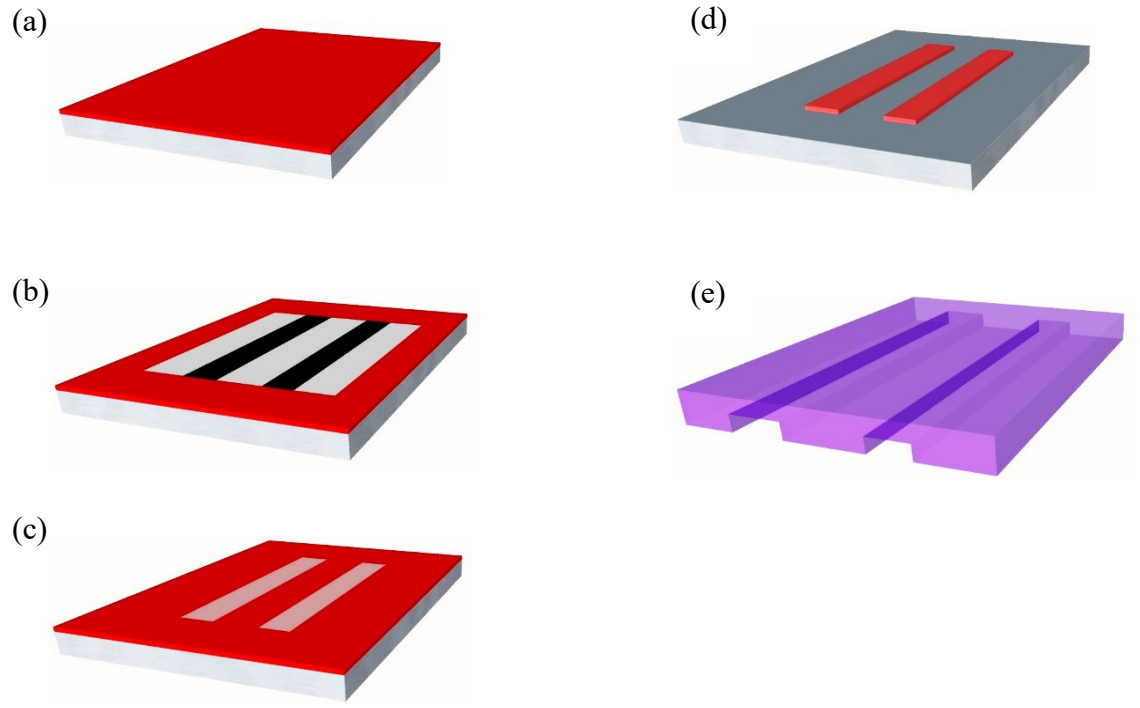

Figure 1.7: Fabrication process of monolayer microfluidic device using softlithography (a) spin coating the photoresist (b) exposure into UV radiation using a patterned photomask (c) polymerized feature on the photoresist (d) wet chemical etching removes polymerized/un-polymerized features and provide positive stamp for replicate molding (e) Negative PDMS layer that consists of microfluidic channels

Microchip fabrication is typically performed with conventional photolithography. This is also referred as to soft lithography since elastomeric rubber materials are used. Soft lithography is a powerful technique that can be used to fabricate monolayer microfluidic devices. Typically microchip fabrication is performed using transparent elastomeric rubber known as PDMS. Using this technique positive stamps are fabricated to perform replicate molding. This is a stepwise process (**see fig. 1.7**). Specific details of the microchip fabrication are given in Chapter 2.3.

Soft lithographic techniques can be extended to integrate many layers in the same device. This is known as multilayer soft lithography in which elastomeric layers are fabricated separately (**see Chapter 2.3)** and then irreversibly bonded together to form a multilayer device. Multilayer soft lithography is low cost, biocompatible, fast and easy. In order to demonstrate the power of this technique Quake's group has fabricated seven layer microfluidic chip.[7] Properties of individual layers such as magnetism and electrical conductivity can be modified by doping with foreign materials.

1.4.2 Fluid Flow Manipulation in Microfluidics

The most common methods to introduce flow in microfluidic manifolds are electroosmotic and pressure driven flows. Pressure driven flow can be implemented by the application of super or sub ambient pressure at the termini of the channels. Electroosmotic techniques are useful if all the analytes are electrically charged as then they can be separated via electrophoresis. Electroosmotic driven flow can be easily controlled on these devices to perform small volume electrokinetic sample injections.

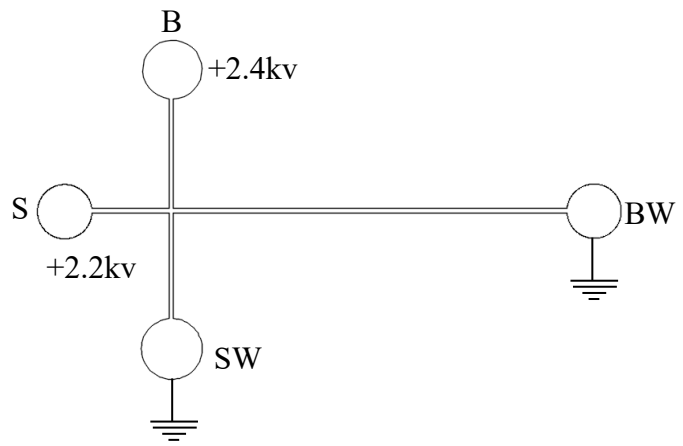

Figure 1.8: Schematic of "cross shape" shape microfluidic manifold typically used for electrokinetic injections.

In electrokinetic gated injections, a simple "cross shape" microfluidic manifold is typically used. As shown in **Figure 1.8,** a high voltage is applied to both sample reservoir (S) and buffer reservoir (B). At the same time, both the buffer waste (BW) and sample waste (SW) reservoirs provided path ground. In this configuration, an electroosmotic flow is developed between S and SW since the electric current follows the incompressible fluid flow between these two reservoirs. If the grounding electrode is reduced for several milliseconds, electroosmotic flow is generated briefly between S and BW. Then, the grounding electrode in SW is re-connected driving the sample plug toward the detector at the downstream of the separation channel. In this manner, discreet injections can be achieved with automation. However, the use of this technique is limited when the sample is sensitive to the electric fields. For example, in single cell analysis many cell types are easily lysed once they are exposed to electric field. Such limitations can be easily eliminated using pressure induced cell transport. Pressure driven flow can be generated in a variety of ways including simply maintaining different liquid levels between the sample and waste reservoirs. Even though this technique is simple to implement, it generates slow, poorly controllable flow and

therefore results in a low cell analysis throughput. In the sub ambient mode, the pressure is lowered at the termini in a channel through the use of a vacuum or syringe pump in the withdrawal mode (**figure 1.9**). This approach can generate fast flow but it is difficult to control precisely and requires the use of large expensive off-chip equipment and external tubing. One of the better alternatives for such limitations is using on-chip fluid handling techniques (**figure 1.10**). In the beginning of the last decade, soft photolithography was used to develop integrated on-chip pumps. This type of pump was first reported by Stephen R. Quake for the transport of fluids and bacteria on microfluidic devices.[7] These on-chip pumps act similarly to a peristaltic pump. Generally, these on-chip pumps are created using a set of 3 on-off valves that can be pneumatically actuated in a repeatable pattern to drive the fluids through the microfluidic channels. In addition, these type of valves can be implemented to perform well defined discrete hydrodynamic injections using "valve-on" and "valve-off" configurations.[8]

These pumps allow precise control of the fluid flow through tuning channel widths, valve actuation frequency, valve actuation pressure and the gaps between the valves. These pumps are simple, durable, easy to fabricate and easy to integrate into small device area.

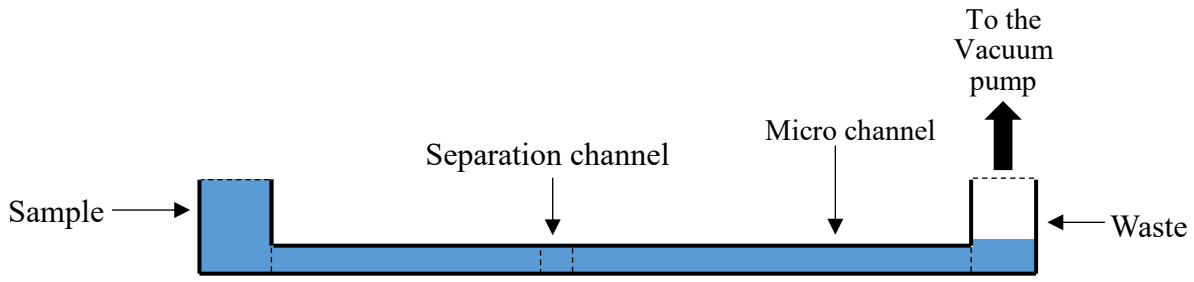

Figure 1.9: Pressure gradient is created between sample reservoir and waste reservoir using external vacuum pump

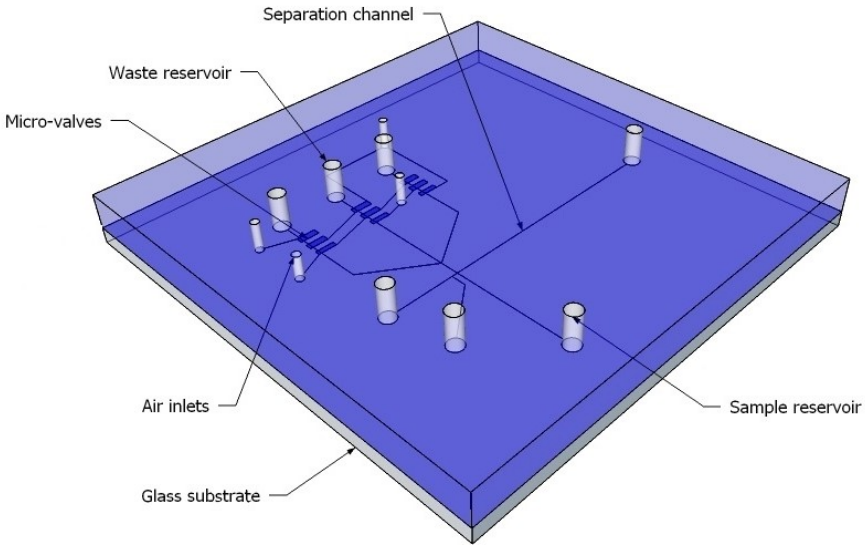

Figure 1.10: A two-layer microfluidic device with on-chip pumping system. Three parallel microfluidic channels are integrated with pneumatically controllable micro valves. Hydrodynamic flow can be created between sample and waste reservoirs by actuating micro pumps/valves

1.4.2.1 Peristaltic Pumps

Peristaltic pumps are positive displacement pumps that allow the transport of different types of fluids through the patterned opening and closing of a set of valves in a series along a short section of channel. The valves are actuated by applying forces to elastomeric membranes that deflect and close the fluidic channels (**Figure 1.11**). In the absence of an applied force, the valve/channel is normally open. By opening and closing the valves in a specific repeatable sequence a pumping action is generated and fluid is driven through the channels.

Figure 1.11: Cross section of elastomeric layer that consists of hemispherical shape profile. To the fluidic channel, an external force is applied and thin elastomeric membrane deflects downwards

Peristaltic pumps have been used in a wide range of applications in microfluidic devices, as they allow for the precise control of fluid flow through a microfluidic manifold.[7, 9, 10] Both pneumatically controlled and non-pneumatically controlled peristaltic pumps have been reported in the literature. Non-pneumatic pumps including pH responsive hydrogel valves [11] and thin shape memory alloy wires[12] have been used to control fluid flow in microfluidic channels. Electrostatic,[13, 14] electrochemical[15] and magnetic microvalves[16, 17] have also been reported. Pneumatically controlled microvalves (**Figure 1.12**), are the most popular, as they have quick response times compared to non-pneumatic categories. Pneumatic microvalves can be easily integrated into multilayer microfluidic devices.

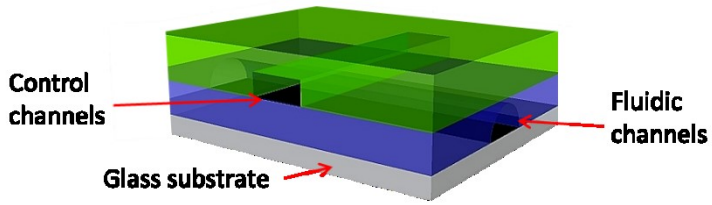

Figure 1.12: A Two-layer PDMS/glass hybrid microfluidic device; pneumatic valves (top layer) are integrated with microfluidic manifold (bottom layer).

The chip fabrication process plays a critical role in proper valve functioning. Hemispherical shaped fluidic channels are used in the fabrication process in order to allow the channel to close completely. Rectangularly shaped fluidic channels cannot be closed completely for any given pressure. Even though, the elastomeric membrane completely deflects; fluid can leak through either side of the fluidic channels. This limitation can be eliminated with rounded channels since they completely close with a modest applied pressure (**see fig.1.13**).[7]

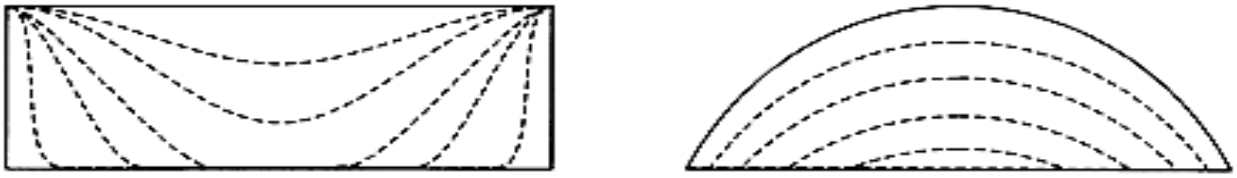

Figure 1.13: Comparison of a rectangular shape channel and a rounded shape channel. As pressure increases, the elastomeric membrane is deflected and closes the fluidic channel. Rectangular channels cannot be closed completely. Rounded shape channels can be closed completely with less applied pressure. From Unger, M. A.; Chou, H.-P.; Thorsen, T.; Scherer, A.; Quake, S. R., Monolithic microfabricated valves and pumps by multilayer soft lithography. *Science (Washington, D. C.)* 2000, *288* (5463), 113-116. This figure was reproduced with the permission from The American Association for the Advancement of Science.[7]

For example, if the effective surface area of the pump is 100µm x 100 µm and fluidic channel is 20 µm deep, rectangularly shaped channels are not completely closed even at 200kPa, whereas, hemispherical shape channels are completely closed at 40kPa.[7]

In two-layer device fabrication, both positive and negative tone photoresists are used in order to produce two layers (positive tone photoresists become soluble in wet chemical etching process when they expose to the UV light. In contrast, negative tone photoresists become insoluble in wet

chemical etching process after they expose to UV light). Briefly, SU-8 negative tone photoresist is used to fabricate pneumatically controlled channels, whereas, fluidic channels are fabricated with a positive tone photoresist (ex: AZ 4620). However, after the initial fabrication step, the profile of fluidic channels consists of rectangular shape. A "Reflow" technique is used to transform rectangularly shaped channels to rounded shaped channels (**figure 1.14**). If AZ 4620 is used, the temperature of the master mold is increased to 120 °C. At elevated temperature, the photoresist re-melts and starts reflow as temperature gradually decreases.

Figure 1.14: Transformation of a rectangular shape channel into a rounded shape channel using reflow technique.

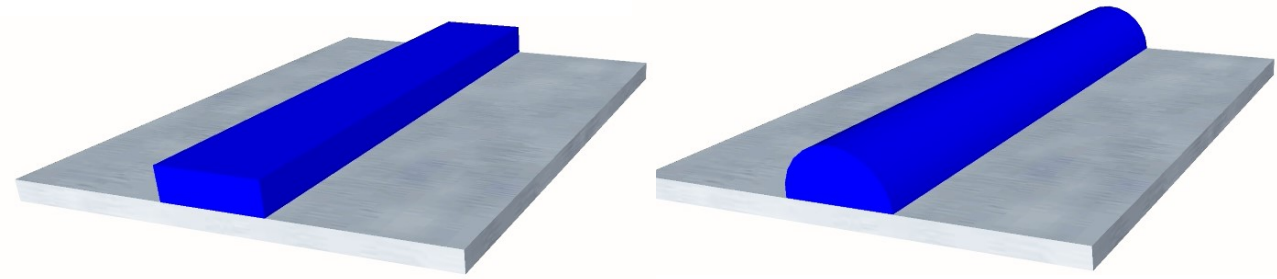

(a) (b)

Figure 1.15: Positive stamps for replicate molding. (a) and (b) are SU-8 and AZ4620P positive stamps respectively

Two PDMS layers are separately fabricated and the micropumps air actuation channels are then aligned on the fluidic channels. In this process, a two layer chip is formed such that the top layer consists of excess base molecules and the bottom layer consists of excess curing agent molecules.

These layers are further cured to make an irreversible bond between the top and bottom layers (In the curing process, excess base molecules and excess curing agent molecules in the interface further react each other to form irreversible bonding between two layers). Finally, the bottom layer is sealed onto a clean glass substrate to form a PDMS/glass hybrid two-layer microchip.

The vertical gap between the fluidic channels and the pneumatically controlled channels is also an important factor for complete valve closure. Previous reports suggest that the optimum gap should be ~30µm for a proper deflection of the elastomeric membrane. [18]

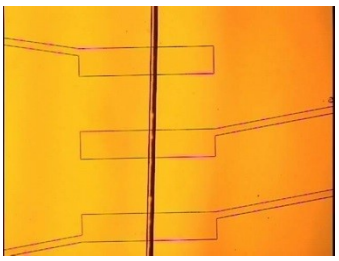

Figure 1.16: Pneumatically controllable micro pumps use three on-off valves aligned on the microfluidic channel. 10× magnification under inverted microscope, 100 × 400 µm peristaltic pumps, the fluidic channel is 100µm wide and 20µm high

A simple three parallel on-off valve design integrated with a fluidic channel (**see fig.1.16**). was used to pump bacterial cells (*Escherichia coli*) through a microfluidic device (in this experiment, 94% of *Escherichia coli* was survived).[7] Also, this report indicated that these pneumatic valves were highly robust and durable. These valves have also been adapted to create other microfluidic manipulation tools (**figure 1.17**) such as "on-off valves", "switching valves" and "a grid of on-off valves".[7]

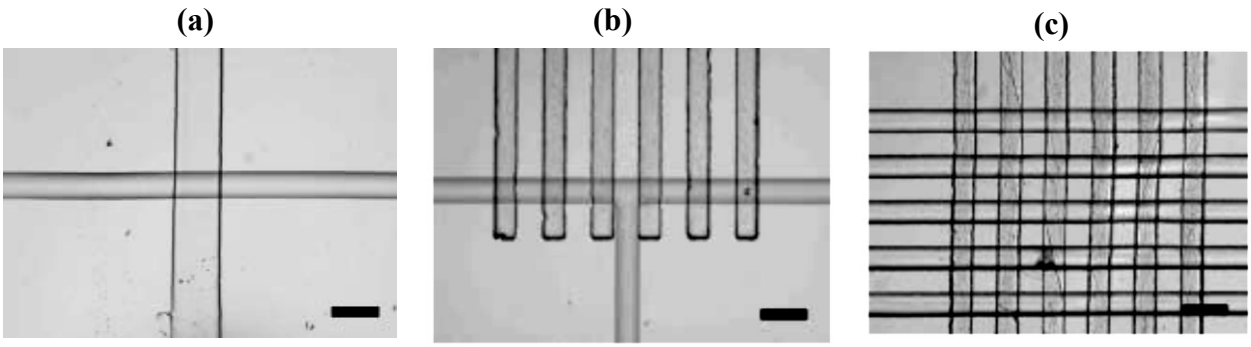

Figure 1.17: Microscopic images of different valve configurations. Pneumatic control lines are oriented vertically. (a) An on-off valve with a 100µm wide fluidic channel and a 200µm wide control channel (b) A set of switching valves (c) A grid of on-off valves. From Unger, M. A.; Chou, H.-P.; Thorsen, T.; Scherer, A.; Quake, S. R., Monolithic microfabricated valves and pumps by multilayer soft lithography. *Science (Washington, D. C.)* 2000, *288* (5463), 113-116. This figure was reproduced with the permission from The American Association for the Advancement of Science.[7]

Two main types of pneumatic microvalves (**figure 1.18**) have been reported in the literature. These are known as push-up and push-down valves. [19]

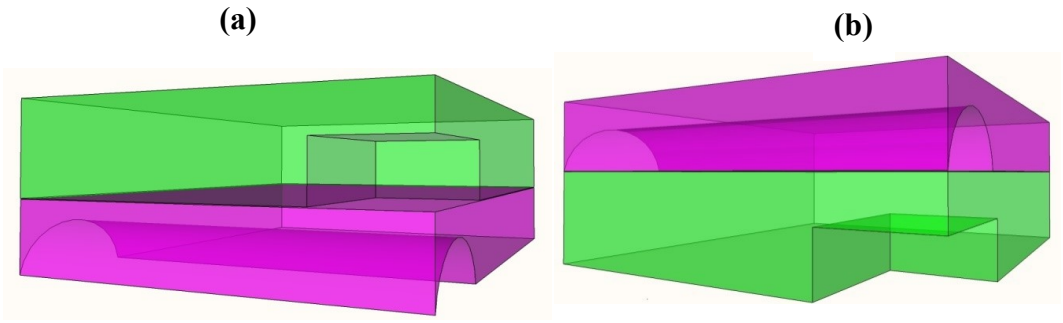

Figure 1.18: A Two-layer microfluidic device that consists of a fluidic channel (purple) and a pneumatically controlled channels (green), (a) a push-down valve (top layer) and (b) a push-up valve (bottom layer)

In the push-up configuration, air is pumped through the bottom elastomeric layer. In this case, the elastomeric membrane deflects upward closing the fluidic channel, whereas in push-down configuration, the top elastomeric layer deflects downward. Push-up valves can be operated with lower pressures compared to push-down valves. As a result, the push-up valve can close much deeper fluidic channels under the same actuation conditions.

These two types of microvalves were systematically characterized using 3 different models to understand their behavior. They are known as "the thick beam model", "the thick spring model (or the suspension bridge model)" and "the thin spring model".[19] In the thick beam model, "each valve dimensions is modeled as a pair of rigid beams joined in the middle". In the thin spring model "The valve membrane is treated as a one-dimensional spring composed of a semi-liquid slab". In the thick spring model the membrane is assumed to be "A suspension bridge hanging across the channel". Comparison of these 3 models to the push-up and push-down actuators, indicate that the "the thick spring model" most accurately replicates the behavior of the push-up valves while the "the thin spring model" most accurately replicates the behavior of the,[19] push-down valves.[20]

1.5 Single Cell Analysis

The rapid analysis of single cells can provide more information than the analysis of a bulk cell sample. Bulk cell analysis only provides an overall average value of a parameter in a group of seemingly similar cells. Bulk measurements provide no information about rare cells in a population that might be very active or non-active. Such cells may provide interesting information about the etiology of diseased cells. Thus, the potential heterogeneous nature of a population of cells can only be observed in SCA. Physically, cell heterogeneity can occur in several ways such as size, shape, deformability and rigidity. In addition, biological properties, such as gene and RNA expression, protein levels and enzyme activities can vary from cell to cell within an otherwise

seemingly homogeneous population. Despites these advantages, SCA can be time consuming and difficult to implement effectively compared to bulk cell analysis. Because of its ability to better characterize individual cell properties, however, SCA is applicable to many areas including cancer researches, tissue engineering, stem cell biology, immunology and neurology and so the time and effort to perform such analyses are worthwhile.

Because the analytes of interest are generally in low concentrations in cells is essential to perform single cell manipulation in microscale volumes in order prevent the analytes from being diluted below detection limits. Thus, microfluidic manifolds serve as an excellent microscale confined volume platform to manipulate and analyze single cells as the channels are compatible with typical eukaryotic cell sizes and volumes (Average volume and diameter of a eukaryotic cell are about ~3pL and ~10μm respectively).

The application of microfluidics for single cell analysis, especially for clinically relevant analytes has seen tremendous growth over the last decade.[21,22] An area of special interest is early-stage disease diagnosis. For example, in cancer metastasis, scientists are focusing on developing "point of care devices" to detect and concentrate rare circulating tumor cells (CTC). Less than one in a million cells in blood are CTCs. These microfluidic devices/ micro total analysis systems[22] also serve as powerful platforms manipulate cell prior to analysis using a variety of processing operations that use integrated softlithographic microvalves,[7,18] microwells,[23] microfluidic traps[24] and droplets.[25]

It has been almost 20 years since the first single cell analysis (SCA) report on microfluidic platforms was published. In 1998, Jed Harrison and coworkers developed a microfluidic device to lyse individual cells and examine β-galactosidase activity of the HL-60 cells using fluorescent detection.[26] Since then, this microfluidics based SCA has continued to advance through the

introduction of a variety of tools for the isolation, separation and detection of both single cells and their intracellular components.

Among many conventional SCA techniques, fluorescence based microscopy can be used to examine cell viability and cell proliferation in real time. Recently, this technique has been extended to the in-depth analysis of subcellular components.[27,28] Other techniques, such as flow cytometry, serve as a powerful method for the high throughput screening and characterization of single cells.[29] While these are powerful techniques, their information content is low as the number of analytes that can be analyzed is limited by the number of different fluorescent probes that can be detected simultaneously. In contrast the number of component that can be analyzed using a microfluidic single cell analysis device is only limited by the separation capacity of the system which can be upwards of 100 components. In addition, for fluorophores to be useful for microscopy and cytometry the fluorophore/substrate must undergo some type of fluorescence change to monitor cellular activity. Another major advantage of single cell analysis on microfluidic devices is that sample preparation can be automated and integrated into the same device where cell lysing and lysate separation occurs.[18] This is especially useful when an analyte of interest degrades over the time due to a short half-life, dismutations or scavenging.[30] Another significant challenge in cell lysing applications is significant dilution of the sample (lysed cell). Since the average volume of a cell is typically ~ 1pL, sample dilution is problem with conventional techniques where the injection volumes can be upward of 1 μL.. In contrast the injection volume on a microfluidic device is on the order of the volume of the cell. The injection of intracellular components under the influence of an electric field (i.e on-chip cell lysing followed by electrophoretic separation) helps to minimize random dispersion and keeps the analyte concentrations above the levels of limit of

detection and limit of quantification. In addition, rapid cell lysing minimizes the sample handling time and sample degradation issues.

1.5.1 Single cell lysing

Rapid cell lysis followed by rapid separations can allows one to examine many important cellular functions. Information about these functions is contained in the electropherograms of the cell lysates and include both peak characteristics (ex: peak shape) and separation characteristics (migration time, injection plug velocity, analyte diffusion and separation efficiency). In microfluidics based single cell applications a variety of lysing techniques, such as chemical, electrical, mechanical, optical and acoustic are used.

1.5.1.1 Electrically Induced Single Cell Lysing

The exact mechanism of electrical lysis is poorly understood. However, according to a widely accepted model, electrical cell lysing can be explained based on the principle of electroporation originally introduced by Zimmermann.[31, 32] When a cell is placed in an electric field, a potential gradient is created across the cell membrane known as transmembrane potential ($\Delta\varphi$).

The transmembrane potential φ at any point of interest on the cell membrane can be expressed in terms of the electric field strength (E), the radius of the cell (a) and the angle between the field line and an arbitrary point of interest (θ).

$$\Delta\varphi = 1.5aE \cos\theta \qquad (1.31)$$

When $\Delta\varphi$ exceeds a certain value, mechanical stress is generated and the cell membrane becomes permeable (**figure 1.19**). This is known as reversible electroporation. When, $\Delta\varphi > 1V$, thousands of nanopores form within the cell membrane and the membrane is irreversibly disrupted by the mechanical stress.[33, 34]

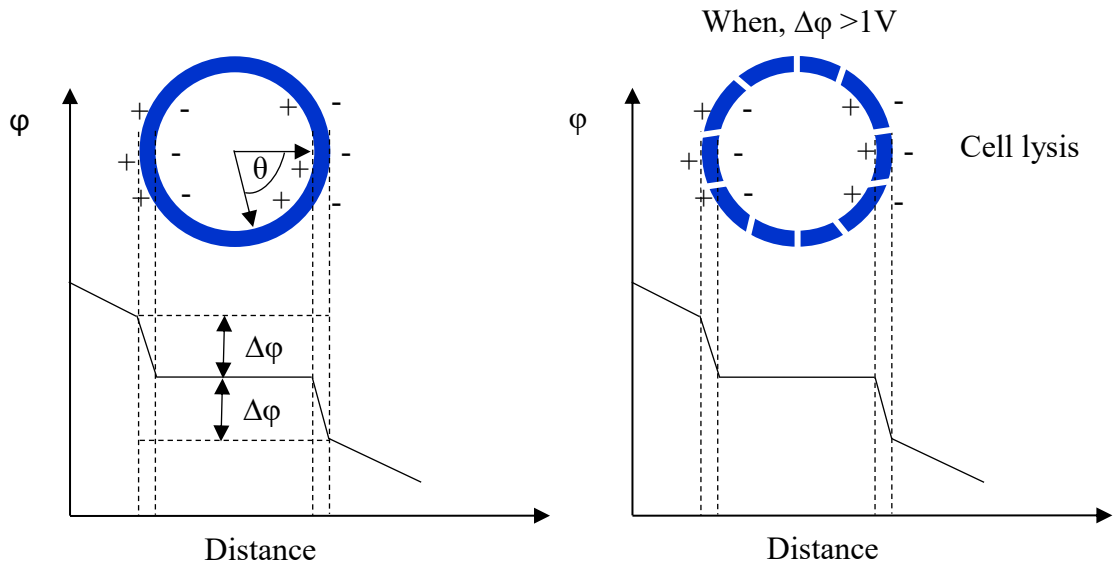

Figure 1.19: Electrical cell lysis. (a) When a cell is placed in an electric field transmembrane potential (Δφ) is induced across the membrane (b) The Cell is lysed if (Δφ) > 1V due to the mechanical stress

In electrical cell lysis, a strong electric field is applied across a microfluidic separation channel to irreversibly disrupt the cell membrane. This electric field is not only useful to lyse the cells but serves to electrophoretically separate intracellular components. This is a very useful technique in high throughput single cell analysis.[18] In this of type of SCA, cells are automatically transported and moving cells are exposed to a strong electric field for several milliseconds. Cells are then lysed, intracellular components are injected into the separation channel and an electrophoretic separation is performed under the influence of same electric field (**see figure 1.20**). More details of this technique will be discussed in Chapter 2.

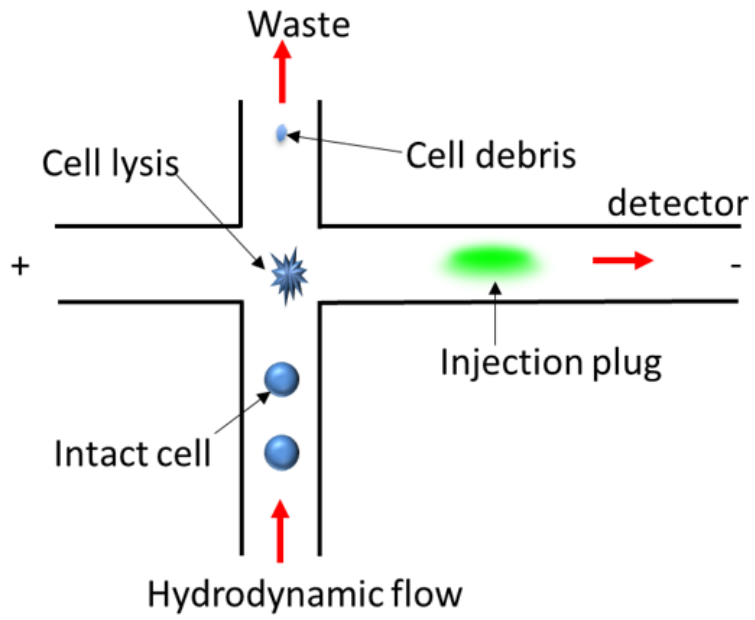

Figure 1.20: Schematic of an electrical cell lysing process of single cells using microfluidic device. Strong electric field (~750v/cm) is utilized to lyse the cells. Intracellular components then separated using the same electric field.

1.5.1.2 Low Voltage Single Cell Lysis

Single cell manipulation using electric fields is rarely reported in the literature. Most eukaryotic cells cannot survive in electric fields as membrane polarization causes electroporation. These cells are easily lysed in the presence of electric fields > 100V/cm. However, a recent approach demonstrated the use of very low electric fields (between 35-95V/cm) in microfluidic channels for cell transport with designed narrow regions where the electric field increases by ~20X that can be used for cell lysing.[33] The difference in the electric field strengths of channel sections with difference dimensions is due to changes in the relative resistances of these channel sections.. The resistance of a given channel section is inversely proportional to the cross sectional area of the channel. Hence, by varying the channel width while keeping the depth the same, the relative resistivities of the channel sections can be changed. The channel manifold in a microfluidic device is analogous to a resistor circuit in electronics.

When two microchannels of the same dimensions are connected by an orifice (short narrow channel segment) the electrical resistance in the orifice per unit length is much higher thus producing a very high electric field region.

According Ohm's law,

$$V = IR \tag{1.32}$$

where, V – voltage, I – current, R – resistance

This equation can be rearranged such that,

$$E = I\left(\frac{R}{l}\right) \tag{1.33}$$

where, E – electric field, l - length of the channel

The resistance per unit length (R/l) can be modulated by varying width of the channel. Hence, electric field strength can be modulated. Microfluidic channel segments were simulated using COMSOL Multiphysics software to optimize a microfluidic manifold for the electrokinetic transport of cells with selected orifices that could generate cell lysis. For example, if 200µm wide fluidic channel is tapered to a 20µm wide and 50µm long orifice, electric field strength is amplified by 10x (i.e width reduction ratio is 10). In contrast, by reducing width of the cell transport channel, the electric field distribution across orifice decreases significantly and may not be useful for cell lysing as shown in **Figure 1.19**.

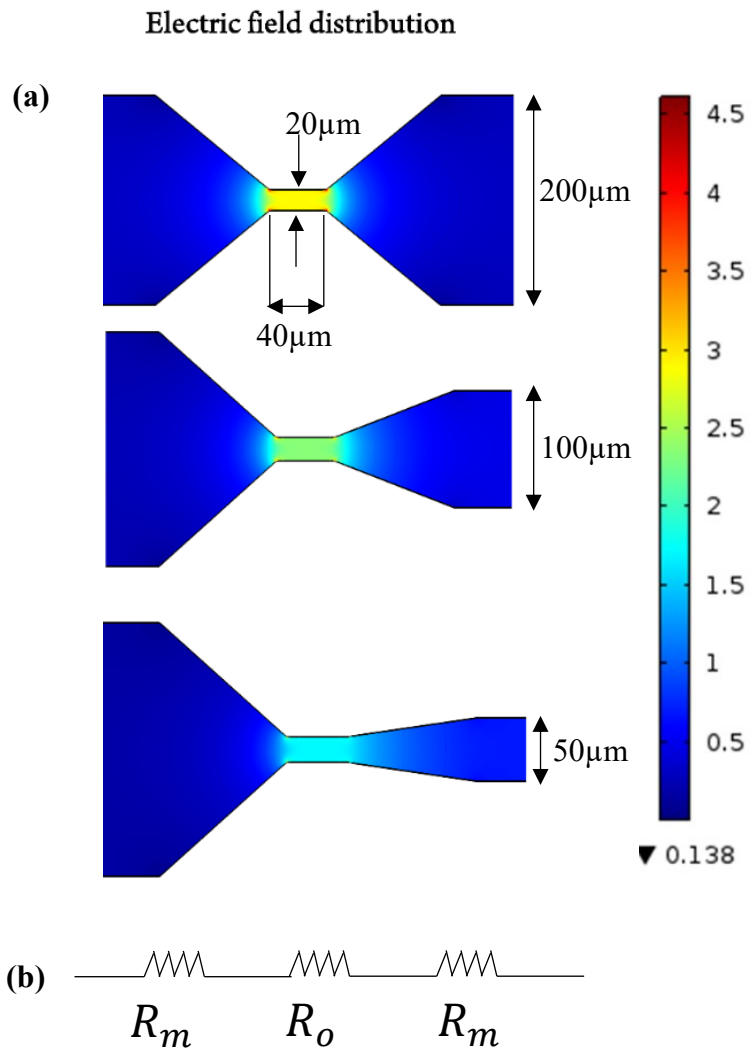

Figure 1.19: Electric field distribution across microchannels with different resistivities (a) Three microchannels are analogs to three resistors in a series. Where, R_m and R_o are resistance of microchannel and orifice respectively (b) when 200µm wide microchannels are connected with 20µm wide and 40µm long orifice, 10x stronger electric field is produced. Field strength is reduced down to 5x and 2.5x, when orifice is connected to 100µm channel and 50µm channel respectively.

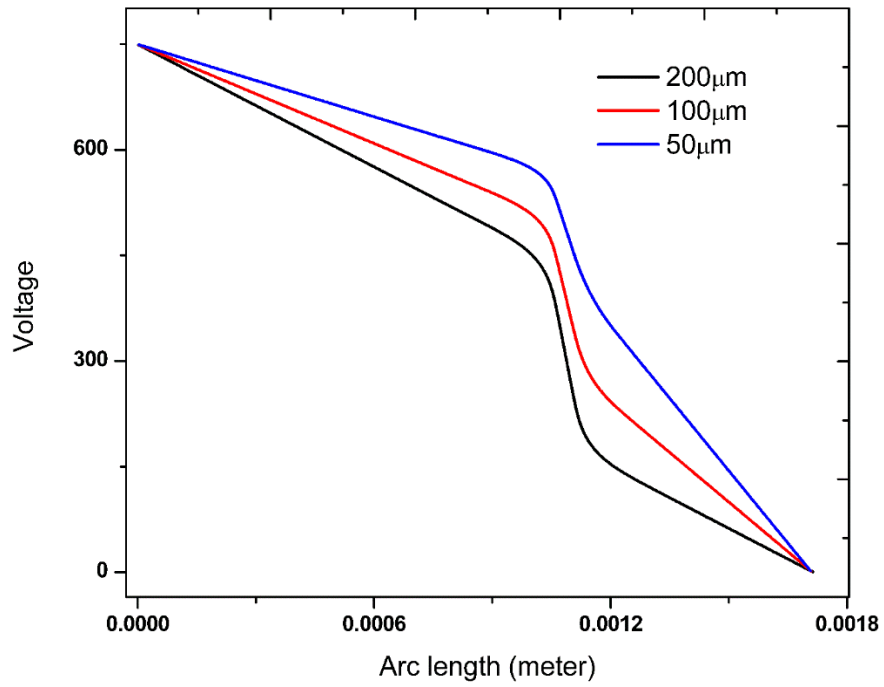

Figure 1.20: Voltage variation as a function of channel length when orifice is connected to microchannels with different widths.

One potential advantage of this technique is the ability to use low DC voltage power supplies to perform multiple cell operations using a rather simple channel manifold design (e.g. cell transport, lysing and electrophoresis) which might be potentially useful for point of care device development. In addition, due to the width reduction of the lysing region, significant dilution of the intracellular components can be greatly minimized. Furthermore, the microfluidic confined volume and the low Reynolds number regime minimizes analyte diffusion thus enabling increased detection sensitivity. Previously published work describing the use of this technique was limited to the transport and lysing of red blood cells (RBC). The average size of a RBC is 7μm. The microchannels in the previously published paper using the constricted channels to transport and lyse the RBCs were 10μm deep. They are too shallow to handle larger cells such as white blood

cells (Average size of white blood cell is 15µm). In addition, RBCs are difficult to lyse compared to WBC. As such, electrokinetic transport of WBC should require even lower E-fields.

The previously reported microfluidic manifold was redesigned to perform the electrophoretic separations at < 200V/cm field strengths while providing 4X greater electric field for lysing cells and 4X smaller electric field for cell transport. For the device tested below 75V/cm, 600V/cm and 150V/cm field strengths were maintained in the desired regions of the separation channel in order to transport cells, lyse the cells and electrophoretically separate the analytes, respectively.

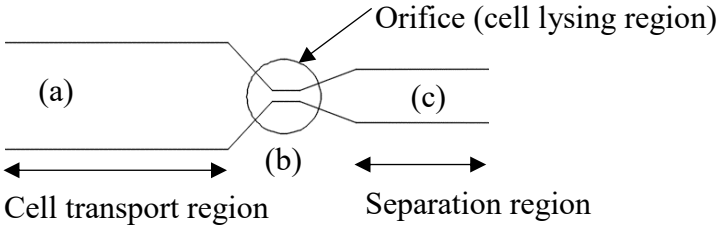

Figure 1.21: Separation channel that composed of cell transport region (200µm wide), lysing region (25µm wide) and separation region (50µm wide). Field strengths of region (a), (b) and (c) were 75V/cm, 600V/cm and 150V/cm respectively.

Low voltage cell lysing is potentially useful in microchip electrophoresis coupled electrochemical detection. In such applications, cell the lysing electric field can interfere with the electrochemical detection setup. Thus, high amplitude background current is generated and that prevents any analyte detection. Troubleshooting such detection issues with low voltage cell lysing technique will be discussed in Chapter 3.

1.5.1.3 Other Types of Cell Lysing

Many other cell lysing strategies including mechanical,[35] thermal,[36] acoustic,[37] and laser induced[38] methods are potentially useful in single cell applications. Some of those techniques are not compatible with separation and detection setups or they are expensive and time consuming. However, the most suitable lysing method has to be chosen depending on the application type. Among all of these techniques, one of the most efficient, fast, easy and cost effective single cell lysing techniques is the electrical cell lysis. In all the following chapters, electrically induced single cell lysis based microfluidic SCA applications will be discussed.

1.6 Conclusions

The fundamentals of microfluidics, electrophoresis and single cell analysis have been discussed. Microfluidics is a powerful platform that allows exploring a variety of sample manipulation, separation and detection techniques. These platforms continue to advance in many research areas including engineering, biology, medicine, environmental science and forensic analysis. A variety of miniaturized microfluidic tools have been developed in order to perform multiple sample handling and analysis functions. Multilayer softlithgraphic techniques have been developed for the fabrication of thousands of permutations of microfluidic valves, pumps and switches. Two layer microfluidic devices can easily be adapted to perform single cell analysis via automated fluid pumping. The major reason for gaining popularity in SCA research field is ability of discriminating cell heterogeneity in terms of both physical and biological aspects. Electrical cell lysing techniques are well suited with most of the on-chip high throughput single cell platforms. Electrically induced lysis allows for the automation of cell lysing and the separation of intracellular

components in real time. Electrical cell lysis is simple, fast, easy and low cost techniques that is compatible with high throughput single cell manipulating platforms.

Chapter 2 - High Throughput Microfluidic Device for Single Cell Analysis using Multiple Integrated Soft-lithographic Pumps

The majority of this chapter is reproduced by permission of the Elsevier.

Published as: Damith E.W. Patabadige, Tom Mickleburgh, Lorin Ferris, Gage Brummer, Anne Culbertson and Christopher T. Culbertson.*

Electrophoresis, **2016.** *37* (10), 1337-1344.

2.1 Introduction

The development of microfluidic and Lab-on-a-Chip systems for the analysis of single cells has made tremendous strides over the last decade. Several devices for cytometry,[39, 40, 41] the analysis of cells in droplets,[42, 43, 44] the culturing and interrogation of fixed cells,[45] and the continuous analysis of individual cells and their lysates have been reported.[46, 47] One advantage of transporting and lysing cells, followed by the separation and detection of the cell lysates is the ability to increase the information content of the system. Multiple components in the lysate can be separated and then detected and quantified using multiple detection modalities. This increased information content can help better distinguish otherwise phenotypically similar cells. There are, however, two limitations for this type of single cell analysis. The first limitation is the ability to control the fluid flow well enough to ensure complete injection of the lysate into a separation channel from run-to-run and from chip-to-chip. The second limitation is the limited number of cells that can be analyzed due to low throughput or limited cell viability times.[48, 49]

Approaches to generate fluidic pumping on-chip for cellular analysis have almost exclusively concentrated on the application of some external force to the termini of the channels to generate the fluid flow. These methods include the use of syringe pumps,[46, 30] pressure,[48, 50] vacuum[49, 51]

or simply differences in reservoir fluid heights.[47] Electroosmosis[33, 52, 53] has also been used, but many cells types are very sensitive to electric fields and so this approach is limited. One of the major drawbacks of using external driving forces is the precision and accuracy of the force that can be applied to make small changes in fluid flows in the channels. In addition, there is often a time lag when making the force change and when the fluid flow in the channel reaches equilibrium. This makes it difficult to robustly design devices with balanced flows at intersections. One approach to increasing the ease of use of these devices would be to integrate the flow generation mechanism directly in the microfluidic manifold. Such pumps known as monolithic microfabricated pumps have been reported previously by the Quake group.[7, 20, 54, 55] These pumps have been applied to a variety of chemical and biological processing operations on microfluidic devices.[10, 56, 57] They have also been demonstrated previously for the transport of prokaryotic cells,[7, 54, 55] but have not been used for the transport of eukaryotic cells most likely as the transport rates are too low to generate sufficient analysis rates and because the channels previously reported are too shallow to move typically sized eukaryotic cells through them.

Although many interesting techniques have been reported for eukaryotic single cell lysing and continuous analysis, most of these techniques, are only capable of performing the analysis for a short period of time[30] or suffer from low throughputs such as (20-40) cells/h.[48, 50, 58, 59] Recently, however, some higher throughput devices have been reported and include a screening platform that was used to image 1020 cells, but this platform did not integrate lysis and separation.[60] In another approach cells trapped in microarrays were integrated with an automated CE system to study S1P enzyme activity of natural killer cells extracted from human blood.[61] Approximately 120 single cells were lysed by pulsed laser followed by lysate injection and electrophoretic separation. This approach, however, is relatively time consuming and complex compared to an

automated and integrated microfluidic system. Other reports of high throughput single cell analysis over the past decade have generally used external hydrodynamic forces to transport cells including a couple of devices capable of analyzing 100-300 cells/h for a maximum of 108 and 300 cells respectively.[47, 49]

In this work, we have developed a high throughput microfluidic device for single cell analysis that integrates multiple peristaltic pumps into a microfluidic manifold to improve fluid flow control and to increase flow rates. T-lymphocytes (Jurkat cells) were loaded with carboxyfluorescein diacetate (CFDA) and Oregon green diacetate (OG) off chip. The labeled cells were then added into a reservoir after which cell transport, cell lysis, analyte injection and analyte separation were performed in an automated fashion. The integrated pumps allowed much better control over the fluid flow in the channel manifold than previously reported external fluid generation systems.[48, 51, 62] 1120 cells were transported to the lysis intersection and the lysates from these cells were successfully injected and detected over an 80 min run for an analysis rate of 14 cells/min or ~1000 cells in the 1st hour. Of these cells 491 single cell electropherograms were analyzed. The average analyte migration time CFDA peak areas remained consistent within experimental error over the 1st hour of the run and no cellular debris accumulated in the channels.

2.2 Materials and Methods

2.2.1 Reagents and Materials.

Anhydrous dimethyl sulfoxide (DMSO) was purchased from Sigma-Aldrich (St. Louis, MO, USA). Ethanol (95%) and isopropyl alcohol were obtained from Fisher Scientific (Pittsburgh, PA, USA). SU-8 2010 was obtained from MicroChem Corporation (Newton, MA, USA). SU-8 developer, (2-(1-methoxy)propyl acetate), was purchased from Acros (Morris Plains, NJ, USA). Silicon wafers, 4 inches (100 mm) in diameter, were purchased from Silicon Inc. (Boise, ID, USA).

Sylgard 184 polydimethylsiloxane (PDMS) prepolymer and curing agent were acquired from Ellsworth Adhesives (Germantown, WI, USA). 18MOhm water was generated using a Millipore Synthesis A10 system (Billerica, MA, USA). 6-Carboxyfluorescein diacetate (6-CFDA) was obtained from Anaspec (Freemont, CA, USA), and Oregon Green 488 diacetate (OG) was purchased from Molecular Probes (Eugene, OR, USA).

2.2.2 Cell Culture.

T-Lymphocyte cells from the Jurkat Clone E6-1 cell line (ATCC TIB-152 American Type Culture Collection, Rockville, MD, USA) were cultured in RPMI 1640 medium containing 10% (v/v) fetal bovine serum, L-glutamine (2mM), penicillin (100 µg/ml) and streptomycin (100 µg/ml). The cells were maintained in a humidified environment at 37℃ and 5% CO_2 and cultured in 25 mL polystyrene culture flasks (Becton Dickinson Labware, NJ, USA). Cells were passaged every 2 to 3 days.

2.2.3 Cell Preparation.

Two fluorescent probes were used in the experiments reported below: 6-CFDA and Oregon Green-diacetate. Both of these fluorogenic dyes are cell permeable. Once inside of the cell they are hydrolyzed by intracellular esterases. The hydrolyzed products are fluorescent and trapped inside the cells because they are negatively charged. The dyes were loaded in a stepwise manner into the cell suspension. In the first experiment reported below, which ran for 80 continuous minutes, 0.2 mM 6-CFDA and 0.2 mM Oregon Green-diacetate were aliquoted into the culture flask and allowed to incubate with the cells for 20 min. In the second experiment, which ran for 30 continuous min, 0.16 mM 6-CFDA and 0.2 mM Oregon Green-diacetate were aliquoted into the culture flask and allowed to incubate with the cells for 20 min. After the incubation period, the

Jurkat cell suspension was centrifuged at 2000 rpm for 2 min and the supernatant was removed. Cells were washed twice, resuspended in sterile PBS and centrifuged again. The supernatant was then removed and the cell pellet was resuspended in 2% BSA containing sterile PBS. The labeled cells were then loaded into the sample reservoir of the microchip.

2.3 Microchip Fabrication.

Multilayer microfluidic devices were fabricated in a manner similar to that reported previously.[7] Pneumatically controlled channels were constructed using a negative tone photoresist SU-8 2010. The SU-8 was spin-coated (1000 rpm for 45 s) onto a 4-inch (100 mm) diameter silicon wafer (Laurell Technologies Corp., North Wales, PA, USA) to an approximate height of 20 μm. The wafer was soft baked at 65℃ for 2 min, followed by a hard bake at 95℃ for 4 min. A photo mask containing the desired channel features was aligned on the photoresist layer and exposed to UV light (ThermoOriel, Stratford, CT, USA). The wafer-photoresist complex was washed with SU-8 developer to remove the unpolymerized photoresist. The wafer was further rinsed with isopropyl alcohol followed by deionized water (Barnstead E-pure system, Dubuque, IA, USA) to fully develop the exposed features. The fluidic channels were constructed using the positive tone photoresist AZ-4620. This photoresist was spin-coated (1000 rpm for 18 s) onto a cleaned silicon wafer (~20 μm thickness) followed by soft baking (65℃ for 2 min) and hard baking (95℃ for 4 min). The photoresist was then exposed through a transparent mask containing the desired features. The features were developed using AZ 1:4 developer followed by a deionized water rinse. To obtain hemispherical shaped channels, the AZ mold was baked at 120℃ for 2 min and allowed to cool to room temperature. A 5:1 mixture of PDMS prepolymer to curing agent was poured onto the SU-8 mold to produce a 5-6 mm thick layer of PDMS. A 30:1 mixture of PDMS prepolymer

to curing agent was spin-coated (2000 rpm for 30 s) onto the AZ mold producing a 50 μm thick elastomeric layer. Both the AZ and SU-8 molds were cured at 80℃ for 90 min. The pnuematically controlled channel PDMS layer was carefully peeled off the SU-8 mold and holes were punched. The layer was carefully aligned on top of the fluidic channel PDMS layer. Both layers were cured together for an additional 90 min at 80℃. After curing, the two layers were irreversably fused and were peeled off the AZ mold as a singular PDMS layer. Holes were then punched in the fluidic channels. The channel manifold in the PDMS layer was then contact sealed against a clean glass substrate.

2.4 Device Operation.

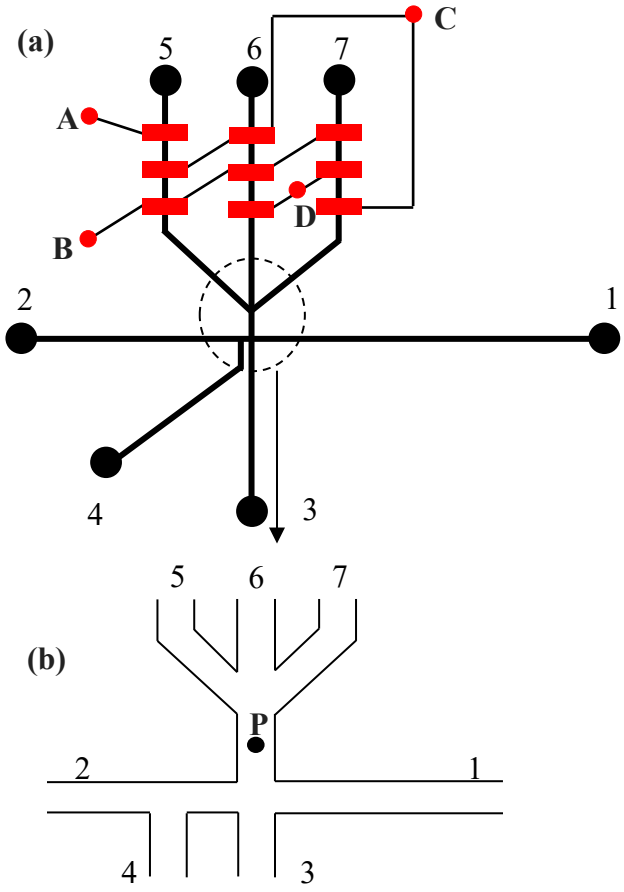

Figure 2.1: (a) Integration of nine micro valves with fluidic channel network (2-D view). Nine micro valves are interconnected to four inlets to actuate the valves pneumatically (b) Cell lysing intersection of microfluidic channel network.

Prior to the loading of cells, all the fluidic channels of the microfluidic chip were filled with running buffer by applying a vacuum to the end of channel 6 (**see fig. 2.1**). The running buffer was composed of 0.20% (w/v) Tween20, 20%(v/v) acetonitrile, 2%(w/v) bovine serum albumin, 25 mM sodium borate and 2 mM sodium dodecyl sulfate(SDS). T-lymphocyte cells loaded with fluorescent dyes and suspended in sterile PBS with 2% BSA (w/v) were added to the sample reservoir (label 3 in **Figure 2.1**). The waste channels are labeled 5-7 in **Figure 2.1**. The air inlets

used to regulate the peristaltic pumps are labeled A-D. Air was pumped at the pressure of 0.8 bar and frequency of 100Hz to actuate the microvalves that form the peristaltic pumps. Four inlets were connected to the top elastomeric layer in order to actuate the peristaltic pumps. Labview 8.2 software and in-house written programs were used to regulate the pumps. The pumping sequence was controlled using solenoid valves (The Lee Company, Westbrook, CT, USA) that were interfaced to the computer via an NI USB-6009 analog-to-digital converter (National Instrument, Austin, TX).

2.4.1 Pumping Mechanism

To operate this device nine microfluidic valves are positioned over three parallel fluidic channels (**Figure 2.1a**). The valves are actuated in the following sequence: 101,100,110,010,011 and 001; where 1 and 0 represent "closed valve" and "opened valve" respectively[7]. The valves are groups into 3 sets of 3 to better coordinate the valve actuation on each channel. Four solenoid valves were used to control the flow of air needed to actuate the valves.

The mechanism of fluid pumping in the middle fluidic channel is represented in following optical micrographs (**figure 2.2a**) and schematic diagram (**figure 2.2b**). Fluid is pumped by continuous actuation of the on-off valves in a given row. At 0 ms, the 1st valve is actuated and it pushes the fluid in both the forward and backward direction. After 10 ms, a 2nd valve is actuated while the 1st valve is still on. The 1st valve prevents back flow generated by the actuation of the 2nd valve and hence, 2nd valve pumps the fluid only forward direction. Similarly, at 30 ms, the 3rd valve is actuated while the 2nd valve is remains on. The 3rd valve pushes the fluid further in the forward direction without generating any back flow. At 40ms, the 2nd valve is off in order to start the next cycle. After another 10ms, the 1st valve is actuated and a second fluid pumping cycle is initiated.

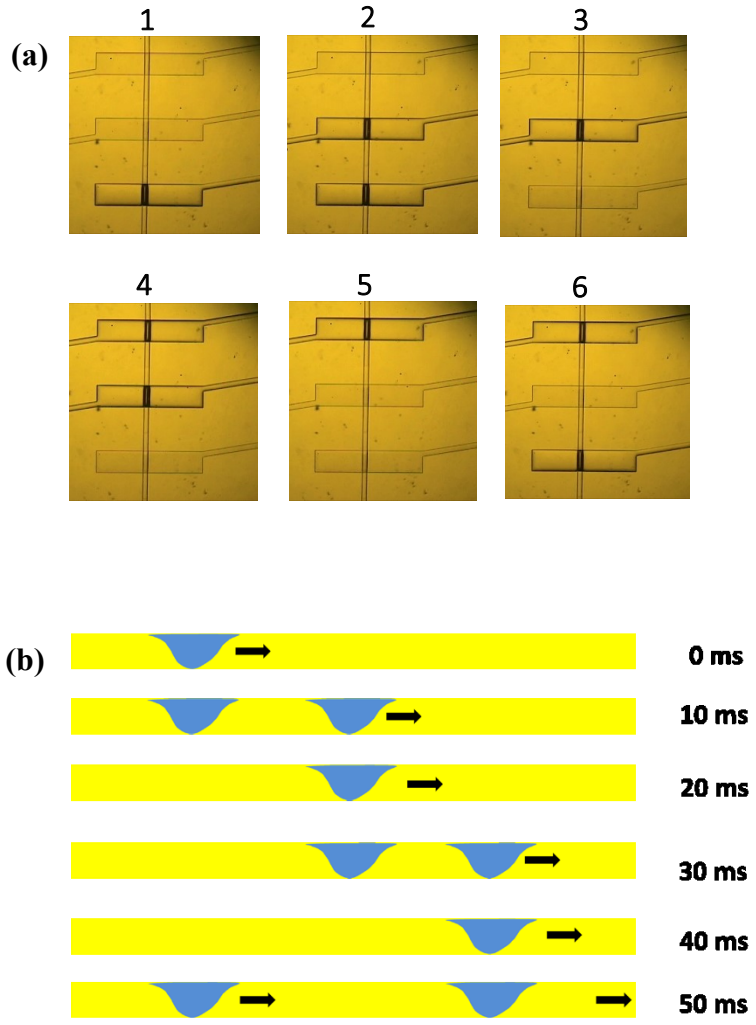

Figure 2.2: (a) Actuation cycle of three on-off valves in the middle raw; each solenoid valve is actuated after 10ms delay. First pumping cycle ends after 50 ms. (b) Schematic representation of fluid pumping when peristaltic pumps are actuated

2.5 Detection.

A multi-line Argon-ion laser (MellesGriot Laser Group, Carlsbad, CA, USA) was used as the excitation source. The 488 nm beam was selected using a dispersive prism and directed into a Nikon eclipse TS100 microscope (Nikon Instruments Inc., Melville, NY, USA) through the rear port and a 20X objective (Plan Fluor, Nikon) to the microscope stage. The beam was focused on a

small spot in the separation channel 1-2 mm downstream from the lysis intersection. The fluorescence emission from the dyes was detected by a photomultiplier tube (Hamamatsu Instruments, Bridgewater, NJ, USA) attached to the trinolucular port of the microscope. The signal was amplified using a low noise current preamplifier at 50 μA/V with 100 Hz low-pass filter (Stanford Research Systems, Sunnyvale, CA, USA) and sampled at 100 Hz using a PC1-603E I/O card (National Instruments, Austin, TX, USA). In-house programs using LabVIEW (National Instruments, Austin, TX, USA) were used to control the high voltage power supply and data acquisition. Data analysis was performed using Igor Pro (WaveMetrics, Portland, OR, USA). Video images were collected using a digital color video camera (ExwaveHAD Sony Corperation, Japan) mounted on the side port of a Nikon TE-2000-U inverted microscope (Melville, NY, USA). Frame grabs were used to calculate the flow rate of analytes down the separation channel.

2.6 Results and Discussion

2.6.1 Device Characterization.

Flow rates in the fluidic channels with integrated 1 and 3-channel peristaltic pumps were characterized both as a function of the valve actuation frequency and the pressure applied to actuate the individual valves in the pump(s). Characterization was performed by measuring the distance 10μm diameter fluorescent polystyrene beads moved as a function of time by analyzing video frames taken while monitoring the beads flowing in the channel manifold through a microscope. For the devices characterized below all of the channels were 50μm wide and 17-20μm deep. Previously, flow rates have been shown to depend upon several factors such as actuation pressure, actuation frequency, dimensions of the fluidic channels, effective area of the on-off valves and gap between pumps.[7, 63] As expected, the flow rate increased as actuation pressure increased (**Figure**

2.3) up to 1.2 bar where sufficient pressure was applied to completely close the channels. Flow rates were also a function of actuation frequency. The highest flow rates for all actuation pressures and for both the 1 and 3-channel pump configurations were found to be in the range of 125-166 Hz. The maximum volumetric flow rates for the 1 and 3-channel pumps were 4 nL/s and 9.2 nL/s, respectively. The single channel pump maximum volumetric flow rates correspond nicely with previous reports of such pumps that generally that have been reported to be in the 1-3 nL range.[7] As with previously reported devices, for pumping frequencies above 166 Hz the elastomeric membrane does not seal the channel completely hence, the pumping efficiency decreases.

For the chips reported here, pulsatile flow was minimized as pumping frequencies were increased (>66 Hz). Three channel valves further reduced the pulsatile nature of the flow compared to 1 channel configuration as each of the pumps was actuated 120˚ out of phase with each other in the 3 different channels.

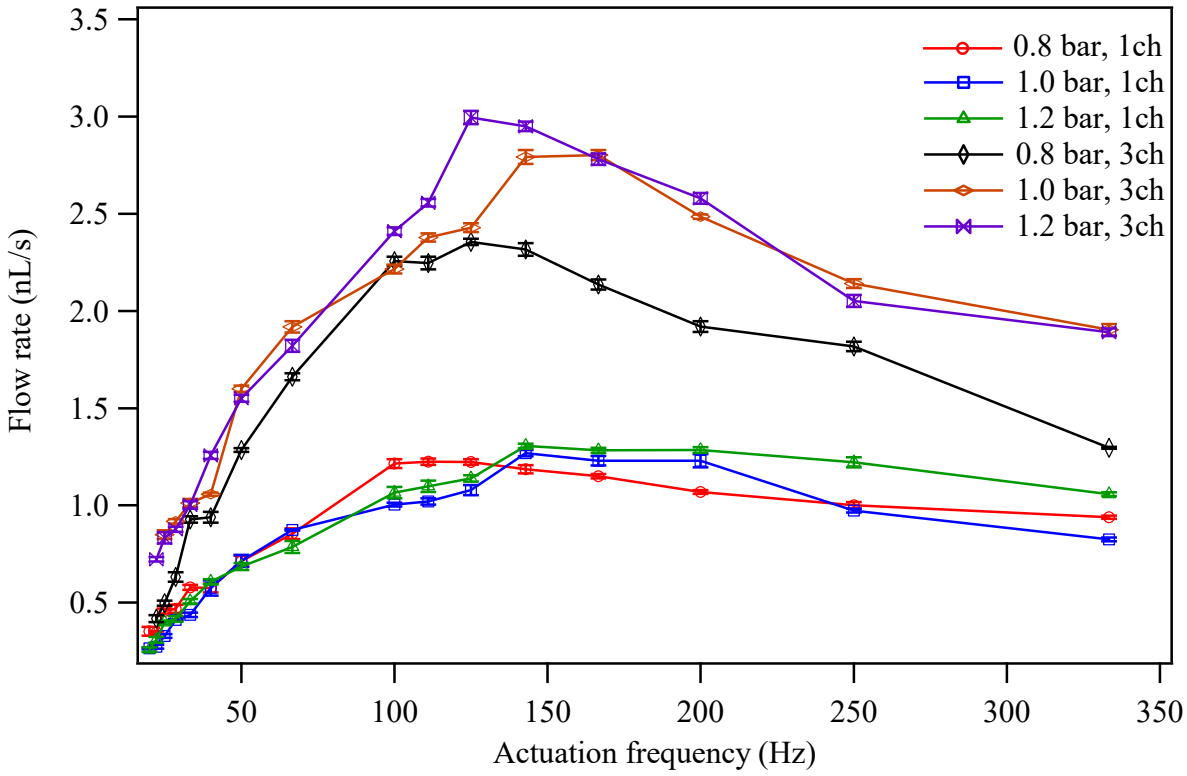

Figure 2.3: Flow rate vs. actuation frequency. Flow rates were measured in cell transport channel at point P (Fig 1b) (10µm fluorescent beads were placed in reservoir 3).

3.6.2 Cell Lysis and Analyte Injection.

Cell lysis and the electrophoretic separations were both performed using an electric field strength ~700 V/cm. Cells were transported to the lysis intersection using a chip with 3 integrated peristaltic pumps. At the intersection, cells were lysed, and the negatively charged analytes injected into the separation channel in <33 ms (i.e. one video frame) (**Figure 2.4**). The efficiency of the injection was a function of the flow rate and applied electric field (**Figure 2.5**). For the separations reported below, the 3-channel device was actuated at a frequency of 100 Hz and a pressure of 0.8 bar which resulted in an injection efficiency of ~100%. The 3 pump system provided a strong hydrodynamic flow and effectively carried much of the cell debris away from the intersection through the pumping channels.

This, in addition to the 0.2% tween 20 and 2% BSA buffer, helped to minimize the adhesion of cell debris to the walls allowing the devices to operate continuously for several hours without blockage.

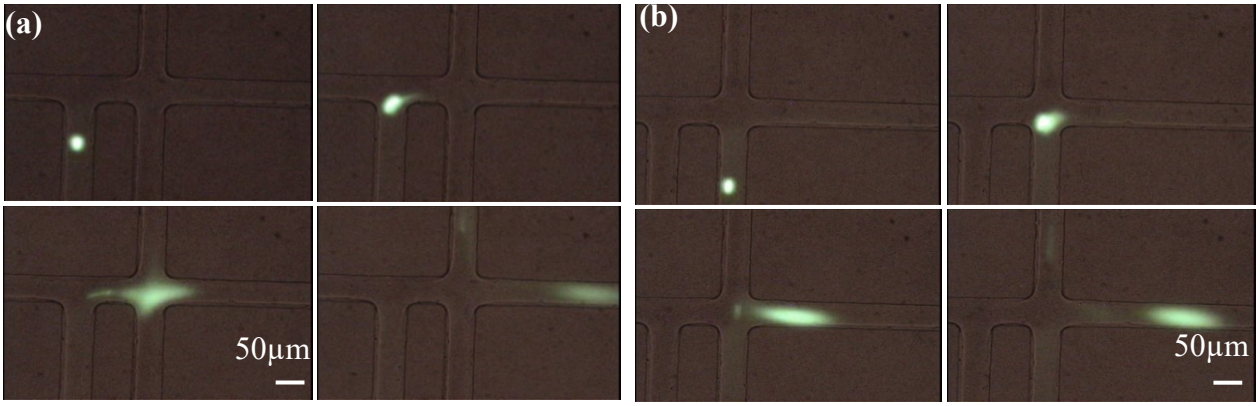

Figure 2.4: (**a) Magnified (20×) images of cell lysis. The field strength was 700 V/cm. Cells were placed in reservoir 4. Cells debris and lysate are moving along with hydrodynamic flow and electroosmotic flow respectively. (b) Magnified (20×) images. The field strength is 700V/cm, and cells were placed in reservoir 3. Sharper and narrower injections could be achieved with this configuration compared to previous configuration.**

Fluorescently labeled cells were placed in reservoir 3 or 4 (**Figure 2.1a**). The other reservoir was used to dilute the cell buffer and was filled with run buffer. Placing the cells in reservoir 3 and the diluent in reservoir 4 resulted in less dilution of the cell lysis injection plug and higher efficiency injections and so this was the arrangement used for the separations reported below.

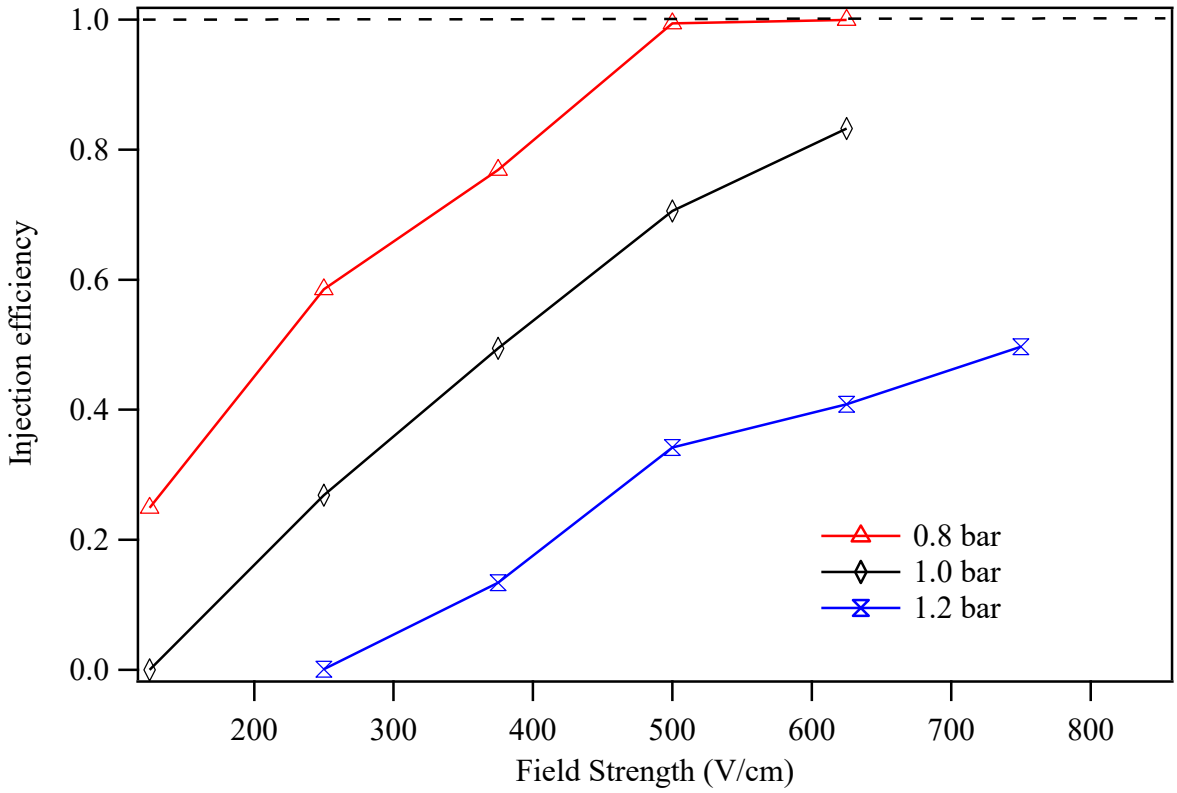

Figure 2.5: Injection efficiency vs. field strength. Injection efficiency varies as a function of actuation pressure and the field strength.

2.6.3 High Throughput Analysis.

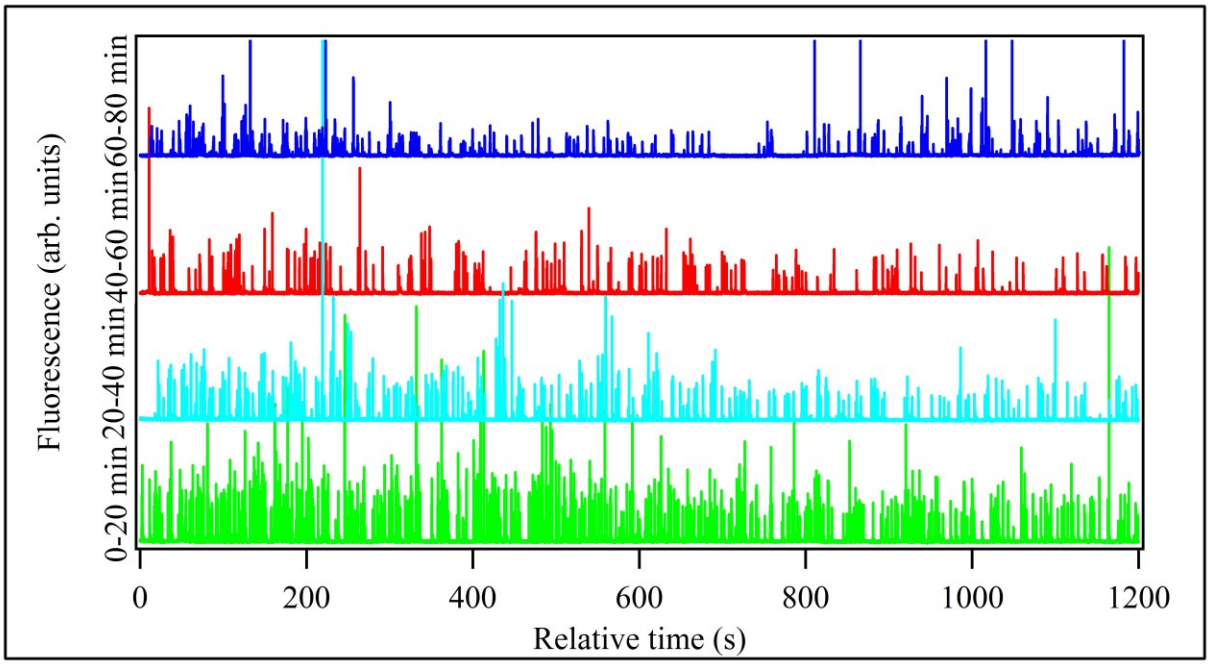

Figure 2.6: Fluorescence vs. relative migration time for 1120 single cell electropherograms split into 4 consecutive 20 min runs.

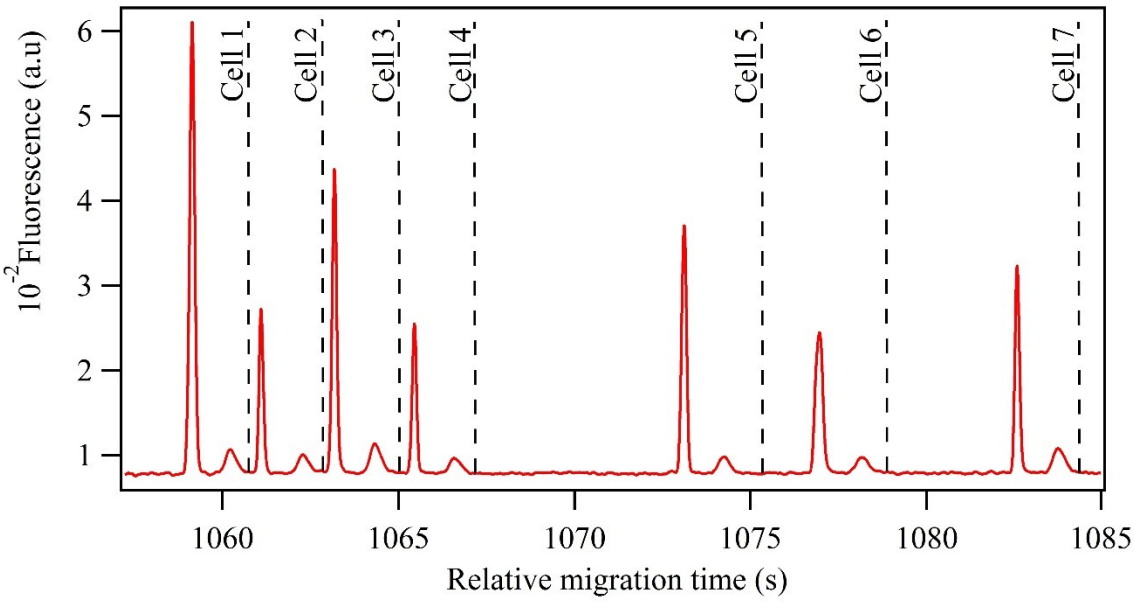

Figure 2.7: Expanded view of Figure 2.6. Separation of CFDA (1st peak) and OG (2nd peak).

To demonstrate the stability and high throughput capabilities of the system, the cells were loaded with 6-CFDA and OG diacetate off the device. They were then added to reservoir 3 at a density of ~1 x 10^5 cells/mL and transported through the microfluidic manifold using the 3-channel pumping system. The total flow rate for the initial experiment was ~6 nL/s at point P and ~2nL/s in the cell transport channel (i.e. channel 3). The cells were continuously lysed over an 80 min period of time. The 80 min run shown in **Figure 2.6** was divided into 4 consecutive 20 min runs in order to periodically save the data and to refresh the cell reservoir from the same stock cell solution. For each single cell electropherogram shown in **Figure 2.7** the first peak is from the hydrolyzed 6-CFDA and the second peak is from the hydrolyzed OG. Approximately 1120 cells were detected over the 80 min run resulting in an average single cell analysis rate of 14 cells/min. This rate compares nicely with previous reports of single cell analysis on microfluidic devices.[30, 46] Of the 1120 single cell electropherograms collected, approximately 491 (44%) were fully resolved from the previous and subsequent single cell electropherograms. If one assumes that the cells enter the lysis intersection stochastically then the number of fully resolved electropherograms expected can be estimated using the statistics of peak overlap developed by Giddings.[64] In this case the number of non-overlapping single cell electropherograms expected if they are randomly distributed across a separation space can be estimated from the number of expected electropherograms (m) and the peak (i.e. electropherogram) capacity of the separation system (n_c):

$$s = \exp(-\frac{2m}{n_c}) \tag{2.1}$$

The number of expected single cell electropherograms can be determined from counting the number of large CFDA peaks and the single cell electropherogram capacity can be determined by dividing the time of a single cell electrophoerogram (i.e. 1.5-2.0 s) by the total run time (i.e. 80

min). From these inputs, eq 2.1 predicts that the number of expected fully resolved single cell electropherograms should be between 440-572 which matches nicely the 491 fully resolved single cell electropherograms actually detected. This makes the effective cell analysis rate for completely resolved electrophorograms ~6 cells/min. For future applications deconvolution algorithms could increase the effective rate.

2.6.4 Separation Parameters.

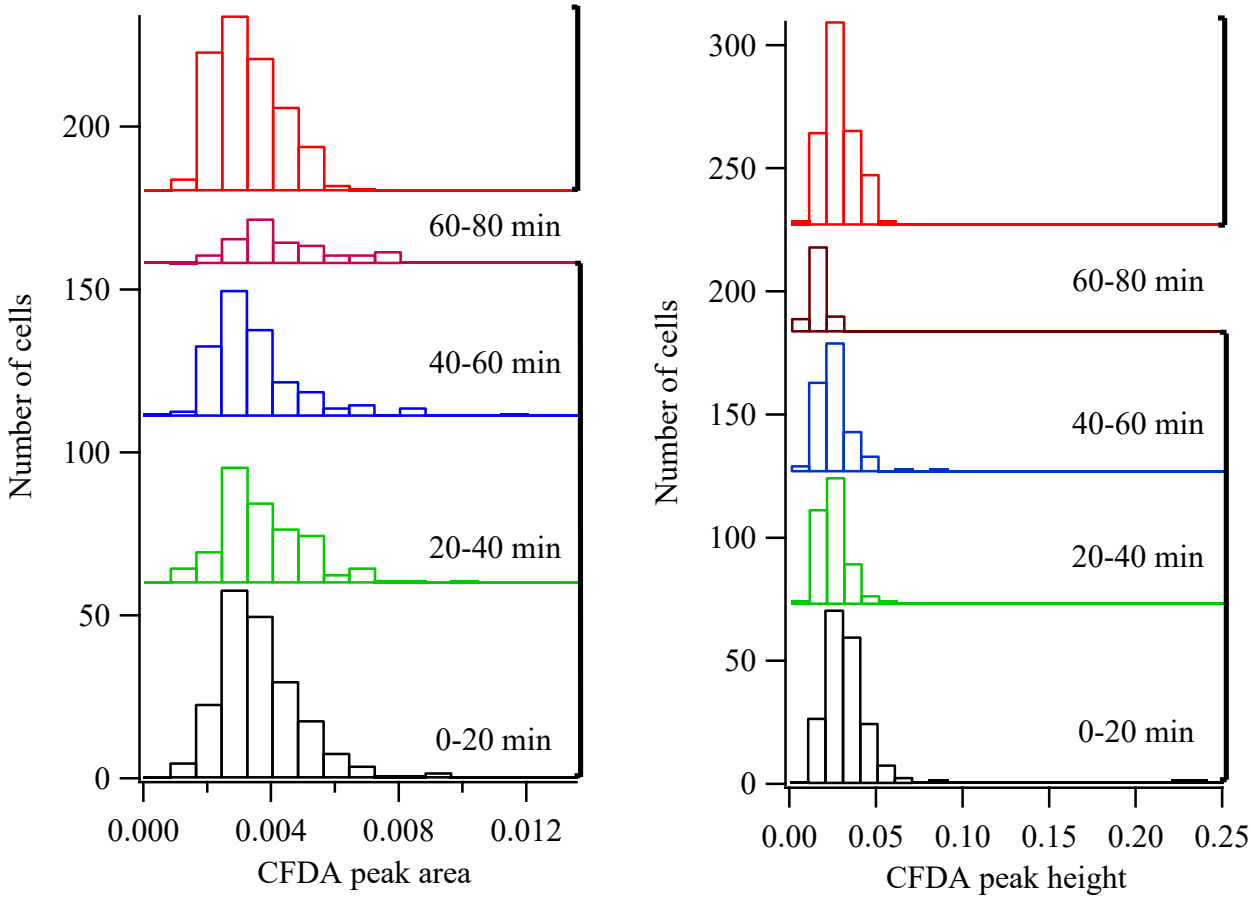

Figure 2.8: Distribution of CFDA peak areas and peak heights. Histograms of 1st run, 2nd run, 3rd run and 4th run are shown in black, green, blue and brown colors respectively. Histogram of 30 min run is given in red color.

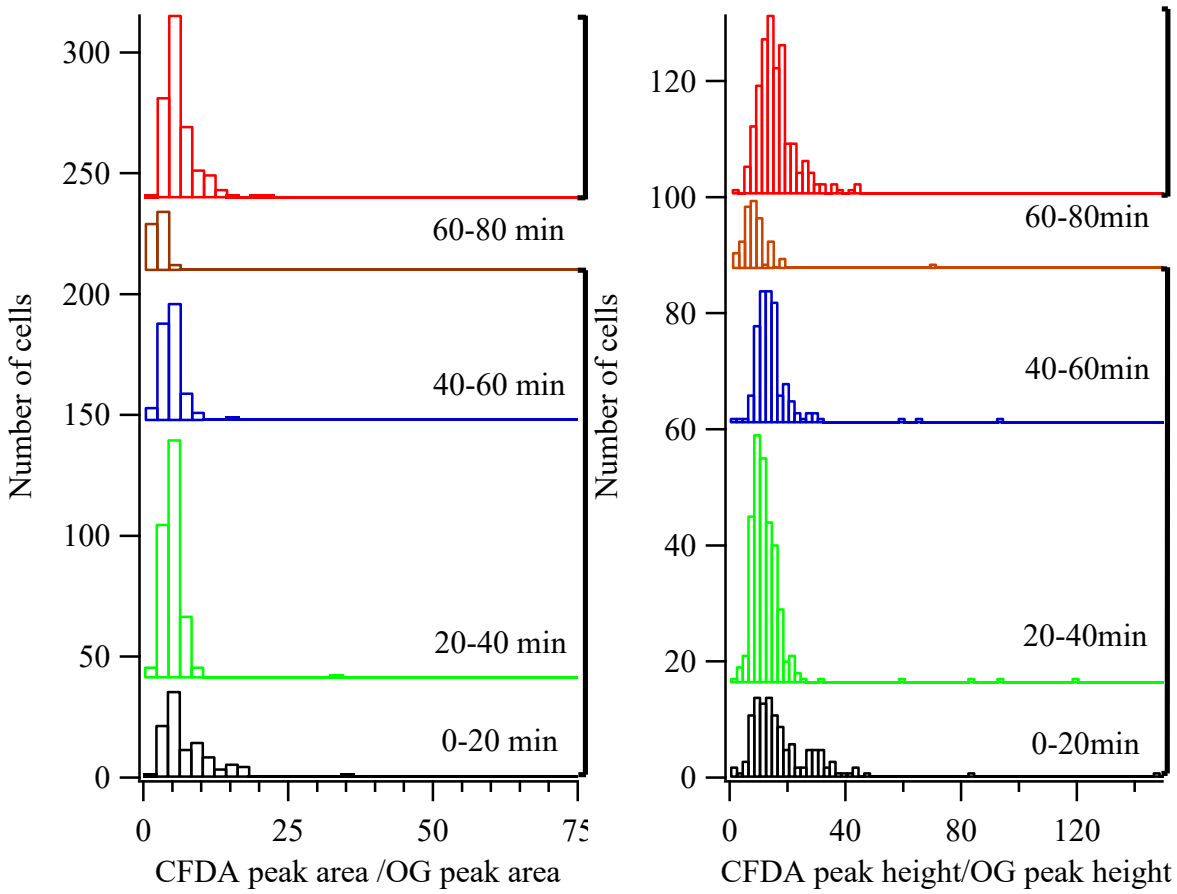

Figure 2.9: Distributions of CFDA peak areas/ OG peak area and CFDA peak height/ OG peak height. Histograms of 1st run, 2nd run, 3rd run and 4th run are shown in black, green, blue and brown colors respectively. Histogram of 30 min run is given in red color.

In order to determine the stability and robustness of the injections, the peak areas and heights, resolution, and peak widths for the cells were examined over the course of the 80 min run. The average and standard deviation of the CFDA peak areas and peak heights can be seen in **Figure 2.8** The average CFDA peak areas for the 4 consecutive 20 min run segments were 0.0037±0.0014 (n=202), 0.0038±0.0015 (n=119), 0.0034±0.0015 (n=121) and 0.0043±0.0016 (n=49) respectively. Median values for the consecutive runs were 0.0035, 0.00340, 0.0032 and 0.00380 respectively. The peak area and peak height distributions for the first 3 20 min run segments are very similar to one another. They follow the distribution expected for an asynchronous steady-state population of immortalized cells assuming that the fluorescent dye intensity variation is due to cell size.[65] A line fit through the data had a slope of ~0 and a correlation coefficient of 0.001 indicating no significant change in the average injected cell volume (**see fig. 2.10**). After 60 min the cells began to clump and the CFDA began to leak out of the cells resulting in more erratic data. The peak area and height ratios of CFDA/OG reflect the same trend. However, OG is relatively more unstable inside cells compared to CFDA over long period of time. More variations can be observed for peak area and height ratios of CFDA/OG (**figure 2.9**).

Table 2.1: Variation of mean migration time and RSD% for 4 consecutive runs (80min) and 30min run

80min Run	Mean	Stdev	RSD%	No. of Cells analyzed
Sample 1	1.12	0.12	10.2	202
Sample 2	1.64	0.27	16.5	119
Sample 3	1.97	0.20	10.3	121
Sample 4	2.56	0.67	26.3	49
30 min Run	**Mean**	**Stdev**	**RSD%**	**No. of Cells analyzed**
Sample 1	0.79	0.08	10.6	185

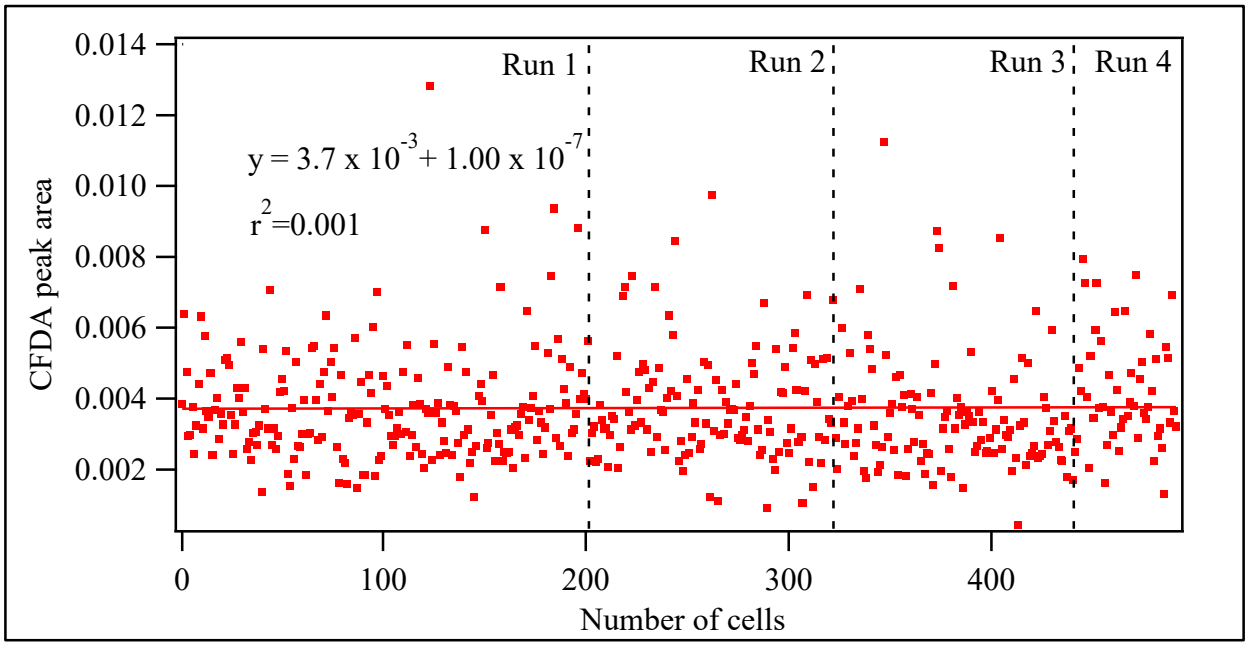

Figure 2.10: Peak area of CFDA calculated for 491 cells. The fitted line shows essentially no change in average value over 80 min.

As absolute migration times cannot be measured, other separation parameters such as relative migration time can also be used to examine the stability of the separation system with time. The

relative migration times of analytes changed over the time of the 80 min run. For the 4 consecutive 20 min periods the average relative migration times for the OG-CFDA analyte pair were 1.12±0.12 s, 1.64±0.27 s, 1.97±0.20 s and 2.56±0.67 s respectively. Their RSD values are 10.2%, 16.5%, 10.3% and 26.3% respectively (**Table 2.1**). Given the complex nature of the separation buffer, small differences in the buffer composition due to the mixing of the cell and separation buffers at the lysis intersection (the separation buffer is much lower in conductivity compared to sample buffer) may cause some migration drift due to changes in electroosmosis. Even with the change in the relative migration times however, the average peak areas did not change (**Figure 2.8 and figure 2.10**) indicating that this migration time drift did not negatively affect the potential to make quantitative measurements of intra-cellular species.

2.6.5 Cell Density Effects.

One of the limitations of using high cell densities is the overlapping of peaks from different single cell electropherograms due to the stochastic nature of the cells entering the lysis intersection. This limited the number of analyzable cells even though the device was capable of transporting even higher numbers of cells. Another 30 min experiment was performed using the same microfluidic device as was used for the 80 min run except that the cell density was decreased to $5x10^4$ cells/mL and the detection distance was decreased to 1 mm from 2 mm in order to increase the percentage of fully resolved single cell electropherograms. During this run, 258 cells were lysed and 185 fully resolved electropherograms were detected and analyzed (72%) which again is close to the 75-81% expected assuming that the single electropherograms were between 0.75 and 1.0 s long. The lower cell density helped to improve the number of analyzable cells but it reduced the average throughput of the device to 6.2 cells/min. For the 30 min run, the average relative migration time was 0.76 s. When corrected for the different separation distances 1mm in the 30 min run vs. 2 mm in the 80

min run the relative migration time would be 1.52 s which lies within the range seen from the 80 min run. The relative standard deviation (RSD %) for all runs were also similar. The average CFDA peak area (**figure 2.8**) for the 30 min run was 0.0032±0.0011 and median was 0.0031 which are statistically equivalent to that seen in the 80 min run reported above. The reproducibility of the results bodes well for the robustness of the system.

Finally, in addition to the ability to analyze cells continuously for over 80 min, the devices reported above could be used more than 12 times without degradation of the separation quality. The 2% (w/v) BSA and the non-ionic surfactant 0.2% (w/v) tween20 significantly reduced channel blockages.

2.7 Conclusions

The 3-pumping channel microchip design reported above generates pumping rates up to 9.2 nL/s. Over a 1000 cells were transported, lysed and the lysate injected and separated. Complete injections were achieved with 0.8 bar actuation pressure and 100Hz actuation frequencies in the presence of ~700V/cm separation channel field strength. The cell analysis rate averaged 14 cells/min for the 80 min run. Of the 1120 cells lysed in the 1st run, 491 lysate electropherograms (44%) were completely resolved which is within the range expected from peak overlap theory. Decreasing cell density by approximately half increased the number of resolved electropherograms to 72% but decreased the overall throughput to 6 cells/min. Channel clogging caused by adhesion of debris on the channel walls was avoided by using 2% (w/v) BSA and 0.2% (w/v) tween 20 in the separation buffer. The device design was robust as a single device could be used more than a dozen times without degradation of the separation results.

Chapter 3 - Electrochemical and LIF detection of nitric oxide, other reactive nitrogen species and reactive oxygen species using multi-layer microfluidic platforms

3.1 Introduction

3.1.1 Nitric Oxide and other Reactive Nitrogen Species

Studying the nitric oxide (NO) in biological fluids is very important since it is involved in crucial physiological functions in human and other mammalian cells. In 1987, NO was characterized as an "endothelium derived-relaxing factor".[66] It is primarily produced in endothelial cells and diffuses to nearby cells causing vasodilation. R.F Furchgott, F.Murand and L.J Ignarro were able to individually describe this process, and they won the Nobel Prize for Physiology and Medicine in 1998 for this work. With this exciting discovery, vast research areas have been opened up and more than 204,000 papers have been published with NO as a keyword in the last decade.

NO is an intercellular signaling agent. It is involved in many vital body functions including immune response,[67] neurotransmission,[68] blood pressure regulation,[69, 70] wound healing,[71] cardiovascular function[72, 73, 74] and antimicrobial activity.[75] In addition NO has been implicated in certain diseases such as cancers,[76] neurodegenerative diseases[73, 77] and diabetes.[74]

Three nitric oxide synthases (NOS) are responsible for the production of NO in the body. They are endothelial nitric oxide synthase (eNOS), inducible nitric oxide synthase (iNOS) and neuronal nitric oxide synthase (nNOS). NO is formed as a by-product when L-arginine is transformed in to L-citrulline in the presence of nitric oxide synthases. Significant amounts of NO are produced by iNOS upon cellular injury or tissue damage. Quantitatively, iNOS produces NO at millimolar

concentrations; whereas, nNOS and eNOS produce NO in the nanomolar level. NO is a radical molecule and highly reactive. Because it is small and gaseous (dissolved in aqueous medium) it also has a high diffusion coefficient. Free NO concentration in biological systems ranges from the low micromolar to nanomolar levels. NO is easily oxidized to other reactive nitrogen-derived species such as nitrogen dioxide (NO_2), peroxynitrite (ONOO-), dinitrogentrioxide (N_2O_3), dinitrogentetraoxide (N_2O_4) and nitrates (NO_3^-). In addition, it can be converted to nitrosothiols and metal-NO complexes. Peroxynitrite ($ONOO^-$) is involved in oxidation and nitration reactions in some types of cells. It is also highly reactive and degrades via two paths.[72] In the first path, Peroxynitrite forms its conjugate acid (ONOOH) and then further decomposes to highly reactive $^{\cdot}NO_2$ and $^{\cdot}OH$ radicals. This reaction pathway is more favorable in non-polar environments such as cell membranes. In the second pathway, carbon dioxide, metals and thiols present in biological fluids also react with peroxynitrite and/or its conjugate acid.

Detection of NO and other reactive nitrogen species(RNS) present in biological systems is challenging due to their low concentrations and short half-lives. Many detection techniques have been reported in the literature such as absorbance,[78] fluorescence,[79, 80, 81] chemiluminescence,[82, 83] electron paramagnetic resonance (EPR)[84, 85] and electrochemical approaches.[86, 87, 88] In order to study NO in single cells laser induced fluorescence (LIF) methods have been utilized. In these approaches, capillary electrophoresis was used to separate the reactive nitrogen species and they were detected via conjugation with fluorescent probes.[79, 81] LIF of reactive nitrogen species requires selective derivatization (ex: derivatization of NO with DAF-FM DA) in order to detect the species of interest. In contrast, electrochemical (EC) detection can be performed without derivatization. Many reviews have addressed NO sensing applications using different kinds of modified electrodes.[86,88] A wide variety of sensitive and selective electrodes have been reported

that were optimized for detection by tuning the size, shape and surface area of the electrode based of the nature of the analytes.[89, 90] Some of the sensing techniques have been associated with selective derivatization in order to enhance the sensitivity and selectivity. In addition, these electrodes were shown to be compatible with microfluidic integration techniques and can be easily confined to miniaturized detection systems.

Among the many EC detection methods, voltammetry and amperometry are higher sensitivity and specificity than other EC techniques. When ME electrophoresis is being used, voltammetry however is not applicable since fast voltage scans have to be performed to detect each analyte it as reaches the electrode via electroosmotic flow (EOF). If amperometry is used, electroactive analytes can be detected by applying constant potential to the working electrode while measuring the redox current verses the relative migration time. Therefore, amperometry is well suited for electrophoresis coupled lab-on-a chip separations.[90]

Amperometry is one of the most popular methods that can be used for highly sensitive and selective applications.[91] In the presence of sufficient electrode potential electro-active species can be selectively oxidized/reduced. This redox current is measured as the analyte signal. Most NO sensors are based on this phenomenon. A common problem, however, encountered in these types of applications is interference. Typically NO oxidizes between (0.7-1.0) V vs Ag/AgCl electrode. Other electroactive species present in biological fluids can interfere with the analyte signal. For example, uric acid, hydrogen peroxide, nitrite, carbon monoxide, dopamine, glutathione and ascorbic acid tend to produce redox currents around this potential and they may interfere with the current signature produced by the NO.[92]

3.1.2 Intracellular Superoxide

Superoxide is another biologically important molecule that plays a crucial role in intercellular signaling and pathophysiological functions.[93, 94] It directly reacts with NO in order to form a highly reactive $ONOO^-$ radical anion. In addition, it is involved in several other crucial intracellular reactions. The excessive production of this radical superoxide anion can cause cytotoxic effects. It has been associated with a variety of diseases including cancers,[95] hypertension,[96] neurodegenerative diseases (Alzheimer and Parkinson),[97] diabetes,[98] aging[99] and inflammatory disorders.[100] The superoxide anion is formed as a byproduct of oxidative phosphorylation which takes place in mitochondria. In the inner mitochondrial membrane, unconsumed oxygen generated from the oxidative phosphorylation process is reduced by the excess electrons ("leaky electrons"). The inner membrane consists of an electron transport chain, four protein complexes, cytochrome c and the mobile carrier coenzyme Q (**see fig. 3.1**). Molecular oxygen is continuously reduced by leaky electrons in the electron transport chain with superoxide being produced at protein complexes 1 and 3.[98] However, Only 1-3% O_2 is consumed to generate O_2^- anion. Since superoxide is highly reactive and it has a very short half-life, monitoring superoxide in living cells is challenging in many ways. On the one hand, superoxide readily reacts with the $NO^{\cdot}$ radical to form highly reactive peroxynitrite ($ONOO^{\cdot}$) radical. On the other hand, it is dismutated by copper/zinc superoxide dismutase (Cu/Zn SOD) and manganese superoxide dismutase (MnSOD). These dismutations lead to the formation of other reactive oxygen species including $OH^{\cdot}$ radicals, H_2O_2, O_2 and H_2O (**figure 3.1**).[98]

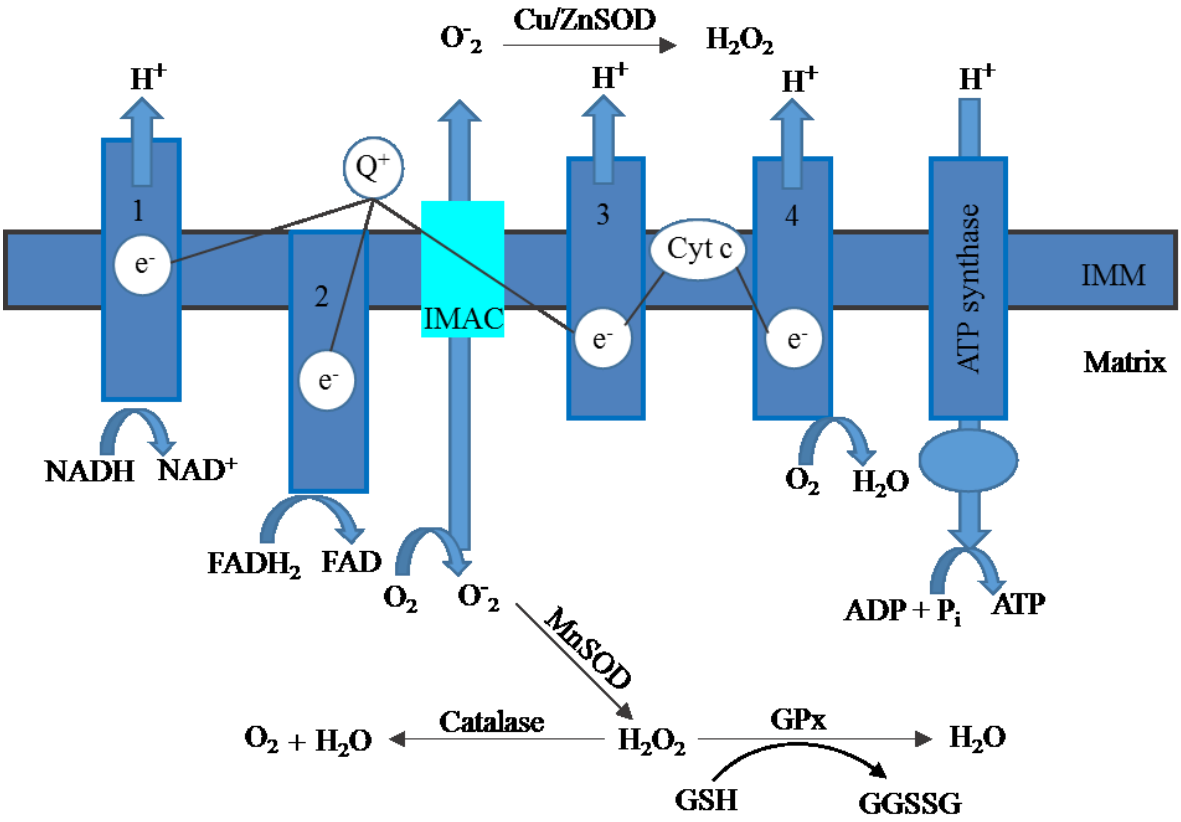

Figure 3.1: Schematic of production of superoxide radical in mitochondrial protein complexes 1,2 and 3. Superoxide is generated during oxidative phosphorylation. Oxygen is reduced by leaky electrons flow through the inner mitochondrial membrane. Superoxide dismutates to H_2O_2 in the presence of Cu/ZnSOD and MnSOD. H_2O_2 further converts to H_2O and O_2 in the presence of catalytic enzymes and glutathioneperoxydase (GPx). IMM: inner mitochondrial membrane; IMAC: inner membrane anion channel; Cyt c: cytochrome c; GGSSG: glutathione disulfide[98]

3.12.1Fluorescence probes for LIF detection of superoxide

The short half-life, higher reactivity and higher instability of superoxide make it nearly impossible detect in living single cells with EC detection techniques as with the amperometric detection of NO.[101] Amperometry is not compatible with superoxide detection since it is thermodynamically impossible to detect such extremely low superoxide concentration as they reach to the electrode. In fact, superoxide reacts readily with almost all of the reducing agents in the environment. However, recent approaches using chemiluminescence,[102] electron spin resonance[103] and fluorescence imaging techniques to monitor intracellular superoxide can be detected.[104] A novel florescence probe known as hydroethidine (HE) serves as a suitable candidate for superoxide detection. HE is a non-fluorescent probe that passively diffuses through the cell membrane. Once it is inside the cell, it is oxidized by the O_2^- anion. The oxidized product is fluorescent and known as 2-hydroxyehtidium (2-OH-E^+). However, 2-OH-E^+ is not the only product formed during the reaction. HE can also undergo oxidation in the presence of hydride acceptor and form E^+ (ethidium ion) (**figure 3.2**).

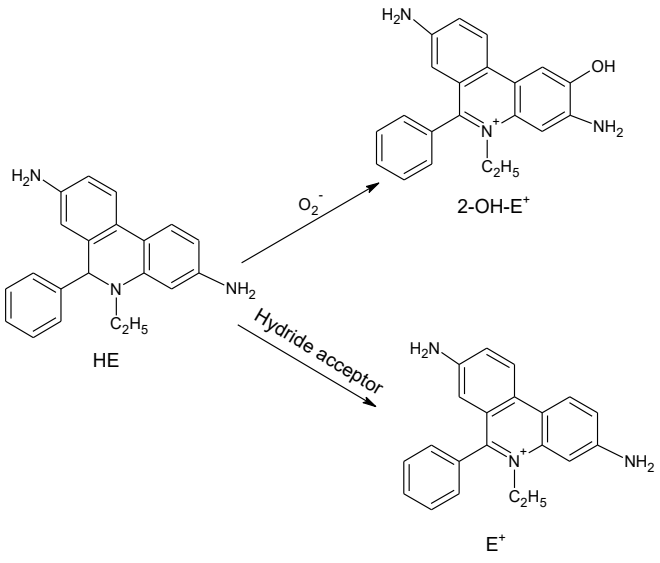

Figure 3.2: Oxidation of hydroethidine and formation of fluorescent products (2-OH-E^+ and E^+)

A previous report indicated that the formation of E^+ resembles the oxidized form of nicotinamide adenine dinucleotide (NAD^+). The mechanism of formation of E^+ is unclear and it could occur via an enzymatic or non-enzymatic path way.[101]

Derivatives of HE can be used to specifically detect mitochondrial superoxide. A novel fluorescent dye was introduced in order to target mitochondrial superoxide by replacing ethyl group with $(CH_2)_6P^+(Ph)_3$ group (**figure 3.3**). This molecule is known as mitosox-red. It specifically targets mitochondria and is oxidized by O_2^-. The fluorescent product is (2-OH-Mito-E^+) and it is similar to 2-OH-E^+.

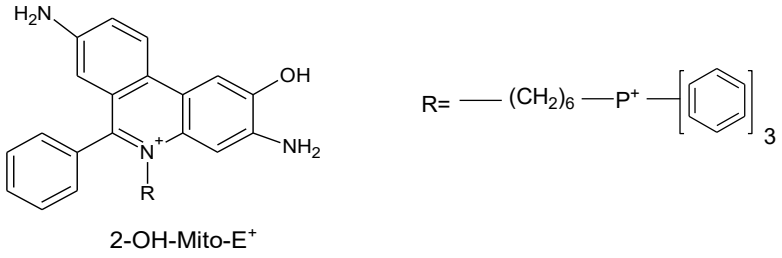

Figure 3.3: The fluorescent product form during the reaction between Mitosox-red and mitochondrial superoxide

3.2 Detection

The amperometric detection technique was used to monitor NO and other RNS. The LIF detection set-up was used to detect superoxide in T-lymphocytes.

3.2.1 Amperometric Detection

Amperometry was used to detect NO, $ONOO^-$ and NO_2^-. In this experiment, a 100µm wide 2-D Pt or Pd microelectrode (working electrode) was aligned across the separation channel such that the electrode was perpendicular with the separation channel. Three alignment strategies were tested in all the experiments. These strategies were 1. An in-channel configuration, 2. An end-channel

configuration and 3. An off-channel configuration (**figure 3.4**).[90, 105] The integration of the working electrode (WE) for in-channel and end-channel configurations was challenging since the WE has to be placed 10-20 µm upstream from the detection reservoir. In order to achieve accuracy, these alignments were performed very carefully with a microscope since small adjustments could significantly affect the detection sensitivity.[90] This problem however was not encountered using the off-channel configuration as the WE and decoupler can be placed at any arbitrary position inside the separation channel.

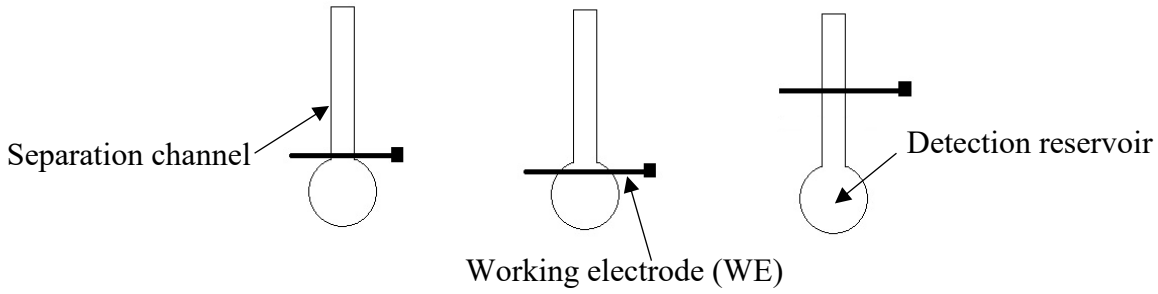

Figure 3.4: Schematic of alignment strategies of WE with separation channel (a) In-channel configuration, electrode was placed 10-20µm upstream from the end of the channel (b) End-channel configuration, electrode was placed 10-20µm downstream from the end of the channel (c) off-channel configuration, electrode was placed 1-1.5mm upstream from the end of the channel

A wireless isolated floating Potentiostat (8151BP 2-Channel wireless potentiostat, Pinnacle Technology, Lawrence, KS, USA) was used with the in-channel and end-channel configurations. A miniaturized Ag/AgCl reference electrode (RE) was placed in the detection reservoir (reservoir downstream of the separation channel). An isolated Potentiostat was connected to the WE and the

RE. An in-house written data acquisition program was used to collect the data (at the rate of 5Hz) through a wireless connection between the potentiostat and the computer.

When off-channel configuration was used, the Pd decoupler was placed 250µm upstream from the WE. Three decoupler sizes (250, 500 and 750µm) were examined depending upon the experimental conditions. The 500µm decoupler was used in most of the experiments unless otherwise specified.

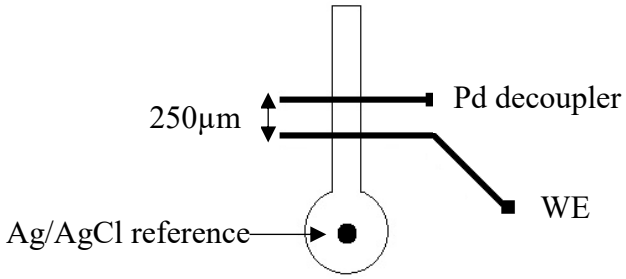

Figure 3.5: Off-channel alignment of microband WE. Spacing between Pd decoupler and WE was 250µm and microchannel was 50µm wide and 20µm deep. Ag/AgCl reference electrode was placed in the detection reservoir.

3.2.2 LIF Detection

Super oxide detection was performed using an LIF detection set up similar to that described in Chapter 2. Cells were labeled with 50µM mitosox red and the fluorescently labeled cells were driven to the cell lysing intersection using peristaltic pumps as described in Chapter 2. The fluorescently labeled, released intracellular contents were detected 2mm downstream of the injection intersection in the separation channel as a function of time.

3.3 Materials and Methods

3.3.1 Microchip Fabrication

A 2-layer microfluidic chip was constructed using multilayer softlithographic techniques as previously descibed in Chapter 2.[18]

3.3.2 Fabrication of Electrodes for Amperometric Detection

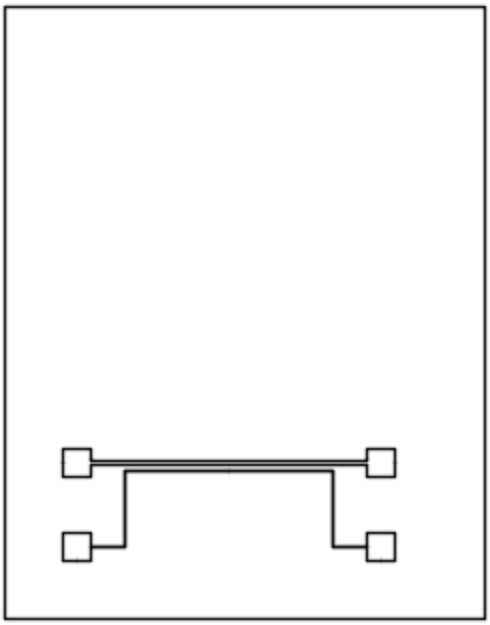

Figure 3.6: **Top view of two electrodes fabricated in a glass substrate with a thin layer deposition technique for off-channel configuration. The decoupler and WE were 500µm and 100µm wide respectively. When, in-channel or end-channel configurations were used the decoupler was disconnected and only WE was used.**

Electrode fabrication was performed using a thin layer deposition technique.[106] Glass substrates were cleaned with pirana solution (3:7 H_2O_2 and H_2SO_4) and placed in a thin layer depostion system. A Ti (adhesion layer) was deposited at rate of 2.3Å/s to a thickness of ~200Å. Similarly

Pd or Pt was deposited to a thickness ~2000Å. Then AZ -4620 photoresit was spun on the glass substrate at 1000 rpm for 30 s. The photoresist was then soft baked at 65^0C for 2 min. Then temperature was ramped to 100^0C and the plate baked another 4 min. A black mask with a transparent background was used to transfer the electrode pattern. Then the features was developed with AZ 1:4 developer followed by rinsing with deionized water. This process etched the unpolymerized photoresist while leaving the polymerized layer on top of the Pd electrodes. Excess Pd was removed with aqua regia and Ti was removed with Ti echant. Finally, the polymerized positive photoresist was removed by rinsing with acetone and deionized water.

3.3.3 Sample Preparation for NO and other RNS analysis

All the reservoirs in the completed and assembled microfluidic device were filled with running buffer which contained the non-ionic surfactant 0.20% tween 20(w/v), 20% acetonitrile(v/v), 2% bovin serum albumin(w/v), 25 mM sodium borate and 2 mM sodium dodecyl sulphate(SDS). Any air bubbles in the microfluidic manifold were sucked out with a negative pressure pump.[18] For the NO and RNS analyses, native T-lymphocyte (Jurkat) cells and LPS stimulated cells were studied for the comparison. A 1mL sample of Jurkat cells (T-lymphocytes) were spun at 1000 rpm for 3min. The supernatant was removed and 1.5µL of 25µg/mL lipopolysaccharide(LPS) in sterile PBS was introduced to make total volume 1 mL. Similarly, another 1mL sample of Jurkat cells were prepared with sterile PBS without adding LPS. These samples were held at 37^0C until the device was ready. Once the device was ready to operate, the sample reservoir was emptied and native/LPS stimulated cells were introduced into the reservoir.

3.3.4 Sample Preparation for Superoxide Analysis

The initial chip preparation and microchannel filling for the intracellular superoxide analysis was same as that for the NO analysis described above except for the dye loading, stimulation and inhibition protocols. Jurkat cells were loaded with 50μM mitosox red in a manner similar to the previously reported.[18] Briefly, native cells were spun at 1000rpm for 3min. The supernatant was then removed and 50μM mitosox red in a warm, sterile PBS solution was added and the cells were resuspended and kept in a 37^0C, 5% CO_2 environment for 20min. After incubation, the cells were washed with a warm, sterile PBS solution twice and resuspended in a PBS solution containing 2% BSA. For cell stimulation, a sterile D-Glucose solution was added to the cell culture flask such that final glucose concentration was 30μM. Cells were stimulated 24hrs prior to the experiment. SODs were inhibited by adding Diethyldithiocarbamate (DDC) into the cell culturing flask 60 min prior to the dye loading. A 10mM solution of DDC was added to the culturing flask such that final DDC concentration 1mM in the cell suspension.

3.3.5 Operation of the Device

The four pumping inlets in the top elastomeric layer were attached to solenoid valves to actuate the peristaltic pumps (**figure 3.7**). Labview 8.2 software and in-house written programs were used to control the peristaltic pumps. Through the actuation of solenoid valves (The Lee Company, Westbrook, CT) that were connected to a computer via an NI USB-6009 analog to digital converter (National Instrument).

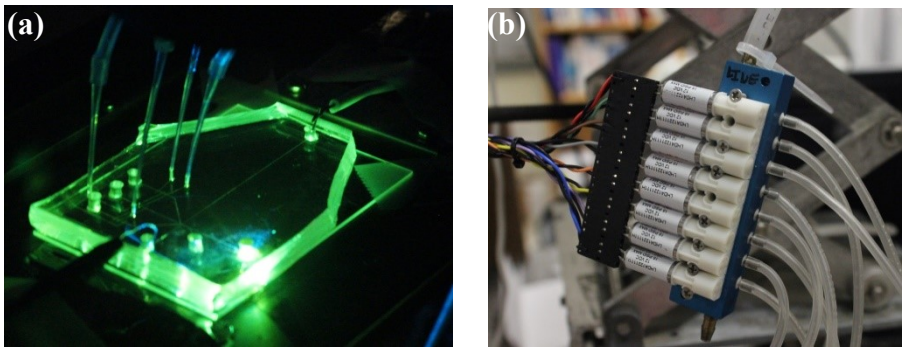

Figure 3.7: (a) Two-layer microfluidic device. Micro pumps were pneumatically controlled by pumping air through four nozzles. (b) Air pressure was regulated by solenoid valves.

An electric field strength of 700V/cm was applied in the separation channel using the Pd decoupler electrode as the ground. The voltage applied using a Bertan high voltage power supply (New York, USA) was controlled through a computer via Labview 8.2 software and in-house written programs . An Ag/AgCl reference electrode was placed in the downstream reservoir (3) at 0.7-1.0 V vs. the working electrode (Pt micro elecrtrode) to oxidize/reduce the electroactive species. The current signature vs migration time of analytes was recorded.

3.4 Results and discussion

3.4.1 Amperometric Detection of CFDA, NO and other RNS

Prior to the detection of NO, a previously reported run buffer (10mM NaCl, 10mM boric acid and 2mM Tetradecyltrymethylammonium bromide)[105] was tested with the device in order to evaluate the background noise level. Tetradecyltrymethylammonium bromide (TTAB) served as an essential component of this buffer system. TTAB is a cationic surfactant and was utilized to generate anodically driven electroosmotic flow for the electrophoretic separation in which both neutrals and the negatively charged analytes were driven to the W.E in the presence of the anodic

EOF. In addition, the basicity of the run buffer played an important role in nitric oxide detection. NO and other RNS can be stabilized in an alkaline medium since they are less likely to undergo hydrolysis at higher pH values. Therefore, the buffer pH was adjusted to 10.3 for all the experiments reported here unless otherwise specified. Two potential problems arose during the detection (regardless of the electrode configuration). The first was cell adhesion to the micro channels and the second was a high background noise. Both intact cells and cell debris adhered to the microchannel and the channels clogged within first 3 minutes of the experiment. In later experiments, however, clogging was avoided by introducing 2% BSA into the separation buffer.[18] The strong electric field (~800V/cm) used for cell lysis and electrophoretic separation was the most probable cause for the high background noise. This noise was significantly reduced by introducing an isolated floating potentiostat that did not allow the separation current to be grounded through either the working or reference electrode. However, at ~800V/cm the separation field strength was too strong to be completely grounded through the in-channel electrode thus leading to a significant current background (>400nA) on the isolated potentiostat. In addition, a highly conductive buffer will also increase the current flow, thus further increasing the background current.[106] To attempt to decrease the background, the borate concentration was decreased, non-ionic surfactants were used and buffer modifiers such as acetonitrile (ACN) were added during the sample preparation.

3.4.2 Optimization of Electrochemical Detection (EC) System

In order to optimize the system in terms of background current, CFDA labeled Jurkat cells were used. Since CFDA is electroactive, it can be simultaneously detected via LIF and the EC detection system. In order to avoid cell adhesion and to minimize the buffer conductivity 0.2% Tween 20

(w/v), 20% ACN (v/v), 2% BSA (w/v), 25mM soium borate and 2mM TTAB buffer was used. As indicated in the previous section, using ~800 V/cm field strength is a potential problem for the in-channel configuration. Therefore, ~300V/cm field strength was used to partially inject the analytes (~50% of the fluorescent dye is injected into the separation under these conditions). Both LIF and EC detectors were placed 4cm downstream of the lysis intersection. In both the LIF and EC electropherograms, peaks were observed at similar time points. The relative migration times for the LIF system were 46.7, 67.8 and 90.2s respectively. Whereas, in EC system, those peaks migrated at 64.4, 76.7 and 91.7s respectively (**see fig. 3.8**). However, there is no strong evidence to conclude that the peak produced in either electropherogram were actually due to CFDA. In addition, these results were not reproducible using the in-channel configuration. Several factors might have affected for these experiments. First, the EC system could have been detecting possible interfering substances such as ascorbic acid, glutathione and uric acid at the single cell level. Second, the microband WE might have been coated by surfactants present in the buffer as has been reported before. As such, surfactants were removed from the separation buffer before carrying out further experiments. In addition, in order to avoid cell adhesion the buffer composition was changed to (0.2% Tween 20 (w/v), 20% ACN (v/v), 2% BSA (w/v), 25mM sodium borate and 2mM TTAB and was introduced between sample reservoir and waste reservoirs (cell flowing path). All the other reservoirs were filled with 10mM NaCl, 10mM boric acid and 2mM TTAB thus minimizing the contact of the surfactants with the WE.

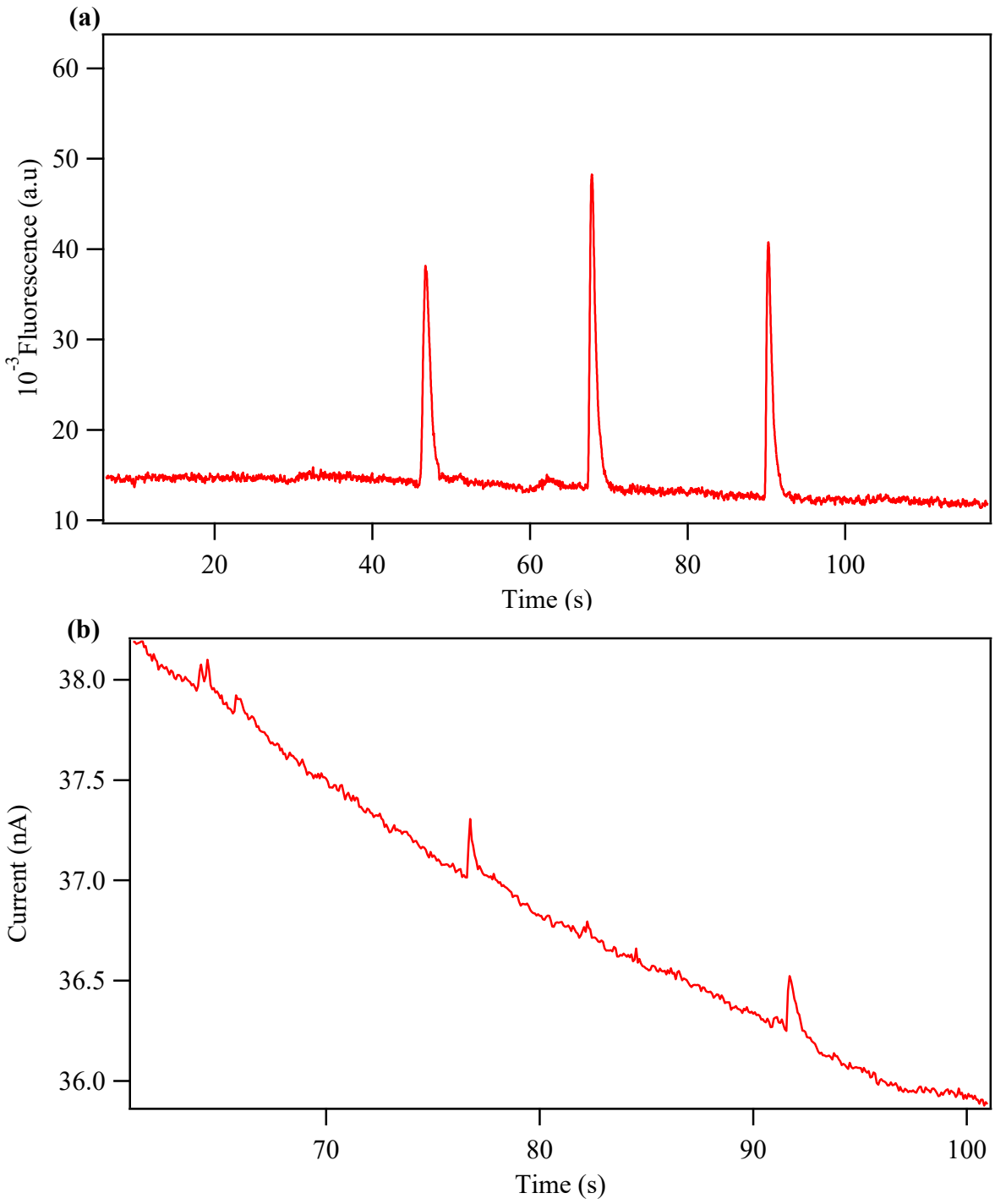

Figure 3.8: Electropherograms for LIF and amperometric detection (EC) of CFDA at 4cm downstream of the separation channel (a) LIF detection (b) Air pressure is regulated by solenoid valves.

In addition to buffer modification, an end-channel electrode configuration was introduced to minimize the background current.[90] In this configuration, the working electrode was placed 10-20 μm downstream from the channel exit It was much easier to align compared to the in-channel configuration; however it still should be performed using a microscope. Even though the background current was reduced to 250nA in the end-channel configuration compared to the in-channel configuration, the end-channel configuration still failed to provide any detectable signal associated with CFDA. Most probably, the concentration of analyte band was below the limit of detection for this configuration. In addition, broadening, loss of sensitivity and selectivity are more significant with the end-channel configuration compared to the in-channel configuration as the analyte band is rapidly diluted and broadens as it exits the separation channel.

Given the potential issues with the in- and end-channel configuration, off-channel electrode alignment was explored. This configuration made use of a Pd decoupler electrode placed in the microfluidic manifold. Recent reports have indicated that such decoupler electrodes were capable of reducing background current significantly relative to in-channel configuration and providing sensitive detection.[106] The off-channel configuration offers many advantages compared to the other two arrangements. First the electrode is directly placed in microfluidic channel (**figure 3.9**). Second, alignment does not require the microscope. Third, the analyte band confinement in the channel minimizes band-broadening. For this configuration, a Pd electrode was used as a ground electrode upstream of the working electrode to ground the separation current. The working electrode was placed about 250μm downstream of the decoupler in the separation channel (**figure 3.10**). The convective delivery of analytes was performed by electroosmotic pumping. The region between decoupler and the working electrode is field free since they are not coupled and the field from the high voltage is grounded by the Pd electrode. In this region, the flow is hydrodynamic in

nature and induced from the upstream EOF. With this configuration analytes were expected to be flow in the field free region to the WE where they are oxidized.

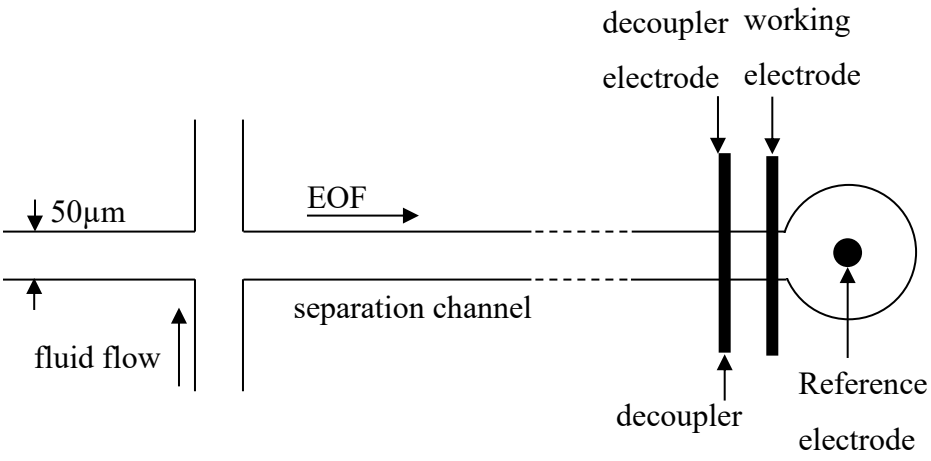

Figure 3.9: Alignment of decoupler, WE and RE with the downstream of the separation channel (not in to a scale).

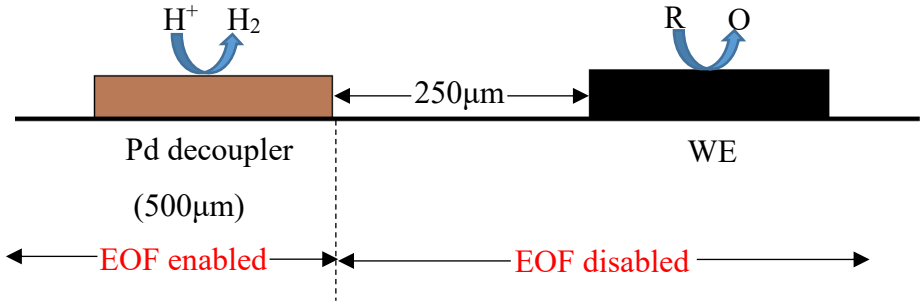

Figure 3.10: **Cross sectional view of electrodes in the separation channel. Pd decoupler and Pt working electrode shown in brown and black respectively. EOF driven flow is dominated up to the decoupler and pressure driven flow dominate between the decoupler and WE**.

An Ag/AgCl reference electrode was placed in the downstream reservoir. A constant potential of 1.1V vs. Ag/AgCl was applied to working electrode and an oxidation/ reduction current was recorded. First, the background noise level was evaluated with the off-channel configuration. The

noice level depends upon distance between decoupler and the WE.[107] For example, when distances were 100µm and 500µm, noise levels varied as 350nA and 100nA respectively. As the gap between the decoupler and the WE decreases, the noise level increases since the solution resistance between the two electrodes are low and the separation voltage has a tendency to ground through the WE as well as the decoupler. This can be reduced by increasing the distance. Unfortunately, the analyte band will broaden as the distance increases. Therefore, it is essential to optimize the distance between two electrodes. It was found that optimum distance was 250µm for the given configuration in order to achieve a relatively low background current and minimum band broadening (with this configuration, background noise was reduced to 150-200nA range which was a significant improvement compared to the other two techniques reported above). However, the strong electric field (for electrophoresis) cannot be maintained for more than 2 minutes as bubbles are generated in the separation channel (separation voltage was ~800V/cm). This bubble generation was caused by the reduction of water to hydrogen gas on the electrode surface (since the decoupler electrode serves as the cathode, hydrogen ions in the buffer are reduced). Even though Pd is a metal well known to adsorb H_2, the effective surface area of the Pd was not sufficient to adsorb all the H_2 molecules generated (Once metal surface becomes saturated with the H_2 gas, bubble formation occurs). IN order to increase the hydrogen gas absorption ability of the decoupler, the width (and thus surface area) of the Pd decoupler was increased to 750µm. The effective surface area of the 750µm wide decoupler was 750µm x 50µm since separation channel was 50µm wide. Similarly, the effective surface area of the 500µm channels was 500µm x 50µm. Thus, the 750µm wide channels offered a 1.5 fold greater surface area to adsorb H_2. By increasing the channel width, the decoupler was stable for up to 5min in the presence of same field strength. Further increases in the decoupler width might help to increase the stability, however, that leads

to the broadening of the analyte signal and poorer baseline resolution. Alternatively, decreasing the separation voltage helps to dramatically increase the decoupler stability. For example, a 500µm wide Pd decoupler was shown to be to function for up to 6hr at the 600V/cm field strength when 25mM sodium borate buffer was used.[107] Such field strengths are well suited for gated injections coupled with amperometric detection.[90, 107] Unfortunately, separation voltages <700V/cm do not support the complete lysis of Jurkat cells thus100% injections of the lysate toward the downstream of the separation channel are not achieved.[18] An alternate , therefore, a low DC voltage cell lysing technique coupled electrochemical detection was explored.[33]

3.4.3 Low Voltage Single Cell Lysis

As previously described (Chapter 1), a 200µm wide microchannel (the cell transport channel) was connected to a 50µm wide separation channel via 25µm wide orifice. Another 50µm wide side channel was used to remove the cell debris after cell lysing. CFDA labeled Jurkat cells were transported under the influence of a 75V/cm field strength. As the cells reached the lysing region they were lysed with a 600V/cm field strength and the negatively charged CF was injected into the separation channel. As a proof of principle, the separation of the NO specific fluorescent dye 4-Amino-5-methylamino-2',7'-difluorofluorescein diacetate (DAF-FM) was performed. DAF-FM is non-fluorescent and cell permeable dye. Once it passively diffuses into the cell, a fluorescent product is formed after the acetoxy groups are hydrolyzed on the dye and it reacts with intracellular NO (DAF-FM T; benzotriole derivative).[30, 92]

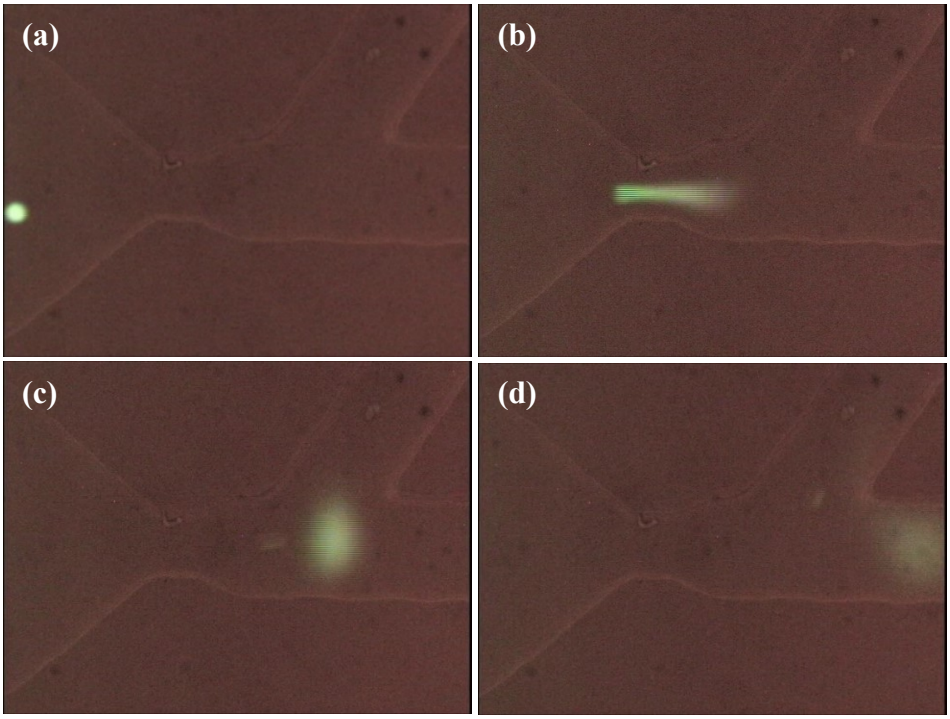

Figure 3.11: Single cell manipulation using different field strengths (a) cell transport under the influence of 75V/cm field strength in 200µm wide channel (b) cell lysing at the orifice in the presence of 600V/cm field strength (c) separation of cell debris and charge analytes (d) hydrodynamic flow carries cell debris toward the waste reservoir and charge analytes moving along with the separation channel in the presence of 150V/cm field strength.

In this case, CFDA was also loaded into the cells along with DAF-FM. The CFDA is used as an internal standard for NO quantification. An electropherogram of the separation of the cell contents is shown in **Figure 3.12**. The separation distance was 2 mm. The first peak and the partially separated second peak are from CF. The last partially separated peak is due to the DAF-NO derivative. Previous reports have indicated that P-CF and DAF-FM are difficult to resolve in short separation distances as they have similar charge/size ratios. In addition, the electric field strength

will also affect the separation resolution. Increasing the field strength is not an option for this separation since that would dramatically increase the background current.

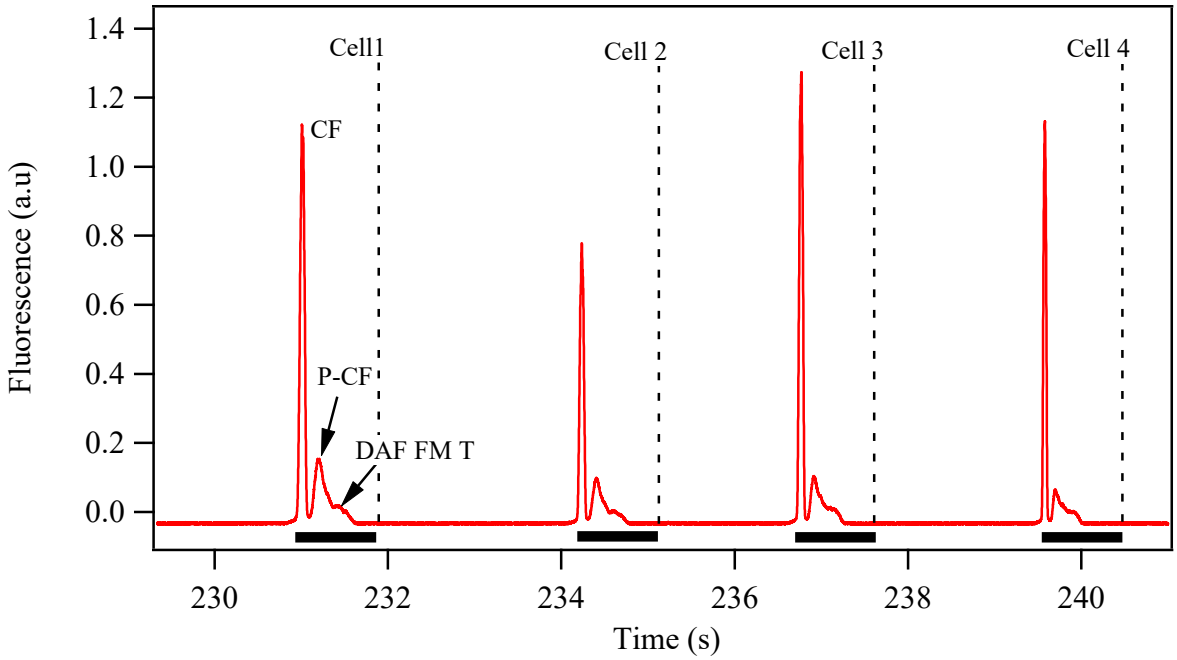

Figure 3.12: Electropherogram associated with detection of NO via LIF 2mm downstream. Each cell produces three peaks which are associated with CF, P-CF and DAF FM T. P-CF and DAF FM T peaks are partially resolved due to low field strength (~150V/cm). Peak area of DAF FM T is directly proportional to the concentration of NO in single cells.

The major potential advantage of this method in regard to the future integration of an electrochemical detector is a dramatic reduction of the background current since the field strength in the separation region (where the WE and RE were placed) was ~150V/cm. Therefore, observed average background currents for in-channel and off-channel configurations were 40nA and 10nA respectively. This new technique could, therefore, be used to detect electroactive analytes via single cell lysis which could not be previously determined due to the high background current.

There is, however, at present still significant fluctuations in the baselines of these separations which may hamper reproducibility. This can be seen in Figure 3.16 where CFDA labeled Jurkat cells were transported, lysed and electrochemically detected using this configuration. The lysates were simultaneously detected via EC and LIF techniques (**figure 3.13).** Even though both detection systems successfully detected the lysates, the signals produced from each system cannot be correlated each other. LIF signals for each single cell was reproducible and the baseline was stable. The signals produced from EC system, however, were not consistent and the baseline was unstable (significantly varying as a function of time). One potential cause of this baseline instability that is currently being investigated is the fouling of the electrode surface by the surfactants in the separation buffer which included Tween 20 and BSA to prevent cell adhesion and TTAB to enhance the electroosmotic flow for the reverse polarity mode. Tween 20 and BSA are non-ionic surfactants and may have coated the electrode surface. Thus electrode response/ performance may have been degraded. Another possible issue is with the wireless isolated Potentiostat (8151BP 2-Channel wireless Potentiostat, Pinnacle Technology, Lawrence, KS, USA). It was highly sensitive towards environmental factors. For example, base-line fluctuations were observed when the vacuum pump and solenoid valves were being turned on and off. In addition, metal electrodes such as Pt are highly sensitive and could produce relatively higher noise. An alternative electrode material, such as pyrolysed photoresist film electrode and cellulose acetate membrane electrode could potentially be used in the future. Previous reports have indicated that such electrodes provide low background current and produce better S/N ratio (improving the signal by lowering the noise allows diminish the background fluctuations).[90] In addition, it is essential to further optimize the separation buffer and investigate the effect of buffer components on the electrode performance.

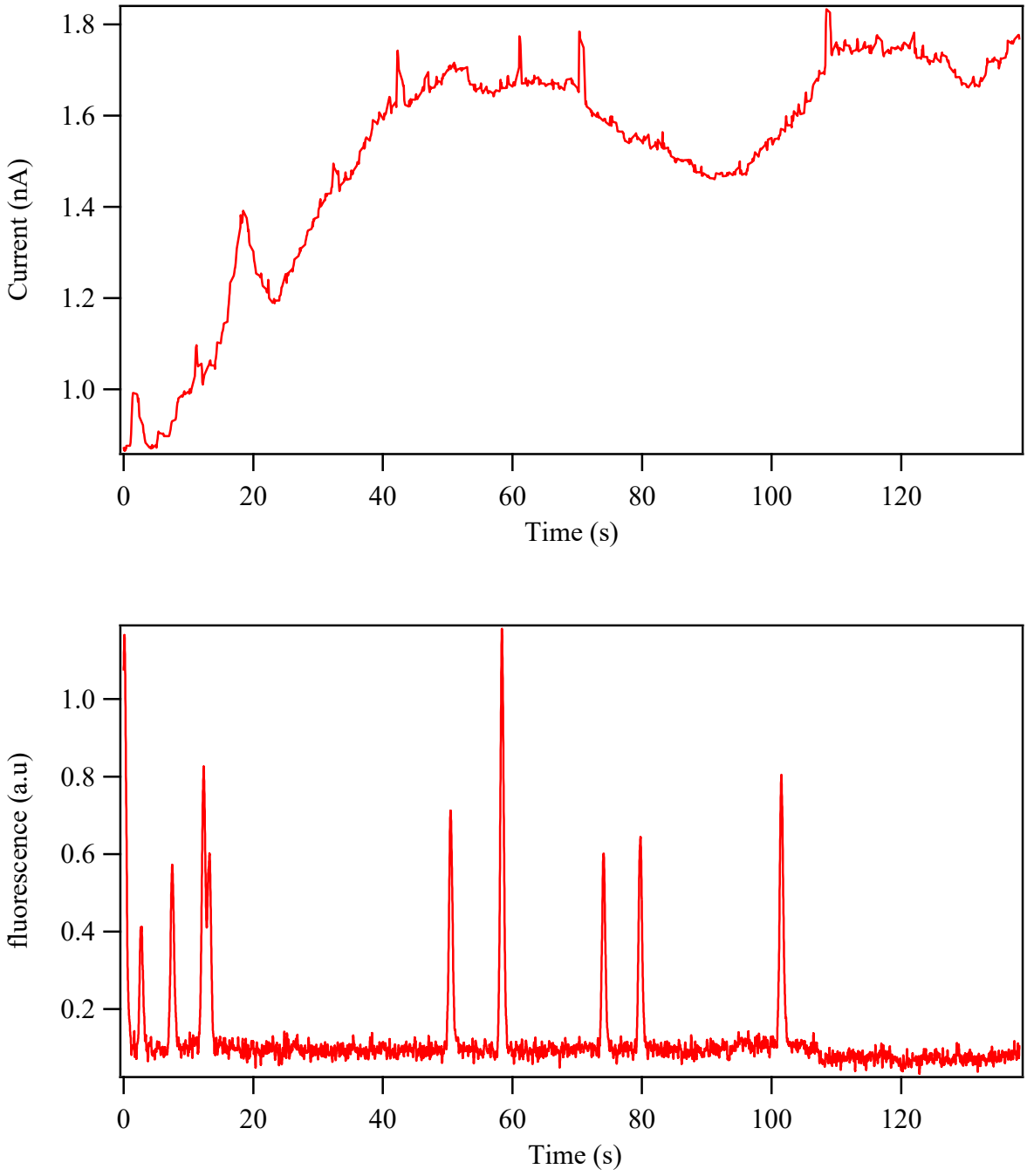

Figure 3.13: Simultaneous detection of CFDA labelled Jurkat cells via EC and LIF detection setups.

3.4.3 LIF Detection of Intracellular Superoxide

In order to quantify the superoxide, T-lymphocytes were loaded with 50μM mitosox red. Single cells were automatically lysed in a manner similar to previously reported technique in chapter 2. The oxidized product (2-OH-Mito-E^+) excites at 478nm and emits fluorescence at 590nm. Once cells were lysed, the injection plug was detected 2mm downstream of the lysis intersection in the separation channel. The S/N ratios of the lysate peaks were relatively low, and for most single cells, it was below 10 (**see fig. 3.14**). In order to perform analytical quantification S/N should be ≥ 10. However, this can be compensated for by increasing the production of superoxide via stimulation using stimulants such as phorbol-myristate (PMA), Antimycin A, Doxorubicin and D-glucose.[104] It has been shown that these stimulants are capable of increasing the concentration of superoxide human coronary artery endothelial cells (HCAEC) by 3-7 fold.[104] Jurkat cells cannot be stimulated significantly with such stimulants and that restricts the ability of using Jurkat cells (**see fig. 3.15**). On the other hand, other cell types such as raw macrophages and HCAEC cells cannot be used with automated cell lysing microfluidic platforms since these cells easily clog the microfluidic channels.

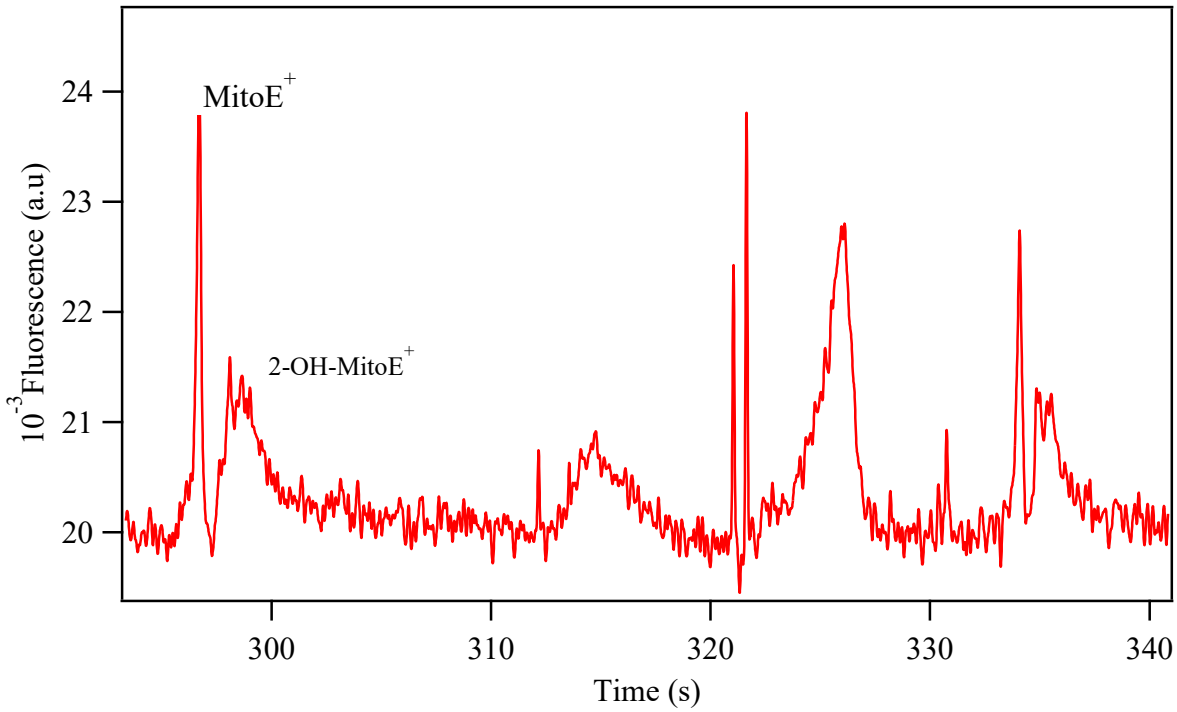

Figure 3.14: Electropherogram of superoxide detection using mitosox red in native Jurkat cells. Each cell produce two peaks associated with oxidation of mitosox red in the presence of hydride acceptor and mitochondrial superoxide.

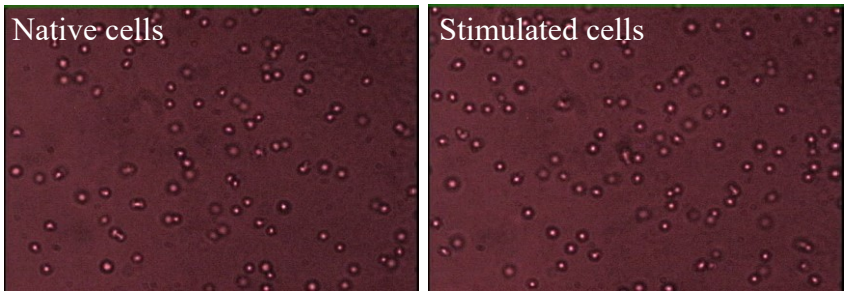

Figure 3.15: **20x micrograph of Jurkat cells loaded with mitosox red. 2-OH-Mito-E$^+$ produce fluorescence at 590mn. (a) Native cells loaded with mitosox-red dye (b) After Incubation of Jurkat cells with 30mM D-glucose for 48h and loaded with mitosox-red. There is no significant difference between native and stimulated cells. Which implies that Jurkat cells do not produce significant amount of superoxide even under the stimulated conditions.**

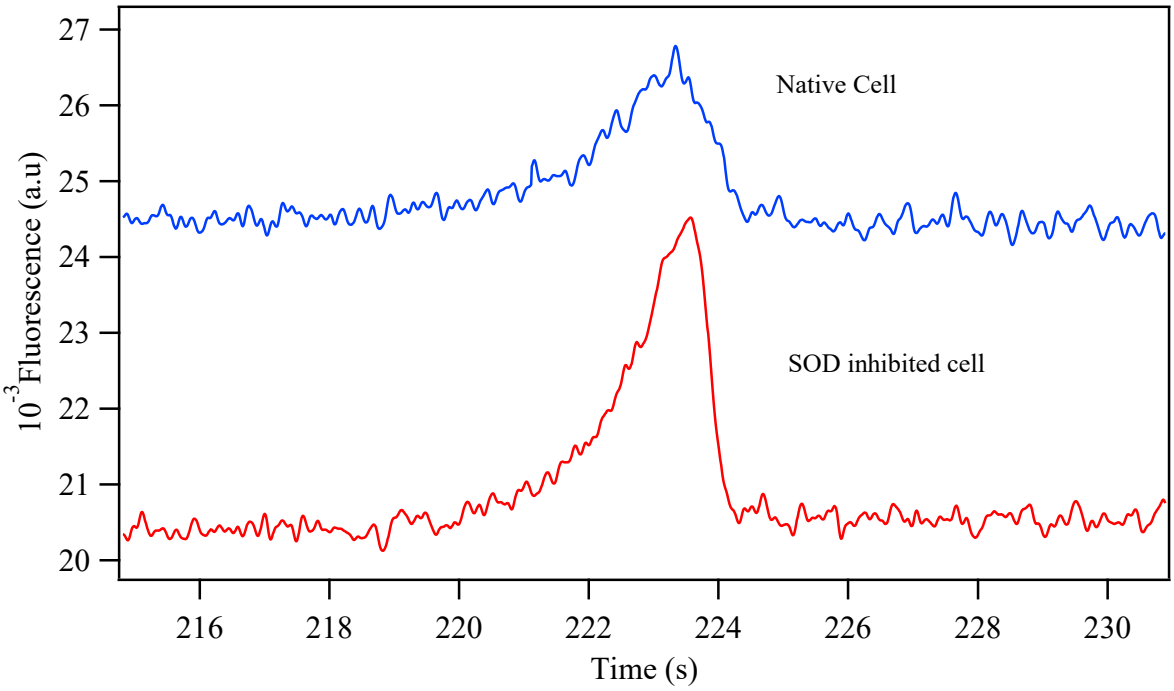

Figure 3.16: Normalized curves of native cell and SOD inhibited cell. SOD inhibition enable continuous production of superoxide and significantly increases the superoxide production relative to native cells. SOD inhibition increase the production of superoxide ~1.7 fold.

Alternatively, inhibition of SODs increases the superoxide level in many types of Eukaryotic Cells.[108] Since SODs play a major role in the detoxification of superoxide, in the absence of SODs superoxide their levels are expected to increase over the time. DDC can inhibit SOD and increase the superoxide level 1.7 fold in the stimulated cells compared to native Jurkat cells (**figure 3.16**). However, the quantification of superoxide still remains challenging since with this method the initial superoxide level of the native cells is unknown.

There may be several reasons for the very low level of superoxide observed in the Jurkat cells during this set of experiments. First, Jurkat cells are not capable of producing quantifiable amounts of superoxide relative to the other cell types such as raw macrophages and HCAEC cells.[104] Second, several reports have been indicated that 2-OH-Mito-E^+ may bind to DNA upon

oxidation.[101] This is problematic as the cell membrane and nucleus are not injected into the separation channel. Rather they are rejected into the pumping channel. This was confirmed by labeling Jurkat cells with a fluorescent probe known as SYTO 16. This dye is specifically targeted to nuclear DNA and has been used for nuclei imaging applications.[109] In this case, Jurkat cells were loaded with both SYTO 16 and 6-CFDA in order to image both the nucleus and cytoplasm (**see fig. 3.17**).

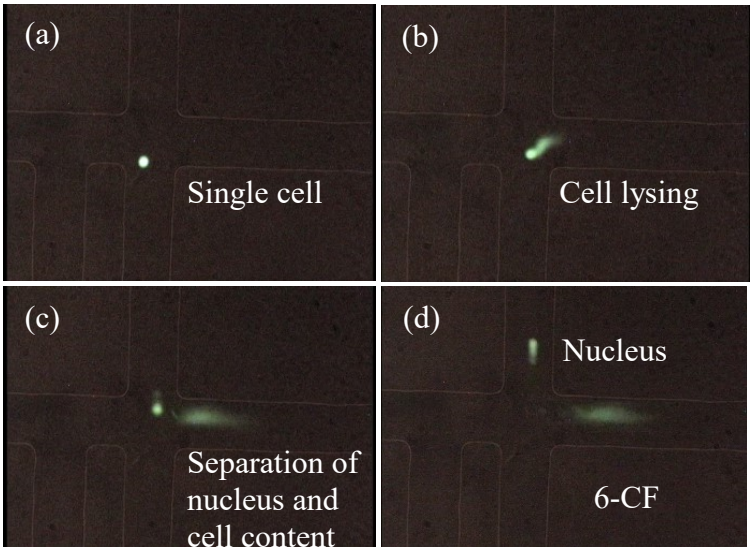

Figure 3.17: 20X magnified micrographs of SYTO 16 and 6-CFDA labelled T-lymphocytes. Cells were automatically lysed by exposing to an electric field (700V/cm). (a) single cell before lysing; (b) cell lysed in the presence of the electric field; (c) and (d) SYTO 16 labelled nucleus moving towards the waste channel along with the hydrodynamic flow and 6-CF release from the cytoplasm injected across separation channel.

Figure 3.17 shows a significant amount of the oxidized mitosox product follows the hydrodynamic flow and does not get injected into separation channel. In addition, the molar absorptivity (ε) of 2-OH-Mito-E^+ is 9400$M^{-1}cm^{-1}$ whereas, ε of fluorescence is 76900$M^{-1}cm^{-1}$. The ε of 2-OH-Mito-E^+ is ~8x smaller compared to fluorescence.[110] (Fluorescein and it's derivatives have been easily

detected with single cell lysing experiments previously).[18] Therefore, it is highly challenging to detect such fluorophores especially in single cell lysis experiments. In summary, the, detection of superoxide in single Jurkat cells, still remain challenging with ME coupled LIF detection setups.

3.5 Future Perspectives

Establishing better electrochemical isolation methods (isolation of detection system) is the key to decreasing the background current in order to detect NO and other RNS through amperometric detection. One potential alternative, is to ground the separation voltage outside of the microchannel via a cellulose acetate membrane (**see fig. 3.18**).

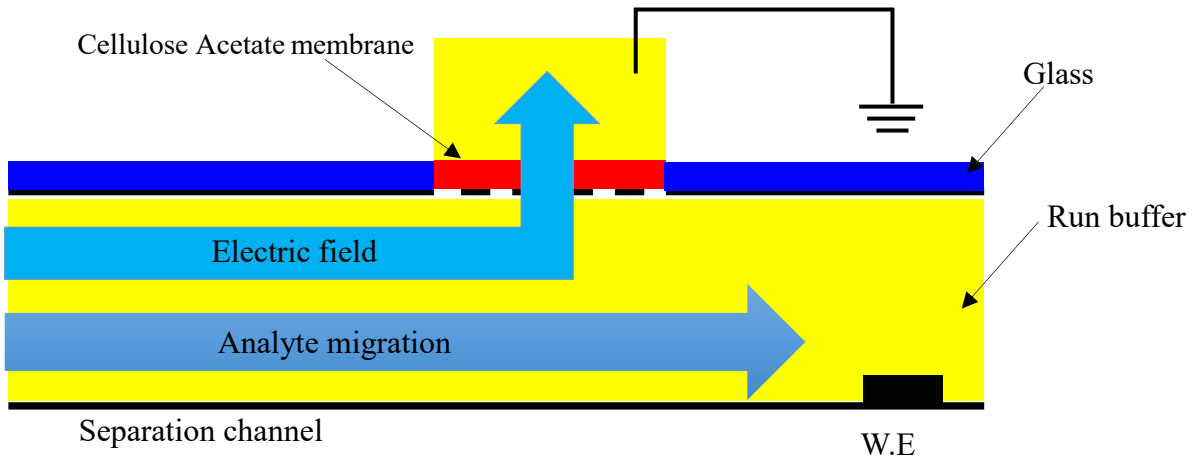

Figure 3.18: Schematic of modification of off-channel configuration to decouple separation voltage outside of the separation channel. Conductive interface (cellulose acetate membrane) between microchannel and the decoupler allows electric field to ground outside.

In other words, the separation voltage will be grounded to the outside via a decoupler electrode (as described in the off-channel configuration) as the analytes are hydrodynamically carried past the W.E due to the pressure driven flow and initial momentum gained with EOF. With this approach, the microfluidic separation channel will be sealed against a glass substrate that consists of a 20-

30μm wide hole which will be covered by a cellulose acetate membrane. Cellulose acetate is a good conductive material and previous reports have indicated that electric fields can be grounded using this method effectively.[111,112] The advantages of this technique are two-fold. First, this configuration can be used under both reverse polarity and normal polarity condition (usually, in off-channel configuration, Pd decoupler is capable of preventing H_2 formation at cathode due to adsorption. However, Pd decoupler is not useful when experiment is running in reverse polarity mode since O_2 is produced at the decoupler). Second, previously reports have demonstrated that this configuration can decouple field strengths of up to 1700 V/cm (which is ~2X greater than lysing and separation voltage in single cell analysis).[112]

In addition,[112] adapting this system to single cell analyzing platform, may dramatically decrease the noise leading to a better S/N ratio and therefore better NO and other RNS limits of detection in single cells through amperometric detection.

Also, LIF detection of superoxide in single cell level should be further investigated. A different cell line such as BV2 cells would be a better candidate for the measurement of superoxide in single cells as they produce relatively large amounts of superoxide compared to Jurkat cells. In addition, studying the variation of intracellular superoxide levels in the presence of SOD, stimulants and inhibitors might be a better way of quantifying superoxide. Finally, the ability to measure such reactive oxygen and nitrogen species could lead to a better understanding neurodegenerative diseases in molecular level.

3.6 Conclusions

Electrophoretic separations coupled with amperometric detection of NO and other RNS still remains challenging since in-channel, end-channel and off-channel configurations do not

effectively decouple the detection system from the separation voltage. The high amplitude of the background current prevents detection of electroactive species at the W.E. In the future, grounding the separation voltage outside of the microchannel via a cellulose acetate membrane might help to dramatically decrease the noise level (more effective decoupling) and improve the S/N ratio.

Also, detection of superoxide with electrochemical detection methods is difficult due to high instability, rapid diffusion and a short half-life. LIF detection may provide an alternative for the analysis of super oxide. Even though, superoxide can be qualitatively analyzed at the single cell level, the production of superoxide in T-lymphocytes is below the quantification level ($S/N \geq 10$). Therefore, it will be necessary to use a different cell line such as BV2 cells which are known to produce significantly greater amounts of superoxide compared to Jurkat cells.

Chapter 4 - Integrating Optical Fiber Bridges in Microfluidic Devices to Create Multiple Excitation/Detection Points for Single Cell Analysis

The majority of this chapter is reproduced with the permission from Damith E.W. Patabadige, Jalal Sadeghi, Madumali Kalubowilage, Stefan H. Bossmann, Anne H Culbertson, Hamid Latifi, and Christopher T Culbertson.* *Analytical Chemistry*, **2016**. *88* (20), 9920-9925.

4.1 Introduction

4.1.1 Background of Fiber Optics

Optical fibers serve as wave guides that can transmit voice, data and videos in the form of light. The durability, flexibility, low attenuation and high speed data transmission capability are the reason optical fibers serve as the backbone of today's advanced telecommunication technology. Today, over two billion kilometers of fiber optics are being used all around the world. Optical fibers are composed of a core and cladding. The fiber core serves as the light propagation medium and the cladding prevents light from escaping the core. Light propagation through an optical fiber is governed by total internal reflection. Optical fibers are manufactured such that refractive index of core (n_1) is greater than refractive index of cladding (n_2). The fiber core is typically manufactured using ultra-pure glass (SiO_2) and the cladding is made by doping SiO_2 with compounds such as GeO_2, Al_2O_3 and B_2O_3. When the incident angle (θ_i) is greater than the critical angle (θ_c), light totally reflects in the dense medium.

According to Snell's law,

$$n_1 \sin\theta_c = n_2 \sin\pi/2 \tag{4.1}$$

$$\theta_c = \sin^{-1} n_2/n_1 \tag{4.2}$$

Optical fibers can be divided in to two major categories known as stepped index and graded index fibers. Graded index optical fibers are manufactured such that the refractive index gradually changes as a function of distance (from cladding to core). Due to the gradual variation in refractive index, in graded index fibers, light rays are always traveling inside the core and signal attenuation is very low since light rays are gradually guided back into the core. In contrast, stepped index fibers have an abrupt change in refractive index between the core and cladding. These fibers experience more signal attenuation compared to graded index fibers. Stepped index fibers can be further categorized as single mode (SMF) or multimode (MMF). SMFs have a much smaller core size compared to MMFs (typically <8μm, but the diameter of the core depends on the application). In SMFs, light propagates via a single path whereas in MMFs, light propagates via multiple paths (**see figs. 4.1 and 4.2**). Therefore, multiple rays spend different time intervals to reach the destination. Such delays may not be well suited with long distance data transmission. Also in MMFs, dispersion of light rays can occur since all of the rays are not propagating at the center of the core. This phenomenon is known as "modal dispersion". SMFs do not exhibit modal dispersion since the smaller core size helps to confine the light rays into the center of the core (SMFs are being used all around the word in order to transmit data with high speed and superior quality). Even though, MMFs exhibit more signal attenuation over long distances they are much more cost effective than SMF fibers for local communication networks. However, signal attenuation can occur due to micro and macro bending over the long distances. But such signal reductions are negligible compared to Copper wires. For example, attenuation per km at 1GHz, for coaxial cable

is >50dB, whereas, SMFs and MMFs can transmit light with an attenuation of only 0.2 dB and 1dB respectively.[113] In addition, advantages of optical fibers such as higher data handling capacity, data security, electrical isolation, durability and flexibility not only make them compatible with the telecommunications industry but also potentially provides a wide variety of Lab-on-a-chip applications.

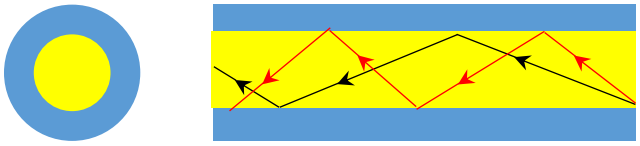

Figure 4.1: Cross section of an MMF (core and cladding are shown in yellow and blue colors respectively) and schematic of light propagation in MMF. Light rays follow different paths in fiber core

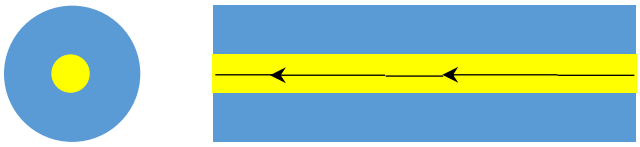

Figure 4.2: Cross section of an SMF (core and cladding are shown in yellow and blue colors respectively) and schematic of light propagation in SMF. Light rays follow only single path.

4.1.2 Modes of light propagation

Two different light propagation modes can be utilized to explore variety of LOC applications. They are known as “guiding mode” and “tunneling mode”. Guiding modes are the fundamental mode in any type of optical fiber (**see fig. 4.3**).

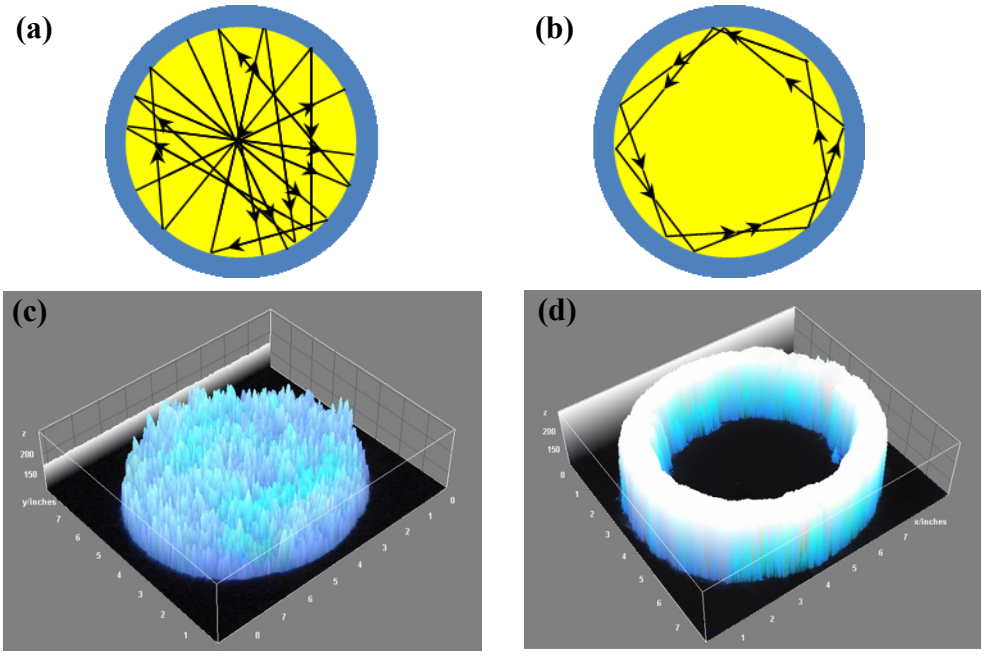

Figure 4.3: Guiding mode (a) and tunneling mode (b) light propagation. In guiding mode, most of the rays reflect across the center of the core (provides Gaussian intensity profile). In tunneling mode, light propagates along the edge of the fiber core. Light intensity at center of the fiber core is zero. (c) and (d) are 3-D profile of light intensity for guiding mode and tunneling mode respectively (constructed using ImageJ).

In guiding mode most of the light rays are confined to the center of the fiber core and the light intensity exponentially decays as a function of distance (from center of the fiber core). Therefore, the intensity of the light exiting the fiber is distributed in a Gaussian distribution. Conversely, tunneling modes are only possible with MMFs due to the relatively larger core diameter. In this mode, light waves do not propagate across the center of the fiber core, rather all of the rays propagate along circumference of the fiber core instead. This type of propagation is known as an edge confined beam (ECB). The incident light angle plays the key role in tunneling mode. This mode cannot be achieved with SMF since the relatively small diameter is not compatible with propagating light along the circumference without interfering with the center of the core. Also,

tunneling modes suffering from significant signal attenuation and light cannot be effectively transmitted more than 1 km. Even though the tunneling mode is not compatible with data transmission over long distances, it can be very useful in LOC applications as will be explained in this chapter. The integration of optical fibers with microfluidic devices can generate a significant amount of useful information about the sizes and velocities of micro/nano particles and intact cells (ex: size and velocity).

In order to produce tunneling and guiding modes, the incident light angle plays an important role as explained below.

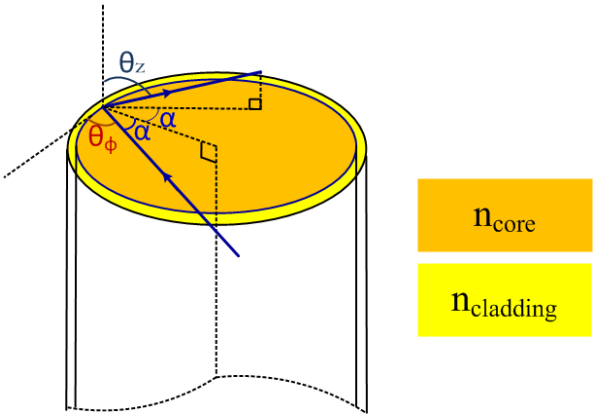

Figure 4.4: Schematic of incidence and propagation light waves throughout the optical fiber

The guiding mode/fundamental mode is produced when, longitudinal propagation angle (θ_z) of light is greater than critical angle (i.e. $0 \le \theta_z < \theta_c$). Generating tunneling modes, however, requires more stringent light entry conditions into the fiber as indicated below (the light ray must fulfill two requirements simultaneously).

α -the total angle of incidence is given by

$\alpha_c \le \alpha \le \pi/2$ where $\alpha_c = \sin^{-1}\left(n_{cladding}/n_{core}\right)$

Also $\theta_c \le \theta_z \le \pi/2$ where $\theta_c = \cos^{-1}\left(n_{cladding}/n_{core}\right)$.

4.1.3 Integrating Optical Fiber Bridges Multilayer Microfluidic Platforms

Because of the small footprint of microfluidic devices, the ability to integrate multiple optical detectors can be challenging.[114] In order to overcome this challenge the use of integrated optics have been reported[1] including on-chip waveguides fabricated by polymerization,[115,116] anisotropic silicon etching,[117,118] or ion-exchange.[119] These on-chip waveguides are, however, generally expensive, complex and time-consuming to fabricate and often highly attenuate visible light in comparison to conventional optical fibers. In addition, such integrated optical waveguides are capable of transmitting light only between pre-determined points.[120] An attractive alternative to the *in situ* fabrication of on-chip waveguides, therefore, is a system that employs optical fibers. Optical fibers have superior data transmission capability, have low light attenuation, are flexible and are cost effective.[121]

Previously, the integration of optical fibers has often been performed in the same plane as the microfluidic channel manifold and has been limited to static points along a microfluidic channel as the relative placements of the waveguides/fibers have not been tunable. Therefore, an off-chip integration approach using optical fibers potentially provides a better alternative since such fibers can be integrated at any point of interest without re-fabricating the microfluidic channel manifold. Such a fiber could be used as a bridge between two detection spots allowing the excitation and detection of fluorophores at any two given points in a microfluidic channel without significantly complicating the chip-fabrication process and the fluorescent detection system. For such a system

one end of the fiber would be placed above a detection point in a microfluidic channel specified by a focused laser from an external epi-illumination system (**Figure 4.5**).

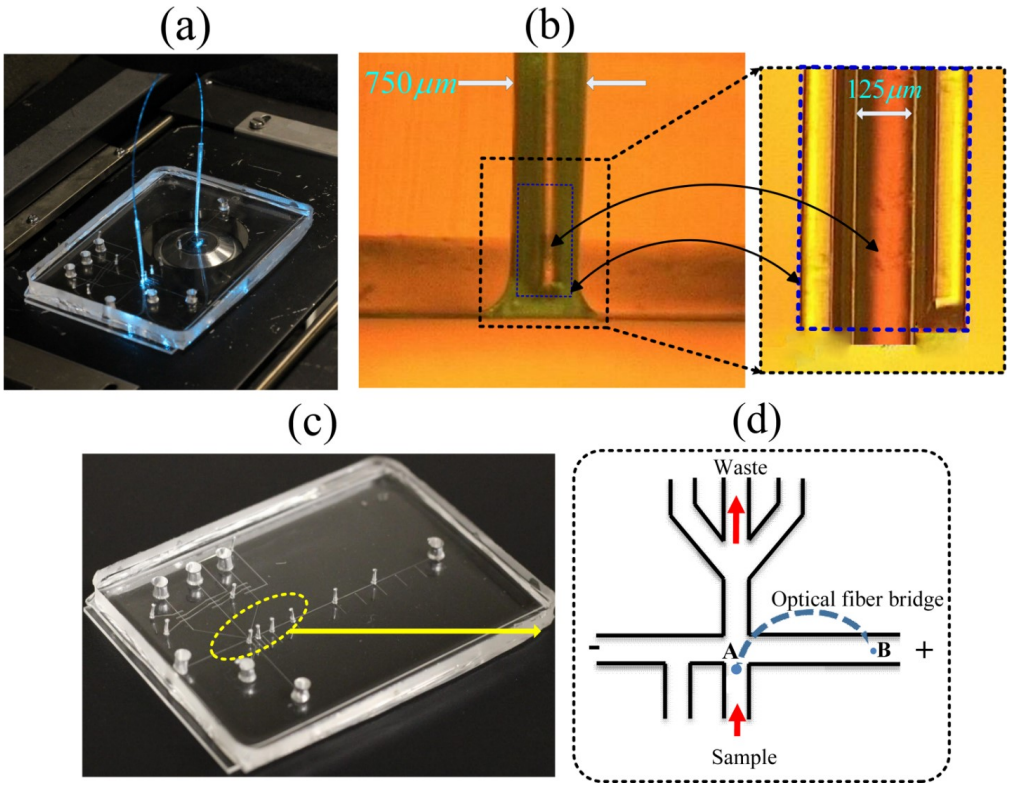

Figure 4.5: **Overview of two-layer microfluidic device integrated with an optical fiber bridge. (a) A 20X objective was placed at LDP in order to transmit excitation beam to ZDP and collect the florescence from both the ZDP and LDP. The detection time difference between the two points is equivalent to the absolute migration time of analyte of interest. (b) Cross section of ~1mm hole and a 20X micrograph of the fiber inserted through the plastic nozzle. The top layer of the device is ~5mm thick and bottom-layer is 50µm thick. The plastic nozzle restricts the free movement of the fiber. Vertical gap between the microfluidic channel and the fiber is 30µm. 360° rotation of the nozzle and vertical movement of the fiber allows precise alignment in 3D space. (c) and (d) Photograph of microfluidic device and expanded view of cell lysing intersection. A and B are ZDP and LDP (any arbitrary point of interest in downstream of separation channel), respectively.**

In addition to using the laser to excite analytes as they pass through the focused beam, this excitation light could be effectively coupled into the optical fiber and transmitted to a second excitation point. The ability of the fiber to transmit multiple wavelengths would allow the bridge then to collect the emission signal from the second detection point and transmit it back to first detection point where it would be collected by the epi-illumination system. Such a fiber bridge, therefore, would allow two excitation and detection points using only one excitation source and one detector thus considerably simplifying multiple point detection systems. In addition, the cost effectiveness of optical fibers (10cm long optical fiber costs ~ $0.30), the ease of integration compared to recently reported techniques,[122,123,124] and the compatibility with a wide range of wavelengths (250-1200 nm) would make such a system potentially interesting for a variety of microfluidic applications.

This fiber bridge could easily be used to improve single cell analysis on microfluidic platforms. Single cell manipulation in microfluidics typically consists of cell transport, cell lysis, and lysate injection followed by the electrophoretic separation of intracellular contents.[48,50,47] For detection in such systems, the excitation laser is generally focused through a microscopic objective and the fluorescent emission is collected through the same objective and sent to a detector. One major limitation of many current single cell separation systems that rely on the stochastic introduction of cells into the lysing intersection is that the actual lysing event is not detected as only one detector is employed in such systems and that detector detects the cell lysate. The reasons for this are generally 2-fold; first, there is little room to easily place 2 external excitation/detection systems at the lysis and lysate detection points as these two points are frequently only separated by a few mm. Second, there is significant extra expense in having an additional excitation source and detector. Being able to detect the lysis event, however, is important as it allows one to characterize how well

a system is behaving, to monitor whether something begins to go wrong over the course of an analysis, and to identify analytes in a multicomponent separation based upon their absolute migration times. By being able to detect both the lysis event and the separated components of the cell lysate, several important separation parameters can be determined in an absolute way that cannot currently be accomplished using a single source and detector. These separation parameters include absolute migration time, migration time drift, peak variance, analyte dispersion and the number theoretical plates generated (i.e. separation efficiency). The ability to understand such processes also allows the one to potentially improve separations. However, determining absolute migration times with microfluidic devices has rarely been reported.[46] One previous work demonstrated a fluorescence-based static imaging technique using a high resolution CCD camera.[46] The accuracy of these types of techniques depends on image quality. In addition, such approaches are restricted by the field of view of the camera to a limited distance downstream in the separation channel. If such limitations can be overcome using a fiber bridging technique then more precise and accurate separation parameter measurements could be produced in real-time.

In addition to being able to monitor the how well a separation system is working, the ability to determine absolute migration times is very useful in the identification of analytes in a multicomponent separation especially if one or more of the components are expected to be missing in any given separation. For example, if one is measuring the activity of a kinase in a cell using a peptide specific substrate which was been loaded in that cell, the level of the activity of that kinase will determine whether either the phosphorylated or non-phosphorylated version of the peptide or both will be detected in the separation. Without the injection (or 0) time marker provided by the fiber optic bridge it would be impossible to tell the difference between a cell in which all or none of the substrate was phosphorylated.

In this paper, we introduce a microchip that uses an out-of-plane optical fiber bridge to connect optically 2 points along a fluidic channel. Single cells were driven towards the cell lysing intersection using multilayer soft lithographic valves, cells were lysed at the intersection in the presence of an external electric field applied across separation channel, and the cell lysate was injected into the separation channel. The out-of-plane optical fiber bridge allowed the detection of both intact cells just prior to lysis and the downstream lysate with a single laser excitation source and fluorescent detector. As a proof of principle, the separation characteristics of 6-carboxyfluorescein diacetate (6-CFDA) released from single cells were evaluated. Furthermore, a fluorescently tagged peptide substrate that can be used to monitor the activity of protein kinase B (PKB) was introduced into single cells.[125] These cells were lysed and the activity of the kinase qualitatively determined from the ratio of the phosphorylated and non-phosphorylated peptide peaks.

4.2 Experimental

4.2.1 Reagents and Materials.

AZ-P 4620 was purchased from AZ Electronic Materials (Branchburg, NJ). AZ (1:4) developer was obtained from Fisher Scientific (Pittsburgh, PA). SU-8-2010 negative tone photoresist was purchased from MicroChem (Westborough, MA). SU-8 Developer was obtained from Acros (Morris Plains, NJ). Silicon wafers (100mm diameter) were obtained from WRS Materials (San Jose, CA). Sylgard184 Silicone Elastomer Kit was obtained from Ellsworth Adhesives (Louisburg, KS). Bovine serum albumin (BSA), Tris(2-carboxyethyl)phosphine hydrochloride (TCEP) and all solvents/reagents for synthesis of PKB peptide substrate were purchased from Sigma-Aldrich (St. Louis, MO). 6-Carboxyfluorescein diacetate (6-CFDA) was purchased from Biotium Inc.

(Hayward, CA). The building blocks for solid-supported peptide synthesis were purchased from Peptides International (Louisville, KY).

4.2.2 Fluorescent Peptide Synthesis.

The rhodamine B labeled myristoyl-based peptide substrate (R_B-GRPRAATFAEGC-s-s-CK(Mys)KKK; where the amino acids are shown with standard notations and –s-s- represents disulfide linkage) was synthesized by means of solid-supported peptide synthesis.[126] Myristic acid was bound to the short peptide sequence while the latter was still on the resin. Binding of myristic acid ($C_{14}H_{28}O_2$) to the short peptide sequence Cys-Lys-Lys-Lys-Lys-NH_2 was carried out as follows. The molar ratio of resin to myristic acid was 1:3. The Resin/ HBTU ratio used in binding process was 1:2.9 (HBTU: *N,N,N′,N′*-Tetramethyl-*O*-(1*H*-benzotriazol-1-yl)uronium hexafluorophosphate). The myristic acid-oligopeptide was then cleaved off the resin by means of trifluoroacetic acid.[126] Both the myristic acid labeled short peptide sequence (Cys-Lys-(Myr)-Lys-Lys-Lys-NH_2) and the R_B labeled oligopeptide were linked via the oxygen-mediated formation of disulfide bonds. The formation of the disulfide bond was carried by dissolving the R_B bound PKB peptide sequence (SPKB) and the myristoyl bound short peptide sequence (Myr) (1:2 molar ratio) in a minimum amount of HEPES buffer (5 mL of aqueous buffer per mg of reagents) and stirring overnight in an open vessel. The solution was frozen by immersing in liquid N_2 and then lyophilized. A red dry product was collected. The hetero-dipeptides were separated by means of descending column chromatography using Sephadex G50 as stationary phase and ethanol as eluent. MADLI-TOF MS showed the presence of a single component at the expected molecular mass (**Figure 4.6**). The electrophoretic separation and detection of the fluorescently labeled peptide showed only 1 peak prior to loading into the cell.

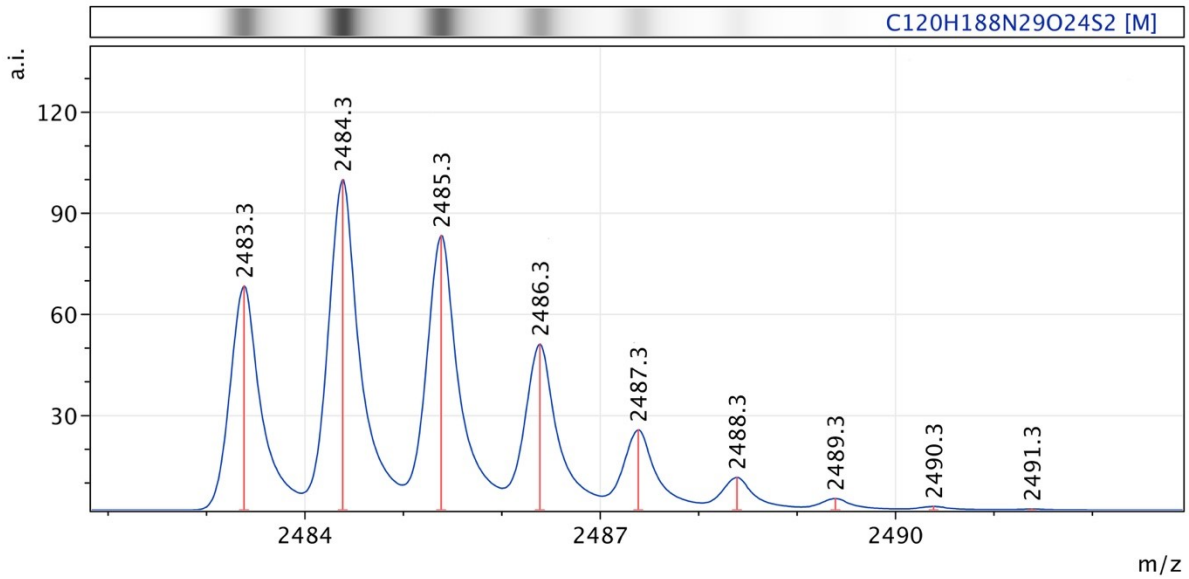

Figure 4.6: MALDI-TOF of R_B-GRPRAATFAEGC-s-s-CKKKK-myristoyl (Voyager DE STRT) The isotope distribution is consistent with the Chemical Formula $C_{120}H_{188}N_{29}O_{24}S_2$. ($R_B$: rhodamine B, G: glycine, R: arginine, P: proline, A: alanine, T: threonine, F: phenylalanine, E: glutamine, C: cysteine, K: lysine).

4.2.3 Sample Preparation

T-Lymphocytes (Jurkat cells) were obtained from ATCC (TIB-152 American Type Culture Collection, Rockville, MD) and cultured according to ATCC recommendations. Five µL of a 3.4mM 6-CFDA solution in DMSO solution were aliquoted into 50 mL polystyrene cultured flasks (Becton Dickinson Labware, NJ, USA) such that the final concentration of 6-CFDA was 0.15mM. Cells were then incubated at 37°C in a 5% CO_2 environment. After 20min, the cell suspension was centrifuged at 1000rpm for 4min, and the supernatant was removed. The cells were resuspended in a warm sterile PBS solution. Finally, after 2 washings with warm PBS solutions, the cells were resuspended in a sterile PBS solution with 2% BSA.

For the PKB single cell assay, the SPKB-Myr substrate was loaded into the cells in a manner similar to a previouly reported protocol.[127] Briefly, the substrate was dissolved in cell loading buffer (1mM $MgCl_2$, 1mM $CaCl_2$, 135mM NaCl, 5mM KCl, 10mM HEPES at pH 7.4)[127] at a concentration of 0.1mM. Cells were then incubated at 37°C in a 5% CO_2 environment. After 30min, the cells were treated with 2mM Tris(2-carboxyethyl)phosphine hydrochloride (TCEP) dissolved in cell loading buffer in order to remove any adsorbed peptide substrate from the outer cell membrane.[127] Finally the cells were washed 3X with cell loading buffer and resuspended in sterile PBS solution with 2% BSA.

4.2.4 Microchip Operation

All the microfluidic reservoirs except sample reservoir were filled with 0.2% Tween 20 (w/v), 2% BSA (w/v), 20% acetonitrile (v/v), 30mM sodium borate and 2mM sodium dodecyl sulfate (SDS). The sample reservoir was filled with CFDA or PKB labeled Jurkat cells in the cell buffer described above. Hydrodynamic flow generated by the peristaltic pumps drove fluid continuously from the sample reservoir to the waste reservoirs. An electric field of (~750 V/cm) was applied across the separation channel in order to lyse the cells as they reached the lysing intersection. After each cell was lysed, the lysates were injected into the separation channel and the components electrophoretically separated. The separation buffer quenched the electroosmotic flow and the peptides migrated toward the anode.

4.3 Detection

The 488nm line from a multiline argon-ion laser (MellesGriot Laser Group, Carlsbad, CA) was used as the excitation source and directed into the rear port of a commercial inverted Nikon TS-

100 microscope (Nikon Instruments, Inc., Melville, NY). The beam passed through a XF101-2 filter cube (Omega Optical) and was focused into the separation channel using a 20x objective (Plan Fluor, Nikon). A few centimeters of multimode silica optical fiber (Thorlabs FG105UCA, 105/125-μm multimode, N.A. = 0.22), which had been stripped of its protective polymeric coating, was bridged between the detection point and the injection intersection. As shown in **Figures 4.5a and 4.5b**, a plastic nozzle (i.e. pipette tip) segment (1cm long) was used to hold the ends of the optical fiber in place on the microchip. Over the 1cm length of the pipette the cone diameter tapered from 1mm down to 300μm. Both ends of the fiber were cleaned, cleaved, and inserted into the pipette tips which were inserted into the holes on the microchip perpendicular to the channel. This method has the advantage that while fiber is fixed in the nozzle, the X, Y and Z position of the fiber's cross section relative to the channels could be precisely adjusted and observed by moving the nozzle. The vertical gap between the end of the fiber and separation channel was 30μm. The focused excitation beam from the 20x microscope objective could be easily coupled into the bridged fiber at the lysate detection point (LDP, **Figure 4.5a**). The fiber then transmitted the excitation light to the lysis intersection (ZDP) where intact fluorescently labeled cells could be excited. The same fiber used for excitation was then used to collect the fluorescent emission from the intact, excited cells. After the cells were lysed, the lysate was injected and electrophoretically transported down the separation channel toward the anode. The focused beam from the microscope objective was used to excite the cell lysate and collect the fluorescent emission at the LDP. The fluorescence from both the intact cell and lysate was collected by the 20X microscope objective, passed through the XF101-2 filter cube, a 488.0nm holographic notch filter (Kaiser Optical) and a 800μm diameter pinhole before being detected by an R-928 photomultiplier tube (Hamamatsu Instruments, Bridgewater, NJ, USA) attached to the trinolucular port of the microscope. The

current from the PMT was amplified using a preamplifier at 50μA/V with 100Hz low-pass filter (Stanford Research Systems, Sunnyvale, CA) and sampled at 500Hz using a PC1-6036E I/O card (National Instruments, Austin, TX). With this configuration both the intact cell and lysate were excited with one laser source and detected using one PMT.

4.4 Results and Discussion

4.4.1 Transmission and Coupling Efficiency of the Bridged Fiber Configuration

The transmission and coupling efficiencies of the optical setup were calculated theoretically and determined experimentally in order to optimize the sensitivity of the bridged fiber configuration. The power transmittance (T) at normal incidence is defined as the ratio of the power of the transmitted wave to that of the incident wave. For light traveling through an array of dielectric layers, the power transmittance depends on the operating wavelength and the propagation length and decreases exponentially with length (**eq 1**). For a propagation distance of L (km), the associated power transmission ratio can be obtained by

$$\frac{P_L}{P_0} = e^{-0.23\alpha L} \tag{4.3}$$

where α is the overall loss (dB) which is the sum of the constituent losses. For our 12 cm long multimode fiber (MMF) where α =10 dB/km the attenuation is negligible and the theoretical power transmission ratio obtained is 0.998, so that ~99.8% of the incident light power is transmitted. We also assumed that the attenuation of the MMF modes due to the bending of the optical fiber were negligible. In addition, for an arbitrary polarization, the power transmittance at a planar boundary between two dielectric media (n_i and n_j) yields the following, known as the Fresnel equation.[128]

$$T_{n_i n_j} = \frac{4 n_i n_j}{(n_i + n_j)^2} \tag{4.4}$$

The power transmittance for N different layers can be obtained from eq 3:

$$T_{Total} = T_{n_1 n_2} T_{n_2 n_3} ... T_{n_{N-1} n_N} \tag{4.5}$$

In this setup the excitation light is transmitted through a glass plate (SiO_2 layer), a layer of PDMS, a buffer filled channel, and 12 cm of the bridged MMF, with refractive indexes of n_{Air}=1, n_{SiO2}=1.46, n_{Buffer}=1.33, n_{PDMS}=1.41, and $n_{SiO2\ (fiber)}$=1.46, respectively. Based on eqs 2 and 3, for the four dielectric layers theoretically the overall optical transmittance was calculated to be 0.94, so that about 94% of the incident light power should be transmitted.

In addition to the transmission efficiency, the excitation intensity and the coupling efficiency of the emitted light into the fiber at the ZDP must be taken into account. According to the optical dispersion principle, [129,130] the 50μm and 105μm multimode fibers used in the experiments reported below produced expanded light spots with diameters (w_{MMF}) of 63.8 μm and 118.8 μm, respectively, at the mid-plane of the fluidic channel (L), which was ~45 μm from the ends of the fiber. Based on the modal field distribution, the ratio of the effective excitation intensity between two MMFs can be derived as,

$$\frac{I_{eff\,(\mathrm{MMF_{105}})}}{I_{eff\,(\mathrm{MMF_{50}})}} = \left[\frac{w_{(\mathrm{MMF_{105}})} + 2L(\mathrm{NA})\,\mathrm{n}^{-1}}{w_{(\mathrm{MMF_{50}})} + 2L(\mathrm{NA})\,\mathrm{n}^{-1}} \right] \tag{4.6}$$

where the NA of the optical fibers was 0.22, and the value of the refractive index (n) of the PDMS was about 1.43. Using this equation the effective excitation intensity ratio (MMF_{105}/MMF_{50}) was determined to be 0.58. In the near field, the maximum coupling efficiency of the emitted light at the ZDP into the MMF is obtained when the distance from the launch point to the fiber is equal to fiber radius.[4] Assuming the launch point was along the mid-plane of the channel which was ~45μm

from the fiber end, the effective emission collection area of MMF_{105} is 4.4 times of MMF_{50}. Given the calculated effective excitation intensity and emitted light intensity ratios determined above, the MMF_{105} should be more appropriate for the fiber bridge configuration in terms of signal generated from the second distant detection spot.

To confirm this experimentally, the overall coupling efficiencies of the bridged fiber configurations (i.e. I_2/I_1%, where, I_1 and I_2 were peak intensities for a fluorescently labeled particle as it passed the fiber excitation cone and objective excitation cone, respectively) for the 50µm and 105µm fibers were determined to be 7.9 ± 2.5% and 45.4 ± 4.9% respectively. As transmission efficiency was calculated to be 94%, it can be seen that most of the light loss in the fiber bridge system is due to a less than unity coupling efficiency. Although the coupling efficiency is not 100%, it is constant for any given device. This, therefore, allows the use of relative intensity changes between the two detection spots to monitor properties like injection efficiencies or the progress of chemical reactions.

Finally, in addition to the significantly higher coupling efficiency of the 105µm core diameter fiber, the alignment of 50µm fiber was much trickier than the 105µm since microfluidic channel width was same as the diameter of the fiber, the 105µm fiber was, therefore, used for all of the single cell detection experiments reported below unless otherwise specified.

4.4.2 Single Cell Analysis

For the results reported below, a 12 cm long 105/125µm fiber was integrated between the zero detection point (i.e. cell lysis intersection, ZDP) and a point either 2mm, 5mm, 10mm or 15mm downstream of the separation channel. Cells were transported to the lysis intersection at an average linear flow rate of 550±23 µm/s. At this flow rate ~100% of the lysate was injected into the

separation channel while the cell debris were effectively removed from lysis intersection by hydrodynamic flow towards the waste reservoirs. As each cell passed the ZDP, a narrow peak was produced which represented the separation start time (t = 0). A second broadened peak was then detected a few seconds later which corresponded to the injection plug (**Figure 4.7**). The 2 peaks from each cell could easily be differentiated and correlated (**Figure 4.8**). From these two peaks the absolute migration time at a variety of separation distances was determined (**Figure 4.8 b, Table 4.1 and Figure 4.9**).

Table 4.1: Variation of absolute migration time, RSD% of absolute migration time, drift in absolute migration time and injection plug velocities at 2mm, 5mm, 10mm and 15mm detection distances.

Distance (mm)	Avg. abs. mig. time (s)	RSD% of abs. mig. time	Drift of abs.mig. time (%)	Injection plug velocity (m/s)	# of cells
2	0.99± 0.08	8.4	4.8	2.04±0.18	83
5	2.40± 0.10	4.1	6.0	2.08±0.085	111
10	5.14± 0.06	1.2	1.3	1.94±0.022	74
15	7.25± 0.08	1.1	0.3	2.07±0.023	75

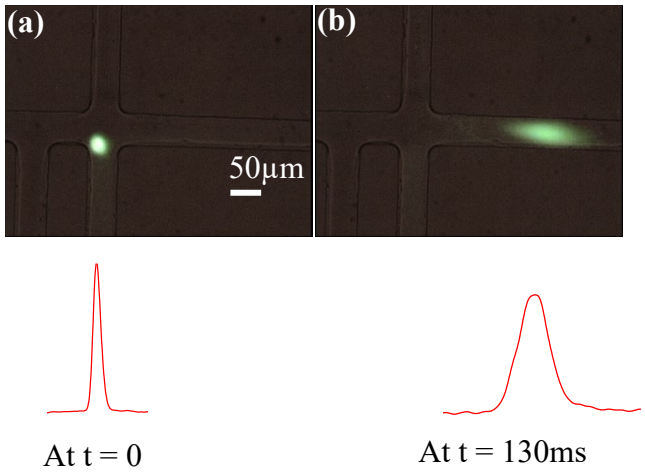

Figure 4.7: 20X magnified images of intact cell prior to lysis and the cell lysate. At t = 0, cell is at ZDP and produces tall narrow peak. After 130ms a broader peak (4σ = ~160µm) is produced by the lysate moving along the separation channel under the influence of a 750 V/cm electric field.

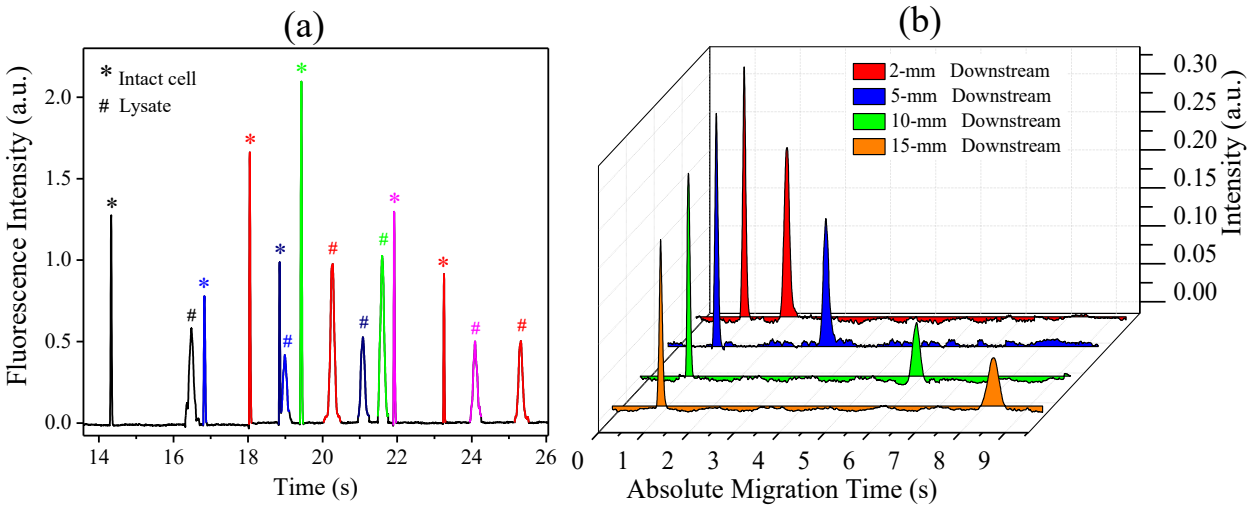

Figure 4.8: (a) Electropherogram of single cells using the optical fiber bridge. The detection point is 5 mm downstream of the lysis intersection. Each cell produces two peaks. The first narrow peak corresponds to ZDP. The second broader peak that appears ~ 2s after the first peak is obtained at the LDP. (b) Single cell electropherograms obtained with the optical fiber bridge as a function of separation distance.

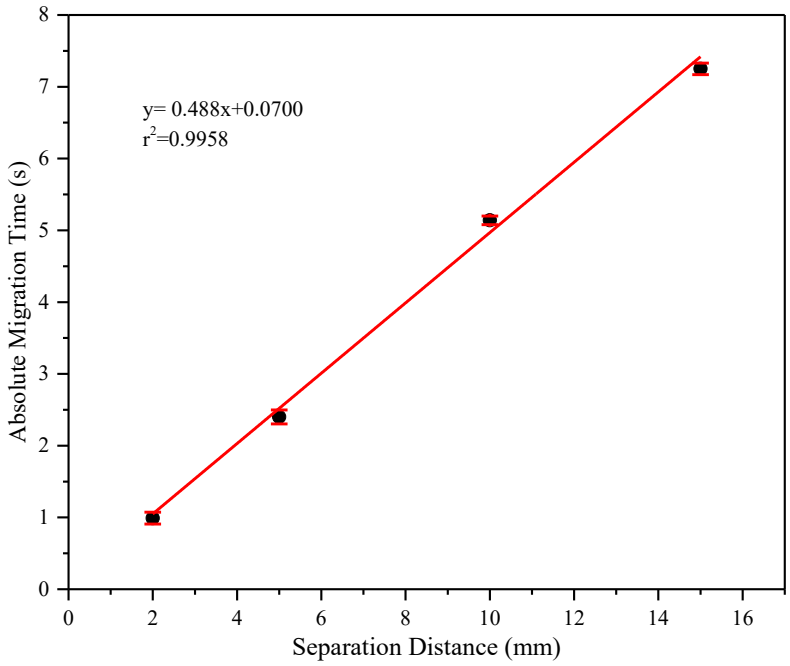

Figure 4.9: Absolute migration time as a function of separation distance

The migration time distributions at each separation distance were nearly Gaussian as the mean, median and mode values at each detection distance were the same within experimental error (**Table 4.2**).

Table 4.2: Mean, mode and median of absolute migration times

Separation distance (mm)	Mean abs. mig. Time (s)	Median abs. mig. Time (s)	Mode abs. mig. Time (s)	# of Cells
2	0.99 ± 0.08	1.00	1.07	83
5	2.40 ± 0.10	2.39	2.30	111
10	5.14 ± 0.06	5.13	5.10	74
15	7.25 ± 0.08	7.26	7.26	75

The absolute precision values for all of the migration distances were small and similar indicating good robustness for the technique. The small analyte migration time variation at each distance

was probably due to the lateral location of the cell in the lysis intersection when lysed and small fluctuations in the hydrodynamic flow. These absolute values also agree with the previous work performed in our lab using relative migration times instead of absolute migration times.[46] The %RSD decreased significantly as separation distance increased as seen in **Table 4.1 and Figures 4.9 and 4.10**. Similar trends were observed for migration time drift (**Table 4.1**).

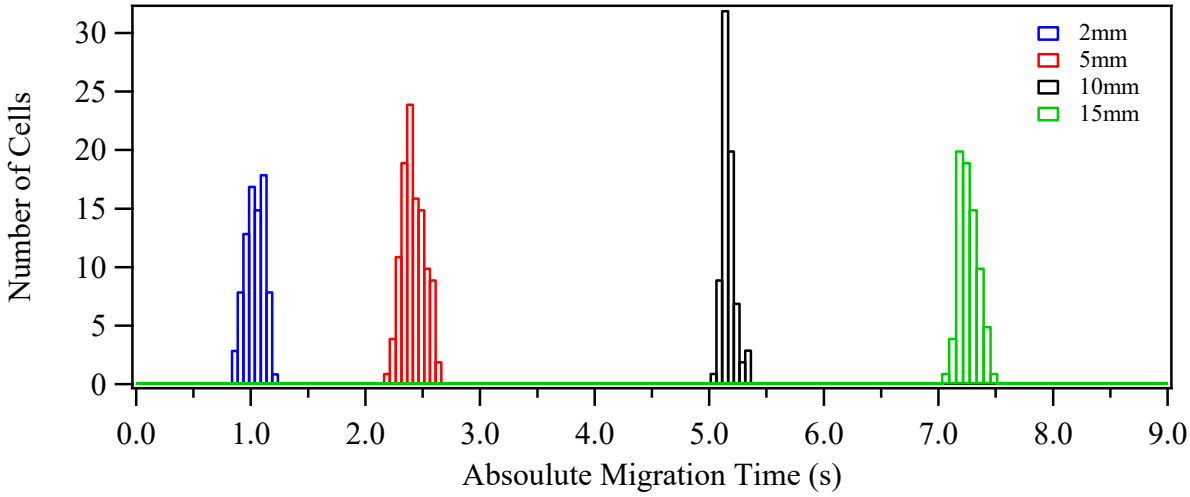

Figure 4.10: **Histograms of absolute migration times at various detection distances from the injection (lysis) point.**

It should be noted that the time required for actual cell lysis could potentially affect the accuracy of absolute measurement especially if the lysis time (l_t) is of the same magnitude as the separation time (t_m). Previous reports have shown that this type of cell was lysed <33ms (i.e. 1 frame of a NTSC video rate camera) after reaching the lysing intersection where the cells are exposed to a high electric field strength.[18,30] Experiments performed in this study using sequential video frame grabs confirmed these reports. Given that the shortest migration times reported were on the order of 1sec (Table 1) the lysis time uncertainty ~0.03s contributed < 3% to errors in accuracy and precision at the 2mm detection distance but < 0.4% at the 15mm detection distance.

The separation velocities at all separation distances were essentially constant as would be expected (**Figure 4.11**). The average velocity of the injection plug was 2.03 ±0.06 mm/s over all distances.

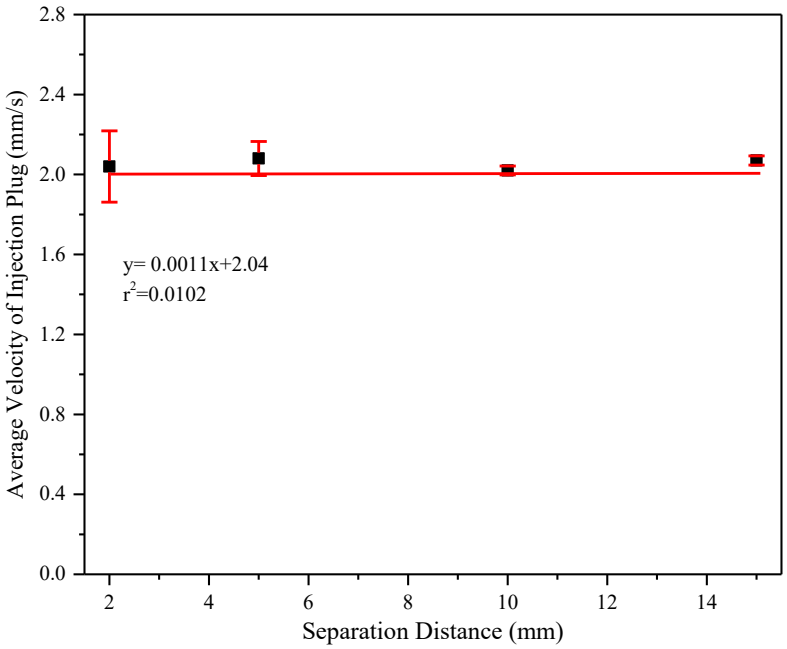

Figure 4.11: Average velocity of the injection plug vs. separation distance. Velocity remains nearly constant and independent from separation distance (r^2 =0.0101).

For all runs the prelysis/separation peak area ratios were nearly constant indicating that the injection efficiency was constant over the course of any particular run. The ratio was not 1:1 due to excitation and emission-coupling inefficiencies with the fiber and migration velocity differences between the intact cell and the lysate as discussed above.

Under ideal circumstances lysate peaks will be broadened as a function of separation distance solely due to longitudinal (molecular or Fickian) diffusion. Longitudinal diffusion can be determined using the Einstein-Smoluchowski equation ($\sigma^2 = 2Dt$) where σ^2 is the spatial peak variance, D is the diffusion coefficient, and t is the migration time. The diffusion coefficient (D) is ½ the slope of the plot of spatial peak variance vs migration time. The y-intercept is the variance

due to the injection plug length and detection window length.[131, 5] The slope of a plot of the spatial peak variance (σ^2) versus migration time (t) (**Figure 4.12**) for the data reported above yielded an experimentally derived diffusion coefficient for CFDA of 4.93×10^{-5} cm^2s^{-1} at 25°C which is 11x greater than the static value for fluorescein previously reported (4.25×10^{-6} cm^2s^{-1} at 23°C).[131]

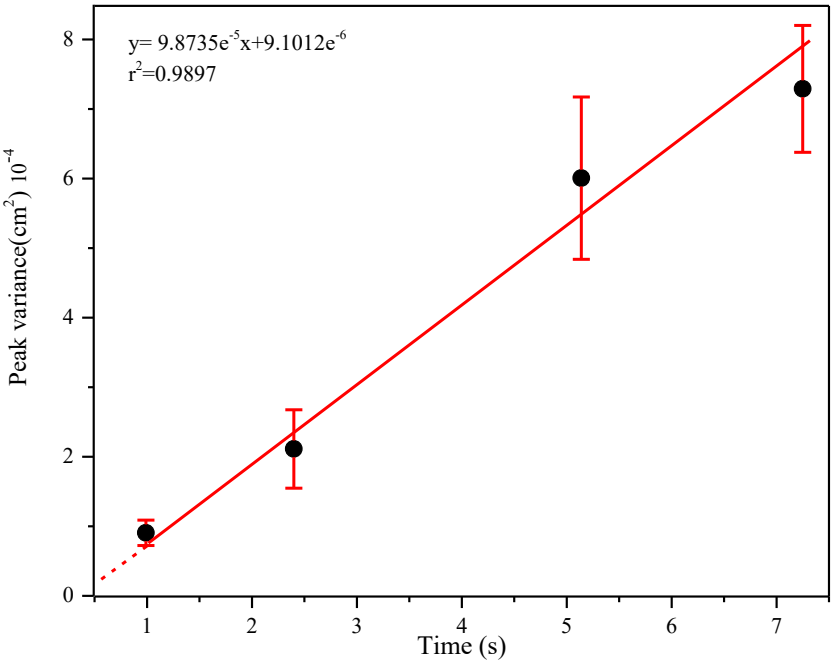

Figure 4.12: Spatial peak variance vs. separation distance

The excess dispersion, i.e. band broadening in excess of molecular diffusion, is likely due to Joule heating, the cell-separation buffer conductivity mismatch and/or hydrodynamic flow generated by the on-chip, in-channel pumps. The injection plug length (l) was determined from the y-intercept ($l_{inj}^2/12$) of the graph minus the detection window length ($l_{det}^2/12$).[5] The detection window length was determined by the (pinhole aperture)/(objective magnification) which was equal to 40µm. The calculated average l_{inj} value (at t = 0) over all four runs was 65µm and consistent with that seen experimentally (In Figure 2, the lysate band width at 4σ after 130ms is ~160µm). Finally, the ability to calculate the absolute migration time and to measure peak width also allows the

calculation of the separation efficiency (Number of theoretical plates generated; N). A plot of N vs. the separation distance (**Figure 4.13**) yielded a straight line as expected ($R^2 = 0.96$, see SI) with an average plate height (H) of 4.3µm for the single cell separations.

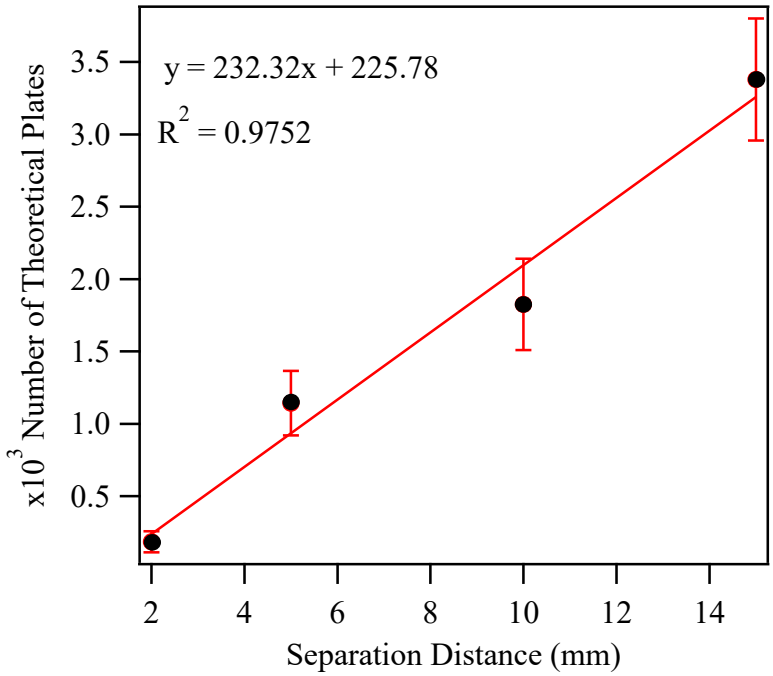

Figure 4.13: Number of theoretical plates vs. separation distance

4.4.2.1 Analysis of Intracellular PKB

PKB is one of the most important protein kinases and plays key roles in many vital cellular functions (ex: glucose metabolism[132], insulin production [133] and apoptosis[134]) Biomedical and pharmaceutical industries have broad interests in better understanding kinase pathways as misregulation of these pathways leads to a variety of diseases.[135,136] Previous papers have shown that kinase activity in single cells can be monitored through the addition of a peptide substrate that contains the amino acid sequence specific for that kinase.[125,137,138] Chemical moieties that can be

attached to the peptide have also been identified in order to passively transport the peptide across a cell membrane.[139,140] In the experiment reported below, a myristoyl group was attached to a fluorescently labeled decapeptide specific for PKB. In addition, a cysteine linkage between the substrate peptide and the peptide containing the myristoyl group was included, such that the substrate peptide would be released from the acid once in the reducing environment of the cell. If PKB is active it will phosphorylate the threonine in the peptide. The activity of PKB can then be monitored by examining the ratio of the phosphorylated and non-phosphorylated peptides electrophoretically separated in the cell lysate as reported previously.[138] For inactive or highly active kinases only the non-phosphorylated or phosphorylated peptides, respectively, may be present. Under such conditions, the ability to measure absolute migration times of the analyte(s) is critical to identify what specie(s) are in the cell. The implementation of an optical fiber bridge in the microfluidic device allows the measurement of the absolute migration time and thus such identification to be made. **Figure 4.14** demonstrates the separation of phosphorylated and non-phosphorylated PKB from Jurkat cell lysate. Twenty-five cells were separated over the course of 310 seconds for an analysis rate of ~5 cells/min. The absolute migration times of phosphorylated and non-phosphorylated substrates were 1.80±0.06s and 2.03±0.05s respectively. This initial result will, however, need to be confirmed with additional experiments. In the future, results from the addition of multiple kinases and the effects of the addition of agonists/antagonists/inhibitors/stimulators of kinases will be reported using this microfluidic setup at the single cell level.

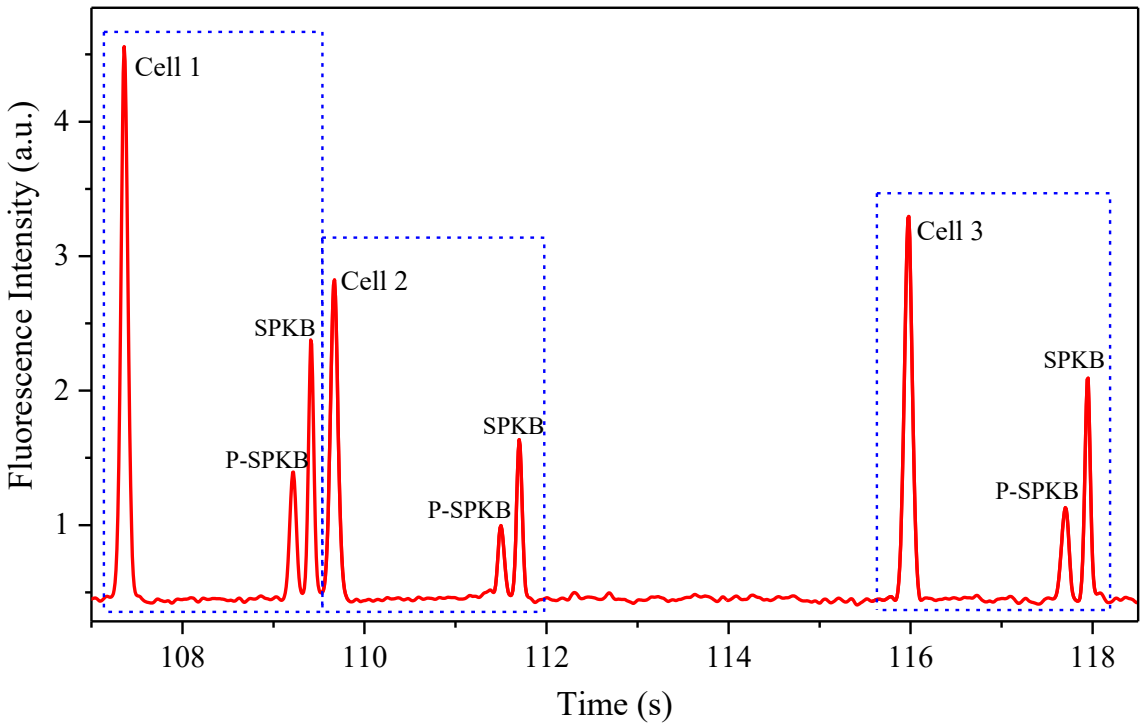

Figure 4.14: **Electropherogram of PKB and p-PKB substrates released from single T-lymphocytes. Intact cells were detected by fiber at ZDP and PKB and p-PKB substrates were detected 2mm downstream of the separation channel.**

4.5 Conclusions

The two-layer microfluidic device reported above allowed the detection of hundreds of single cells in short time period (<15 min). Two detection points were established at any two points of interest using an out-of-plane multimode optical fiber bridge that transmitted both excitation and emission light two ways. The detection distances were easily changed without modifying the microfluidic manifold. The two points of interests were excited simultaneously with a single excitation (488nm) source and detected with a single photomultiplier tube. With this design the absolute migration times for cell lysates were measured. This allowed the determination of migration time drift, lysate injection efficiency, band broadening, and separation efficiency; parameters that could not be

determined easily previously. In addition to providing the ability to better monitor and evaluate separation characteristics, this setup could be applied to a variety of other analytical applications including monitoring the velocity of particles, cells or droplets in microfluidic systems. As an example of such an application, the separation of phosphorylated and nonphosphorylated kinase substrate peptides from single cell lysates was reported.

Chapter 5 - Out-of-Plane Integration of a Multimode Optical Fiber for Single Particle/Cell detection at Multiple Points on a Microfluidic Device with Applications to Particle/Cell Counting, Velocimetry, Size Discrimination and the Analysis of Single Cell Lysate Injections

The majority of this chapter is reproduced by permission of the Royal Chemical Society.

Published as: Jalal Sadeghi, Damith E.W. Patabadige, Anne H Culbertson, Hamid Latifi, and Christopher T Culbertson*

Lab Chip, ***2017***. *17*, 145-155.

5.1 Introduction

Interest in microfluidic devices for the analysis of cells and particles continues to increase due, in large part, to the flexibility in being able to design the channel manifold to perform a variety of operations on the cells as they are transported through the channels.[141,142,143,2] Often, this transport is controlled through the generation of pressure differentials in the channels which creates a hydrodynamic flow. The flow profile in the channel, therefore, is parabolic in nature with the highest flow velocity in the center of the channel and the lowest velocity along the walls.[144] Cells or particles are, therefore, transported at different velocities depending upon their axial location in the channel. These velocity differences can cause issues and uncertainties with the transport and manipulation of particles/cells in these devices. Therefore, simple, inexpensive and easy-to-implement methods to characterize the exact nature of this flow and to monitor it in real time, could substantially improve the ability to track, transport, and manipulate particles/cells in

microfluidic devices. Such capabilities are especially relevant in flow cytometry techniques where cell sorting, cell counting, cell trapping and cell lysis operations are implemented.[2,1,145] Many different techniques to measure cell velocities on microfluidics devices have been developed.[146,147] For example, particle image velocimetry (PIV) is used for real-time deformability cytometry[148] or for the direct measurement of velocity fields in experimental systems.[149] A specially designed optical space–time coding method using a spatially patterned mask has also been reported for determining cell velocity.[150,151] The mask modulates the optical forward scattering or fluorescent emission propagating toward the detectors. Cell tracking information has also been obtained using a mathematical signal processing algorithm from time-domain modulated signals.[151] Finally, the creation of a structured light intensity pattern without using a patterned mask has been used to measure cell velocities. For this method a spatial light modulator (SLM) was used in place of a patterned optical mask.[152,153] In addition to velocity information, several of these methods can also be used to determine the average size of the cells/particles.[154,155,156] Both theoretical and experimental studies have revealed a correlation between equilibrium position/velocity of cells/particles in the channels and their size as a function of channel cross section geometry, flow profiles and Reynolds numbers regimes.[157,158] While useful, these optical detection methods are difficult to implement, mathematically complex and/or the spatial distance needed between particles to avoid interference is relatively large. For simple velocimetry measurements creating 2 detection spots in close proximity (i.e. < 1mm) to measure cell velocity is difficult and requires the use of multiple detectors. Therefore a simpler, less expensive method to obtain this information would be highly useful.[150]

We recently reported a method to incorporate 2 detection points in close proximity on a microfluidic device using an optical fiber bridge.[159] In this system, light was focused into a

microfluidic channel to form one detection point using an epi-illumination system. A short length of optical fiber was inserted 30μm above the channel at this detection point. The focused light from the epi-illumination system was also coupled into the fiber. The other end of the fiber was placed at another location 30μm above a channel in the channel manifold. The light from the fiber then created a second excitation spot in the channel, and thus a second detection point, using only one excitation source and one detector. While the system could create 2 detection spots in close proximity (~1-2 mm) for velocity determinations, an even closer set of detection points was desired. In addition, the excitation spot size (118μm) was larger than desired and limited the spatial resolution. In order to decrease the distance between the detection spots and create narrower excitation lines, a rarely used optical fiber light propagation method has been employed and will be reported in this chapter. As explained in more detail below, tunneling modes were created in a multimode optical fiber resulting in a ring of excitation light emanating from the end of the fiber. When this fiber was placed above the channel, 2 excitation lines were formed as shown in **Figure 5.1**. These lines were narrow (~8μm wide) and only ~110μm apart. The velocities of cells and particles passing through the 2 points could easily be determined. In comparison to the methods mentioned above, cell/particle excitation-emission using an out-of-plane multimode optical fiber (OP-MMF) has several advantages. First, the high spatial resolution generated by the narrow (~8μm) excitation lines can significantly decrease particle/cell detection overlap problems. This is in contrast to other methods such as the spatially patterned mask that has a detection length of 980 μm and thus requires a much larger spatial separation of particles in the channels.[151] Second, a high signal to noise ratio (S/N) is generated from the concentrated excitation beam intensity, and the narrow field of view of the fluorescence collection minimizes environmental stray light. Third, the OP-MMF detection point can be moved easily, compared to the use of *in situ* fabricated fixed

planer waveguides.[160,161,162,163,164] Fourth, the functionally rectangular excitation beam of the OP-MMF, in comparison to the focused circular beams of a microscopic epi-illumination system, can cover the whole channel width. Finally, the OP-MMFs have low light attenuation, have high throughput data handling capacities, are flexible, and are cost effective.

In actuality, with this system, 3 detection points are created as the end of the fiber into which the excitation light was coupled was situated above a detection point also (**Figure 5.1 b-d**). With this optical setup the efficiency of cell lysis and the efficiency of cell lysate injection were determined in a microfluidic single cell analysis device. As cells enter the lysis intersection they are axially distributed throughout the channel cross section. As such, they will have different velocities due to the parabolic nature of the hydrodynamic flow. These varying velocities mean that the time over which the cell is exposed to the electric field used to lyse the cell will also vary. If the cells enter the lysis intersection too quickly they are either not lysed or only partially lysed, as their interaction time with the electric field is limited. This can result in partial injections of the cellular content and thus can generate misleading results and conclusions because of the biased nature of the injections. This 3 detection point technique allows one to characterize the maximum velocity that a cell can enter into the intersection and still be completely lysed and the lysate completely injected. This technique can be used to characterize the flow in a microfluidic manifold, or be employed in any experiment in order to provide real-time feedback on how well the system is functioning.

In this chapter the theory behind the optical fiber tunneling mode is developed and the usefulness of this light propagation mode to create two closely spaced excitation lines is shown. With this OP-MMF configuration, the velocity distributions for 3 different sizes of particles were measured and a correlation between particle size and the average particle velocity was developed. Lastly,

using this device, the relationship between the cell velocity entering the lysis intersection and the efficiency of cell lysis and lysate injection into a separation channel was demonstrated.

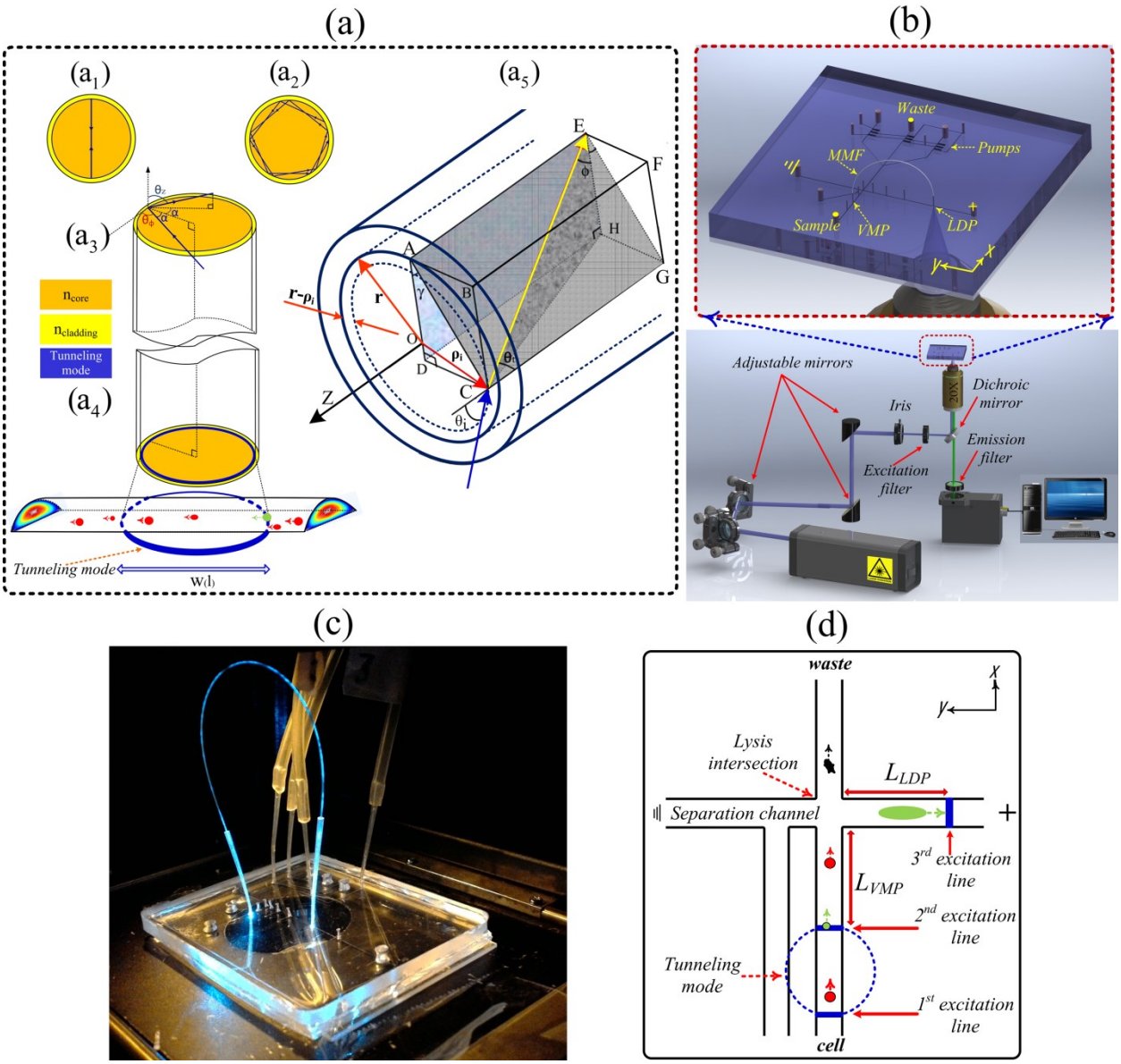

Figure 5.1: (a) Ray paths within a MMF, (a_1) a bound ray, (a_2) a tunneling ray, (a_3) a tunneling ray showing all angles including α, θ_φ, and θ_z, (a_4) a covered channel by a tunneling mode with the beam diameter w(l) at a position l, (a_5) tunneling ray formation at the position ρ_i on a propagation plane (b) Schematic diagram of the optical setup with details and magnified microfluidic chip integrated with MMF. (c) Photograph of a chip integrated with MMF and four inlets to actuate the peristaltic pumps. (d) Schematic of the lysis intersections for the microchip design shown in (b) and (c), showing the three excitation lines and important points and distances.

5.1.1 Characterization of the Optical Fiber Light Modes

According to optical waveguide theory, optical modes in a waveguide can be divided into two classes: guiding modes (bound rays) and leaky modes (refracting rays).[165] Guiding modes propagate along the waveguide via total internal reflection (TIR), while leaky modes completely disappear within an extremely short distance. However, in cylindrical multimode waveguides, such as large core multimode optical fibers (MMF), a third class of modes arise that are distinct from both guiding and leaky modes; these modes are called tunneling modes (i.e. tunneling rays).[166] A MMF can propagate light via hundreds of guiding modes and the interference of these modes at the fiber output usually generates a random speckle pattern (**Figure 5.2a)**.[153] However, under specific optical conditions when laser light is focused into MMF input, tunneling modes can be excited and travel to the other end of the fiber resulting in a ring-like output pattern as illustrated in **Figure 5.2c.**

The general ray paths and mode regions valid for all rays propagating along the MMF can be defined by the spherical polar angles θ_φ and θ_z, where angle θ_φ is the azimuthal propagation angle and θ_z represents the longitudinal propagation angle, i.e. the angle between the ray and the optical axis. Bound rays are only defined by θ_z while tunneling rays are defined by both θ_φ and θ_z. Unlike bound rays, which are confined within the critical angle, θ_c, given by $0 \leq \theta_z < \theta_c$, tunneling rays are confined within the ranges given by $\theta_c \leq \theta_z \leq \pi/2$ and $\alpha_c \leq \alpha \leq \pi/2$ where $\alpha_c = \sin^{-1}(n_{cladding}/n_{core})$, $\theta_c = \cos^{-1}(n_{cladding}/n_{core})$ where the angle of incidence, α, is depicted in **Figure 5.1 (a_3)** and given by $\cos\alpha = \sin\theta_z \sin\theta_\varphi$. In contrast to bound rays which cross the fiber axis (**Figure 5.1 (a_1)**), tunneling rays never cross the fiber axis (**Figure 5.1 (a_2)**).[167]

In general, tunneling rays have larger losses than bound rays, but under certain conditions the overall power detected at the fiber end may be in the same range as that for bound rays. More

details about, characteristics properties of tunneling rays including their excitation power and signal attenuation were discussed and mathematically derived by Dr. Jalal Sedeghi (Laser and Plasma Institute, Teheran, Iran).[168] In this chapter, we show how the tunneling rays can be used as the dominant excitation rays in comparison to bound rays with application to single cell measurements in microfluidic devices.

5.2 Experimental

5.2.1 Reagents and Materials.

Dow corning Sylgard 184 silicone elastomer kits were purchased from Ellsworth adhesives (Germantown, WI). SU-8 2010 photoresist was obtained from MicroChem (Westborough, MA). AZ P4620 photoresist was acquired from AZ Electronic Materials (Branchburg, NJ). Silicon wafers (100 mm P(100) 1-10 ohm-cm SSP 500um Prime Grade single side polished) were purchased from University Wafer (Boston, MA). 6-Carboxyfluorescein diacetate (6-CFDA, ~95%) was obtained from Sigma-Aldrich (Saint Louis, MO). Yellow-Green fluorescent polystyrene latex microbeads (5, 7 and 10 μm) were purchased from Magsphere Inc. (Pasadena, CA). Deionized water was generated using 18 Mohm Millipore Synthesis A10 system (Billerica, MA, USA). A length of multimode optical fiber (0.22 NA, core Ø105 μm) was acquired from Thorlabs Inc. (Newton, NJ).

5.2.2 Cell Culturing

T-lymphocytes obtained from Clone E6-1 cell line (ATCC TIB-152 American Type Culture Collection, Rockville, MD, USA) were cultured as described previously.[18]

5.2.3 Microchip Fabrication

The two-layer PDMS microchip was fabricated as previously reported.[18] Briefly, master molds for the microfluidic channel manifold and the microvalve/pump manifold were created using AZ-P 4620 photoresist and SU8-2010 photoresist, respectively. The micropump manifold was molded in a 5 mm thick layer of 5:1 PDMS, and the microfluidic channel layer was molded in a 50µm thick layer of 30:1 PDMS separately. The micropump control valves were 22µm high and the effective surface area between the pump and channel layer was 100µm × 200µm. The channels in the bottom layer were 18µm high. The gap between micropumps and fluidic channels was 32µm. Detailed dimensions of the device are given in the supplementary information.

5.2.4 Optical Detection System and Generation of Optical Fiber Tunneling Modes

A 105/125-µm multimode fiber (MMF) (Thorlabs FG105UCA, N.A. = 0.22) was used to generate tunneling modes with a uniform irradiance distribution.[167] As illustrated in **Figure 5.1(b)**, several optical elements (i.e. elliptical mirrors and an iris diaphragm) were used to direct the beam into the rear port of a commercial inverted Nikon TS-100 microscope (Nikon Instruments, Inc., Melville, NY) and control the incidence angle (α) of the rays into the optical fiber. A 20X microscope objective (NA=0.45) and Z-axis control (i.e. focusing knob) were used to control the laser spot size of a laser beam. Also, the stage upon which the microchip sat was equipped with a translational controller knob to adjust the optical incidence position ($\rho_i^2 = X^2+Y^2$) at the MMF end face. The objective lens had an effective working distance of 7.4 mm with focal length of 9 mm. The beam with a diameter of 8 µm was focused into the incident point (on the separation channel) with the following characteristics of $40 \le \rho_i < 52.5$, $78^o \le \alpha < 90^o$, $11.5^o \le \theta_z < 90^o$.

The fiber was bridged between the velocity measuring point (VMP) in the cell handling channel and the lysate detection point (LDP) in the separation channel. As shown in **Figure 5.1(c**), a few

millimeter long pipette tip was used as a clamp in order to hold the ends of the optical fibers in place and to adjust the X, Y and Z positions of the both ends of the MMF's relative to the channels as previously described.[159] Over the 1cm length of the nozzle, the cone diameter tapered from 1mm down to 300μm which was suitable for fiber clamping. The excitation source was a 488nm line from a multiline argon-ion laser (MellesGriot Laser Group, Carlsbad, CA). The focused excitation beam from the 20X microscope objective could be easily coupled into the bridged fiber at the LDP. The fiber then transmitted the excitation light via tunneling to create the VMP. The tunneling mode and microchannel junction made two uniform light-lines that perpendicularly covered the channel width (**Figures 5.1(a$_4$) and 5.1(d**)).

At the VMP, intact fluorescently labeled cells could be excited two times at shown in **Figure 5.1d**. resulting in two sharp emission spikes (**Figure 5.2e**). After the cell was lysed at the intersection, the lysate was electrophoretically injected into the separation channel and the fluorescently labeled substrate electrophoretically transported down the separation channel, where the third focused beam excited the cell lysate (LDP) and caused the third emission spike (**Figure 5.4 a-c**). Two sharp emission spikes due to the fiber's backward collection, and the third emission spike were all detected by the same photomultiplier tube (Hamamatsu Instruments, Bridgewater, NJ) attached to the trinocular port of the microscope.

5.2.5 Sample Preparation

Jurkat cells were loaded with 6-Carboxyfluorescein diacetate (6-CFDA) as previously reported.[18] Briefly, 50 μL of 2 mM 6-CFDA in a DMSO stock solution was aliquoted and introduced into a cell culture flask such that the final concentration of the fluorescent dye was 50 μM. Cells were then incubated for 20 min at 37℃ in a 5% CO_2 environment. After incubation, the cells were

centrifuged for 3 min at 2000rpm. The supernatant was then removed and the cell pellet was resuspended in a warm, sterile PBS solution. The centrifugation/resuspension process was repeated two more times to minimize the fluorescent background from the non-loaded dye.

The fluorophore (carboxyfluorescein diacetate; CFDA) was used to label cells. This species is cell permeable and non-fluorescent in nature. After passively diffusing onto the cells, the CFDA is hydrolysed by intracellular esterases and the fluorescent product (carboxyfluorescein; CF) is formed. All live cells are labeled. Due to the hydrophilic nature of the product, it is trapped inside the cells and stable for significant time period (> 1hr) as previously reported.[18]

Five, 7 and 10μm diameter green fluorescent (480/501nm) polystyrene latex beads (Magsphere Inc., Pasadena, CA) were separately prepared in 10mM sodium borate solutions such that the final concentration of each solution was 1x 10^4 beads/mL. Also, a mixture of each size of beads was prepared in same manner such that concentration of each type was 3 x 10^3 beads/mL.

5.2.6 Microchip Operation – Bead Experiments

All of the microfluidic channels were filled with 10mM sodium borate solution at pH = 7.2. A sample of polystyrene beads was placed in the sample reservoir. Fluid flow between the sample reservoir and the waste reservoir was generated using the 3 peristaltic pumps that were integrated with the three parallel fluidic channels.[18] Stable and consistent hydrodynamic flow was generated using multilayer soft lithographic valves integrated into the device. This device has been previously characterized in terms of long-term stability and flow rates and showed no experimentally measurable changes in flow over a > 80 min time period while continuously pumping cells.[18] In addition, when flow rate changes were introduced intentionally, the flow rates were reproducible for a given actuation frequency and pressure, and they could be controlled precisely over a wide range of particle/cell velocities.

5.2.7 Microchip Operation – Cell experiments

Single cell manipulation was performed as previously reported.[18] Briefly, all of the fluidic channels were filled with a separation buffer that contained 2% BSA (w/v), 20% acetonitrile (v/v), 40mM sodium borate, 2mM SDS and 0.2% tween 20 (w/v). Fluorescently labeled Jurkat cells were introduced into sample reservoir. Single cells were then driven towards waste reservoirs using the peristaltic pumps at an average flow rate of 5nL/s. As each cell reached the lysing intersection, they were automatically lysed with a constant electric field (~700V/cm) that was applied across the 5cm long separation channel. The flow rate was finely adjusted so that cell debris were rejected towards waste reservoir and charged fluorescently labeled analytes were injected into the separation channel. The intact cell was detected just prior to lysing using the fiber bridge (zero detection point), and the lysate was detected 2 mm downstream of the lysis intersection directly using the epi-illuimination system.

5.3 Results and Discussion

5.3.1 Particle Velocimetry

Particle velocimetry is based on the measurement of the velocity (V) of a particle between 2 detection points. In other words, the velocity of a cell is acquired by dividing the distance between the two points (W_l) by the time elapsed between the two recorded signals (Δt), i.e. $V=W_l/\Delta t$ where, W_l is defined as the external diameter of the expanded tunneling mode at the mid-plane of the channel. According to the beam divergence principle, [128] the beam diameter at a position l, as shown in **Figure 5.1 (a_4),** can be found from

$$W_l = w_0\left[1+(\frac{\lambda l}{\pi {w_0}^2})^2\right]^{1/2} \tag{5.1}$$

where, w_0 is the initial beam (i.e. core) diameter (w_0=105 μm). As described in the theoretical section, light can be propagated using tunneling modes through the fiber based upon the azimuthal and longitudinal angles of incidence. By adjusting the incidence parameters as defined in the theoretical section, most of the central guiding modes were converted to tunneling modes without a significant reduction of the excitation power. We have utilized a near-field technique to check the intensity expansion of tunneling modes at various incident conditions. A 3-D rendered view of the near-field image of a generated guiding mode (**Figure 5.2(a**)), a guiding-tunneling mode (**Figure 5.2(b)**), and a steep tunneling mode (**Figure 5.2(c**)) are shown. The light exiting the fiber can be used to excite fluorescently labeled particles in a channel twice if the fiber is significantly larger than the channel width. For the results reported below, the channel width was 50 μm and the distance between the two excitation lines as obtained from Eq 9 was 118 μm. In fact, the two excitation beams act as rectangular excitation lines at two points along the channel. As such they can be used to detect and measure the velocity of a particle or cell at any point axially along the width of the channel. This is illustrated in **Figures 5.2(c and d)**. In **Figure 5.2c** two dashed lines are shown that indicate the center line and one edge of a channel. Cross-sections of the light exciting the optical fiber at these two points along the channel width are shown in **Figure 5.2d**. As can be seen in the **Figure 5.2d**, the excitation points for particles/cells transported through the central(black) and lateral(blue) points in the channel are the same within the measurement precision of the technique. The transport of each cell/particle through the excitation points results in two steep fluorescent signals which are modulated in time (**Figure 5.2(e)**). This excitation setup provides an advantage over previous cytometry velocity techniques, as in those techniques some cells pass through different positions relative to the focal point of the excitation spot or may miss the excitation profile entirely[169] (because excitation diameter is much smaller than the channel

width). In our case, cells can be detected across the entire channel width and depth (i.e. Y and Z axes with negligible excitation intensity differences).

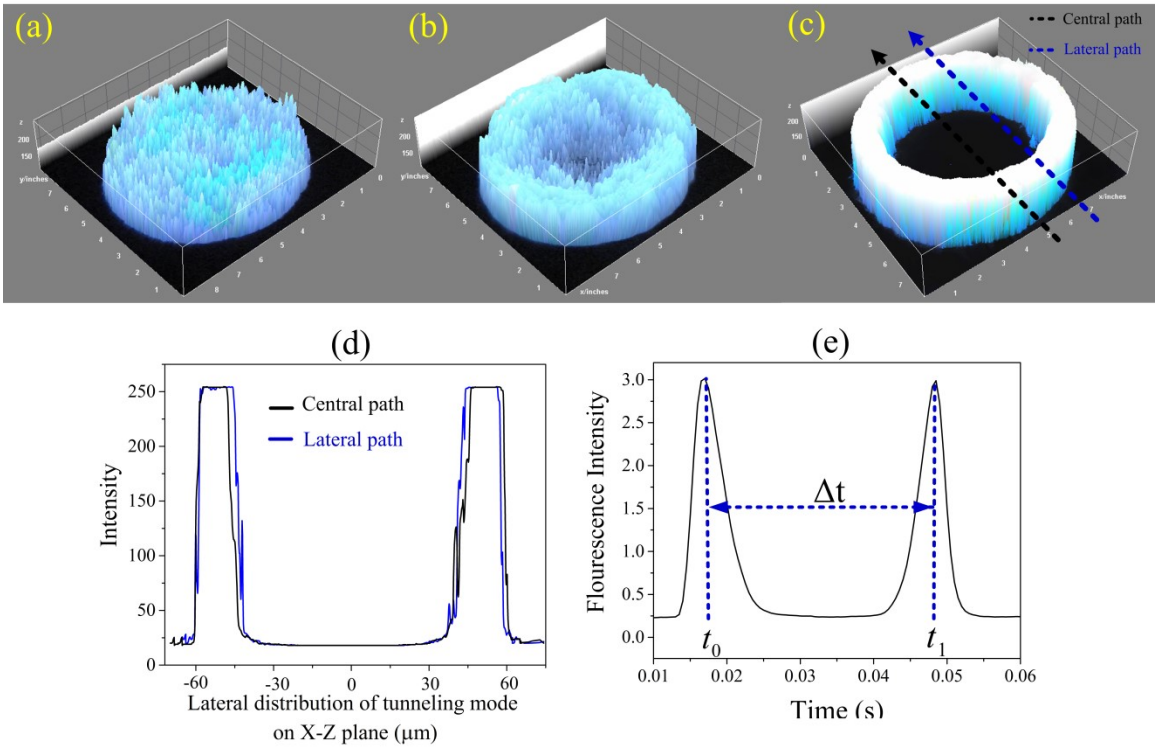

Figure 5.2: The 3-D rendered view of the near-field pattern of generated guiding (a), guiding –tunneling (b), and tunneling mode (c). The horizontal intensity profile of the tunneling mode for central (black) and lateral (blue) path of the particles (d), Fluorescence intensity profile of a 10 μm bead under a tunneling mode excitation (e).

As performed in our previous work[159] the collection efficiency of the emitted light into the fiber bridge at the ZDP which was calculated to be ~94% while the actual coupling efficiency for the fiber was determined to be 45 ± 5%. Unlike the coupling efficiency, the ratio of effective excitation intensities depends on the optical modes. According to the optical dispersion principle, the 105μm multimode fiber used in the experiments reported here produced expanded light spots with diameter of 118 μm at the mid-plane of the microfluidic channel, which was ~45 μm from the end of the fiber. Based on the modal field distribution, for the same input power, the ratio of the

effective excitation intensity between guiding ($I_{eff(G)}$) and tunneling ($I_{eff(T)}$) modes can be derived as,

$$\frac{I_{eff(T)}}{I_{eff(G)}} = \frac{A_{eff(G)}}{A_{eff(T)}} \tag{5.2}$$

where $A_{eff(T)}$ and $A_{eff(G)}$ are the effective cross-sections of the light modes at the mid-plane of the fluidic channel. Here the $A_{eff(G)}$ was ~ 8.7×10^{-3} mm^2 and $A_{eff(T)}$ for the experimentally measured ~8 μm ring width obtained was ~ 2.4×10^{-3} mm^2. Using this equation, the effective excitation intensity ratio was determined to be ~ 3.6. As such tunneling modes have a greater capacity than guiding modes to contribute excitation power and receive fluorescent signal tunneled back from the sample.

5.3.2 Determination of Particle Size and Velocity

The ability of the tunneling optical fiber bridge detection setup to both determine particle size and velocity was examined using fluorescently labeled polystyrene particles of different sizes. The initial assay was performed using a suspension of particles that were 5, 7, and 10 μm in diameter at approximately equal concentrations. As shown in **Figure 5.3(a)**, the fluorescent signals can be divided easily into three groups based upon the size of the fluorescent beads. The relative standard deviations (RSDs) for the 5, 7, and 10 μm diameter beads were determined to be 5.1%, 6.9%, and 7.8%, respectively. These values were close to the RSD values of 10% reported by the manufacturer and most likely a more accurate assessment of the size distribution for the particular batches used.

The minimum interval between cells/particles/samples that can be distinguished using the tunneling excitation and detection scheme can be determined using the resolution equation, R_s

$=\Delta t/4\sigma$. [5] In this equation Δt is the time difference between two particles passing between the excitation lines from the fiber optic, σ is the average standard deviation of the width of the two spikes, and 4σ is used as the baseline width of a spike. For the experiment reported in Fig 5.3, the average baseline width of the particles was $4\sigma = 0.0008$ s so the minimum temporal spacing of the cells must be >0.8 ms. In comparison, the minimum spacing between particles for guiding modes is ~4 ms.

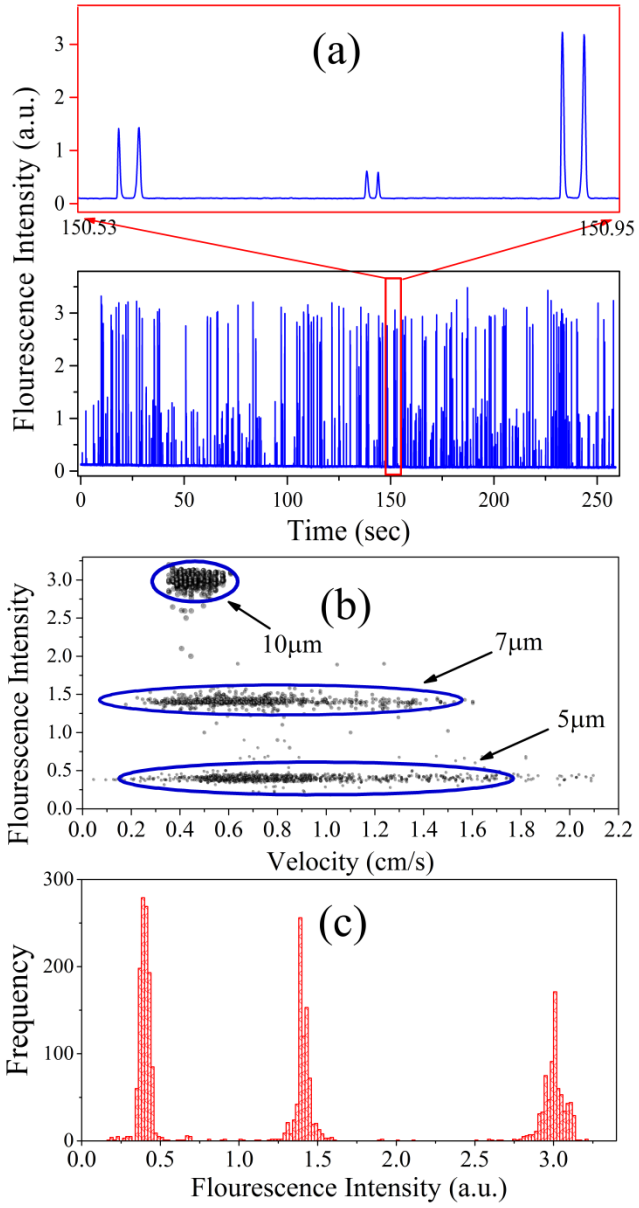

Figure 5.3: (a) Fluorescence signals for the mixture of 10, 7, and 5 µm polystyrene beads. The inset is an expanded view of three fluorescence intensity profiles. (b) Scatter plot for the all particle suspensions. Each data point represents the velocity and the fluorescent intensity of a detected particle. (c) The particle distribution based on the number of fluorescence spikes.

The scatter plot in **Figure 6.3(b)** shows the fluorescent intensity as a function of the velocity of the mixture. For each particle size, the average and standard deviation of the velocity was

determined as well as the spread of the velocities and are reported in **Table 5.1**. The low velocity standard deviation (SD) for the 10 μm population indicated that particle velocities were close to the mean velocity which reflected the confinement of this population to the central portion of the microchannel. In contrast, the high velocity-SD of the 5 μm population indicated that they were spread out over a wider area of microchannel and thus sampled a wider range flow streams in the parabolic fluid flow profile

For many applications of particle velocimetry, the particles used to measure the flow are several orders of magnitude smaller than the channel's dimensions in order not to perturb the flow.[151] The lateral dimensions of the microfluidic channel manifolds used for precisely moving cells/particles, however, are generally only slightly larger than the cells/particles themselves. Under these conditions, the particles significantly affect the flow profile in their proximity. Therefore, larger particles experience more inertial migration, or in other words, the mean velocity of smaller particles is higher. As shown by the results in **Table 5.1**, the mean velocity of particles in microfluidic channels can be utilized to discriminate the various particle populations. The 10 μm population, the 7 μm population and the 5 μm population can be clearly distinguished by means of the measured velocity. The mean velocity of the 10 μm population was 4.5 $mm.s^{-1}$ and thus slower than the 7 μm population with a mean velocity of 6.6 $mm.s^{-1}$ and again slower than the mean velocity of the 5 μm population with 7.2 $mm.s^{-1}$.

Table 5.1: The obtained values of the mean velocity, maximum velocity, SD, and number of particles for each given population

Mean particle diameter	Mean velocity	Maximum velocity	Standard deviation	Particle count
μm	mm s^{-1}	mm s^{-1}	mm s^{-1}	#
10.2	4.5	6.0	0.5	794
7.0	6.6	15.8	2.4	805
5.1	7.2	21.5	3.1	945

5.3.3 Optimization of Cell Lysis and Lysate Injection

In this experiment, the optical fiber bridge was used to create 3 detection points 2 defined by the tunneled light emanating from the optical fiber to measure cell velocity prior to lysis, and one in the separation channel 2 mm downstream of the lysis intersection to detect the injected lysate.

According to the electroporation principle, thousands of nanopores are formed when a cell is exposed to an electric field thus permeabilizing the membrane. If the intensity and duration of the electric field exposure are sufficient, the cell membrane is irreversibly compromised leading to cell lysis. Conversely, if electroporation is generated using low electric fields and short exposure times, the pores can reseal themselves after the field is removed.[46,170]

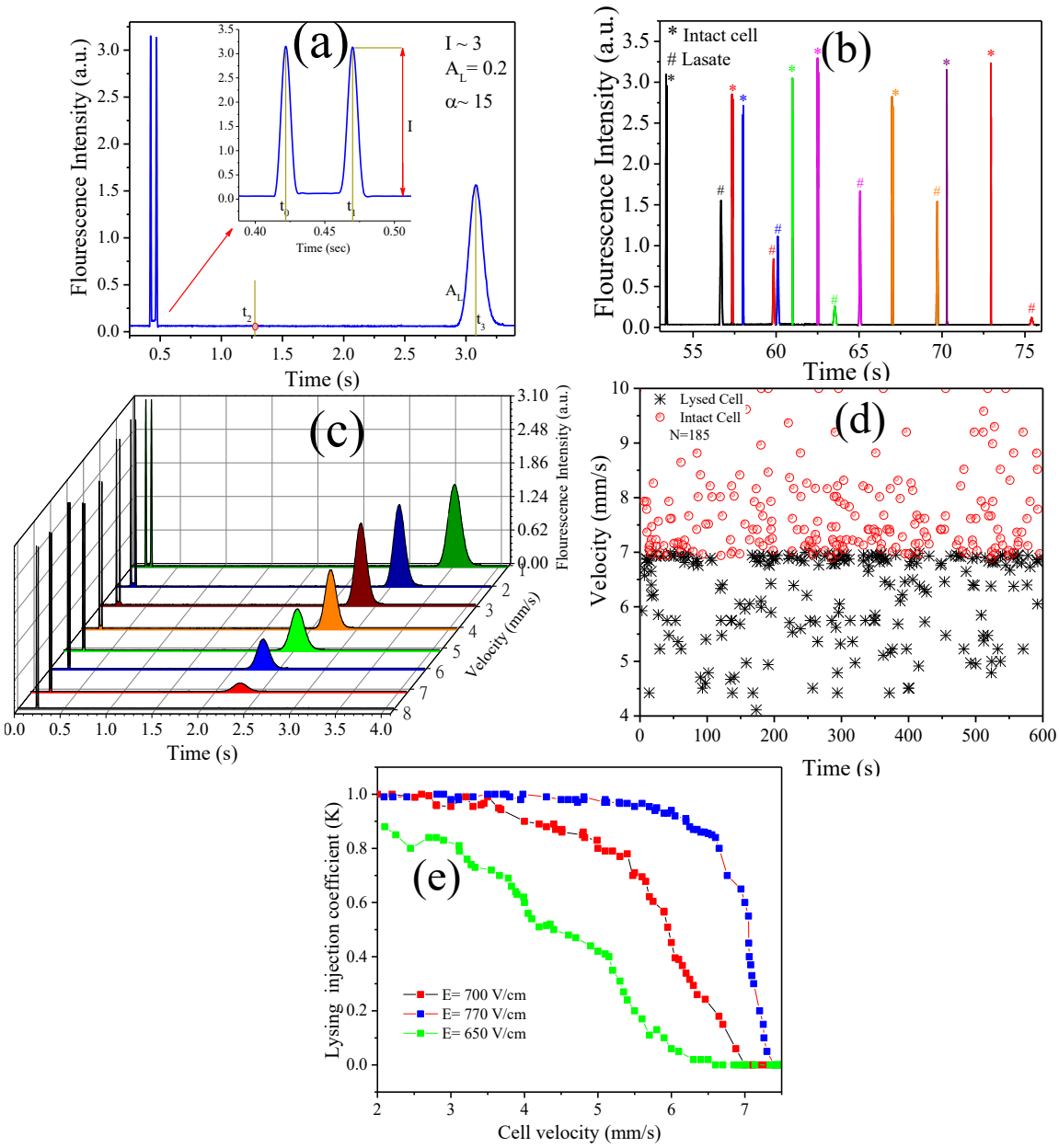

Figure 5.4: (a) and (b) Electropherograms of intact cells 2 mm upstream from the lysis intersection and cell lysate 3mm downstream of the lysis intersection. Each cell produced three peaks. Two narrow peaks appear at t_0 and t_1. A third broader peak appears at t_3. (c) 3-D representation of fluorescence intensity variations of lysate as a function of cell velocity. (d) Separation of 185 cells in velocity interval between 4-10 mm/s to show the critical velocity for an applied electric field of 700 V/cm. (e) Lysing injection coefficient variation as a function of cell velocity for electric field strengths of 650, 700, 770 V/cm.

For this device, the duration of the exposure of the cell to the electric field is determined by the velocity of the cell entering the lysis intersection and, therefore, cell velocity should affect the lysing and lysate injection efficiency. A secondary parameter that also affects cell lysis is cell size,[171] with small cells less susceptible to lysing than large ones under the same electroporation conditions. Both the electric field exposure time (via cell velocity measurements) and cell size effects (via intact cell fluorescence) can be measured using the OP-MMF device. **Figure 5.4(b)** shows typical electropherograms of 8 separated cells obtained from an experiment where hundreds of cells were examined. Three distinct peaks from each cell were easily detected (**Figure 5.4(a)**). Two first sharp peaks (magnified in the inset **Figure 5.4(a)**) are from the intact cell at the VMP as discussed in the previous section for determination of size and velocity. From the information shown in the electropherogram (**Figure 5.4c**) the cell velocity ($V_C=W_1(t_1-t_0)^{-1}$), the absolute migration time of the lysate ($\Delta t_L=t_3-t_2$) and the lysate velocity ($V_L=L_{LDP}(t_3-t_2)^{-1}$) can be determined. Qualitatively, the effect of cell velocity on the efficiency of lysate injection can clearly be seen in **Figure 5.4c**. The electropherograms from the 8 individual cells in this figure are arranged based on the intact cell velocity from 1.1 mm/s to 8 mm/s. These cells were all approximately the same size as judged by their signal at the VDP to eliminate any possible cell size effects.

In order to quantitatively measure the efficiency of injection (K) of the lysate from any cell, the ratio of the amount of the injected lysate (peak area, A_L) at the LDP to the maximum fluorescent signal from the intact cell (I) from the VDP was determined as shown in **Eq 5.3**

$$K= \alpha A_L/I \qquad (5.3)$$

where, α is a coefficient that normalizes the maximum value of A_L/I to 1 as the excitation intensities at the detection points are not the same. Ideally, the ratio of A_L to I should be 1 if cell lysing and lysate injection are complete as seen with cells that enter the lysis intersection at lower

velocities. These cells were completely disintegrated and all the intracellular contents were injected into the separation channel as indicated by a constant maximum K value (**Figure 5.4e)** cells entering the lysis intersection at <4 mm/s at E = 770 V/cm). With increasing cell velocity, however, the amount of the injected lysate (A_L) decreased as shown in **Figure 5.4c**. Cell lysis efficiency (K) as a function of intact cell velocity at electric field strengths of 650, 700, and 770 V/cm is shown in **Figure 5.4(e).** As can be seen in the figure it was not possible to slow the cell velocity down enough for complete lysis/injection to take place at 650 V/cm as K< 0.85 for all velocities examined. As the electric field strength was increased, however, complete lysis and lysate injection (K~0.98±0.02) could be achieved at higher and higher intact cell velocities. At 700V/cm, the critical velocity for complete cell lysing and lysate injection was 3.4±0.2mm/s (**Figures 5.4(d) and 5.4(e)**) and at 770V/cm the critical velocity increased to 5.3±0.2mm/s.

5.4 Conclusion

In this work, a simple, fast and cost effective technique to determine the velocity of particles/cells in a high throughput manner was reported. A microfluidic platform with an integrated 10cm long out-of-plane multimode optical fiber (OP-MMF) was used to create three excitation/detection spots between any two arbitrary points using only a single excitation source and detector. The ability to transmit light through the multimode optical fiber via tunneling modes was utilized to create two excitation/detection lines in the channel at the end of the fiber. These 2 lines were used to monitor particle velocity and determine average particle size. To demonstrate the capability of this system, the velocity and size distributions of 5, 7, and 10 μm fluorescently labeled polystyrene beads were determined. Finally, a third detection point at the end of the fiber, where the excitation light was coupled into the fiber, was used to detect the lysate from the cells whose velocity was

determined at the other end of the fiber. With this design, the absolute migration times for cell lysates were measured. This allowed the characterization of migration time and lysate injection efficiency parameters that could not be previously determined. In the future, this device could be coupled with a variety of integrated and tunable microlenses to more easily generate tunneling modes for better emission, optical trapping, and other optofluidic applications. [161,162,163,164]

References

1. Patabadige, D. E.; Jia, S.; Sibbitts, J.; Sadeghi, J.; Sellens, K.; Culbertson, C. T., Micro Total Analysis Systems: Fundamental Advances and Applications. *Anal Chem* **2016,** *88* (1), 320-38.

2. Culbertson, C. T.; Mickleburgh, T. G.; Stewart-James, S. A.; Sellens, K. A.; Pressnall, M., Micro Total Analysis Systems: Fundamental Advances and Biological Applications. *Anal. Chem. (Washington, DC, U. S.)* **2014,** *86* (1), 95-118.

3. Giddings, J. C., *Unified separation science*. Wiley New York etc: 1991.

4. Heiger, D. N., High performance capillary electrophoresis. **1992**.

5. Jacobson, S. C.; Culbertson, C. T. In *Microfluidics: some basics*, CRC Press LLC: 2006; pp 19-54.

6. Terry, S. C.; Jerman, J. H.; Angell, J. B., A gas chromatographic air analyzer fabricated on a silicon wafer. *Electron Devices, IEEE Transactions on* **1979,** *26* (12), 1880-1886.

7. Unger, M. A.; Chou, H.-P.; Thorsen, T.; Scherer, A.; Quake, S. R., Monolithic microfabricated valves and pumps by multilayer soft lithography. *Science (Washington, D. C.)* **2000,** *288* (5463), 113-116.

8. Bowen, A. L.; Martin, R. S., Integration of on-chip peristaltic pumps and injection valves with microchip electrophoresis and electrochemical detection. *Electrophoresis* **2010,** *31* (15), 2534-2540.

9. Martin, L.; Meier, M.; Lyons, S. M.; Sit, R. V.; Marzluff, W. F.; Quake, S. R.; Chang, H. Y., Systematic reconstruction of RNA functional motifs with high-throughput microfluidics. *Nature Methods* **2012,** *9* (12), 1192-1194.

10. Melin, J.; Quake, S. R., Microfluidic large-scale integration: the evolution of design rules for biological automation. *Annual Review of Biophysics and Biomolecular Structure* **2007,** *36*, 213-231.

11. Park, J. Y.; Kim, D. J.; Kim, S. R.; Baek, J. Y.; Sun, K.; Lee, S. H. In *Microfluidic valve employing the pH-responsive hydrogel microsphere as an actuating element*, Institute of Electrical and Electronics Engineers: 2006; pp 35-38.

12. Sassa, F.; Al-Zain, Y.; Ginoza, T.; Miyazaki, S.; Suzuki, H., Miniaturized shape memory alloy pumps for stepping microfluidic transport. *Sens. Actuators, B* **2012,** *165* (1), 157-163.

13. Landers, J. P.; Begley, M. R.; Ferrance, J. P.; Jones, M. H.; Monahan-Dian, J. Electrostatic actuation for management of flow in micro-total analysis systems (μ-TAS) and related method thereof. WO2006044458A2, 2006.

14. Xie, J.; Shih, J.; Lin, Q.; Yang, B.; Tai, Y.-C., Surface micromachined electrostatically actuated micro peristaltic pump. *Lab Chip* **2004,** *4* (5), 495-501.

15. Walavalkar, S.; Scherer, A. Autonomous electrochemical actuation of microfluidic circuits. WO2009094236A2, 2009.

16. Nie, F.; Sha, J.; Wang, X.; Ye, J. A magnetically responsive micro valve based on microfluidic chip and preparation method thereof. CN103062479A, 2013.

17. Li, M.; Song, Y.; Li, D.; Pan, X. Electromagnetic micro-valve integrated on microfluidic chip. CN103335154A, 2013.

18. Patabadige, D. E. W.; Mickleburgh, T.; Ferris, L.; Brummer, G.; Culbertson, A. H.; Culbertson, C. T., High-throughput microfluidic device for single cell analysis using multiple integrated soft lithographic pumps. *Electrophoresis* **2016,** *37* (10), 1337-1344.

19. Fordyce, P. M.; Diaz-Botia, C. A.; DeRisi, J. L.; Gomez-Sjoberg, R., Systematic characterization of feature dimensions and closing pressures for microfluidic valves produced via photoresist reflow. *Lab Chip* **2012,** *12* (21), 4287-4295.

20. Kartalov, E. P.; Scherer, A.; Quake, S. R.; Taylor, C. R.; Anderson, W. F., Experimentally validated quantitative linear model for the device physics of elastomeric microfluidic valves. *Journal of Applied Physics* **2007,** *101* (6), 064505/1-064505/4.

21. Heath, J. R.; Ribas, A.; Mischel, P. S., Single-cell analysis tools for drug discovery and development. *Nat Rev Drug Discov* **2016,** *15* (3), 204-16.

22. Patabadige, D. E. W.; Jia, S.; Sibbitts, J.; Sadeghi, J.; Sellens, K.; Culbertson, C. T., Micro Total Analysis Systems: Fundamental Advances and Applications. *Anal. Chem. (Washington, DC, U. S.)* **2015**, Ahead of Print.

23. Sun, T.; Kovac, J.; Voldman, J., Image-based single-cell sorting via dual-photopolymerized microwell arrays. *Anal Chem* **2014,** *86* (2), 977-81.

24. Reece, A.; Xia, B.; Jiang, Z.; Noren, B.; McBride, R.; Oakey, J., Microfluidic techniques for high throughput single cell analysis. *Curr Opin Biotechnol* **2016,** *40*, 90-96.

25. Hummer, D.; Kurth, F.; Naredi-Rainer, N.; Dittrich, P. S., Single cells in confined volumes: microchambers and microdroplets. *Lab Chip* **2016,** *16* (3), 447-58.

26. Ocvirk, G.; Salimi-Moosavi, H.; Szarka, R. J.; Arriaga, E.; Andersson, P. E.; Smith, R.; Dovichi, N. J.; Harrison, D. J. In *Single cell enzymatic analysis on a microchip: lysing of single cells and identification of their β-galactosidase activity*, Micro Total Analysis Systems' 98, Springer: 1998; pp 203-206.

27. Chakravarty, A. R.; Kumar, A.; Dixit, A.; Banerjee, S.; Bhattacharyya, A.; Garai, A.; Karande, A. A., Cellular imaging and mitochondria targeted photo-cytotoxicity in visible light by

singlet oxygen using a BODIPY-appended oxovanadium(IV) DNA crosslinking agent. *MedChemComm* **2016**, Ahead of Print.

28. Kang, J. W.; So, P. T.; Dasari, R. R.; Lim, D.-K., High resolution live cell raman imaging using subcellular organelle-targeting SERS-sensitive gold nanoparticles with highly narrow intra-nanogap. *Nano letters* **2015,** *15* (3), 1766-1772.

29. Liu, Z.; Lee, Y.; hee Jang, J.; Li, Y.; Han, X.; Yokoi, K.; Ferrari, M.; Zhou, L.; Qin, L., Microfluidic cytometric analysis of cancer cell transportability and invasiveness. *Scientific reports* **2015,** *5*, 14272.

30. Metto, E. C.; Evans, K.; Barney, P.; Culbertson, A. H.; Gunasekara, D. B.; Caruso, G.; Hulvey, M. K.; Fracassi da Silva, J. A.; Lunte, S. M.; Culbertson, C. T., An integrated microfluidic device for monitoring changes in nitric oxide production in single T-lymphocyte (Jurkat) cells. *Anal Chem* **2013,** *85* (21), 10188-95.

31. Zimmermann, U., *Electrical breakdown, electropermeabilization and electrofusion*. Springer: 1986.

32. Zimmermann, U.; Pilwat, G.; Holzapfel, C.; Rosenheck, K., Electrical hemolysis of human and bovine red blood cells. *The Journal of membrane biology* **1976,** *30* (1), 135-152.

33. Lee, D. W.; Cho, Y.-H., A continuous electrical cell lysis device using a low dc voltage for a cell transport and rupture. *Sens. Actuators, B* **2007,** *124* (1), 84-89.

34. Albritton, N.; Li, G.-p.; Bachman, M.; Sims, C.; Han, F. Fast electrical lysis of cells and rapid collection of the contents thereof using capillary electrophoresis. WO2003093791A2, 2003.

35. Di Carlo, D.; Jeong, K. H.; Lee, L. P., Reagentless mechanical cell lysis by nanoscale barbs in microchannels for sample preparation. *Lab Chip* **2003,** *3* (4), 287-91.

36. Nan, L.; Jiang, Z.; Wei, X., Emerging microfluidic devices for cell lysis: a review. *Lab Chip* **2014,** *14* (6), 1060-1073.

37. Salehi-Reyhani, A.; Gesellchen, F.; Mampallil, D.; Wilson, R.; Reboud, J.; Ces, O.; Willison, K. R.; Cooper, J. M.; Klug, D. R., Chemical-free lysis and fractionation of cells by use of surface acoustic waves for sensitive protein assays. *Anal Chem* **2015,** *87* (4), 2161-9.

38. Li, Z. G.; Liu, A. Q.; Klaseboer, E.; Zhang, J. B.; Ohl, C. D., Single cell membrane poration by bubble-induced microjets in a microfluidic chip. *Lab Chip* **2013,** *13* (6), 1144-50.

39. Chung, J.; Shao, H.; Reiner, T.; Issadore, D.; Weissleder, R.; Lee, H., Microfluidic Cell Sorter (μFCS) for On-chip Capture and Analysis of Single Cells. *Adv. Healthcare Mater.* **2012,** *1* (4), 432-436.

40. Han, X.; van Berkel, C.; Gwyer, J.; Capretto, L.; Morgan, H., Microfluidic Lysis of Human Blood for Leukocyte Analysis Using Single Cell Impedance Cytometry. *Anal. Chem. (Washington, DC, U. S.)* **2012,** *84* (2), 1070-1075.

41. Wu, M.; Piccini, M.; Koh, C.-Y.; Lam, K. S.; Singh, A. K., Single cell microRNA analysis using microfluidic flow cytometry. *PLoS One* **2013,** *8* (1), e55044.

42. Li, L.; Wang, Q.; Feng, J.; Tong, L.; Tang, B., Highly sensitive and homogeneous detection of membrane protein on a single living cell by aptamer and nicking enzyme assisted signal amplification based on microfluidic droplets. *Analytical chemistry* **2014,** *86* (10), 5101-5107.

43. Rao, L.; Cai, B.; Yu, X.-L.; Guo, S.-S.; Liu, W.; Zhao, X.-Z., One-step fabrication of 3D silver paste electrodes into microfluidic devices for enhanced droplet-based cell sorting. *AIP Advances* **2015,** *5* (5), 057134.

44. Türkcan, S.; Nguyen, J.; Vilalta, M.; Shen, B.; Chin, F. T.; Pratx, G.; Abbyad, P., Single-Cell Analysis of [18F] Fluorodeoxyglucose Uptake by Droplet Radiofluidics. *Analytical chemistry* **2015,** *87* (13), 6667-6673.

45. Muñoz-Berbel, X.; Rodríguez-Rodríguez, R.; Vigués, N.; Demming, S.; Mas, J.; Büttgenbach, S.; Verpoorte, E.; Ortiz, P.; Llobera, A., Monolithically integrated biophotonic lab-on-a-chip for cell culture and simultaneous pH monitoring. *Lab on a Chip* **2013,** *13* (21), 4239-4247.

46. McClain, M. A.; Culbertson, C. T.; Jacobson, S. C.; Allbritton, N. L.; Sims, C. E.; Ramsey, J. M., Microfluidic devices for the high-throughput chemical analysis of cells. *Anal. Chem.* **2003,** *75* (21), 5646-5655.

47. Phillips, K. S.; Lai, H. H.; Johnson, E.; Sims, C. E.; Allbritton, N. L., Continuous analysis of dye-loaded, single cells on a microfluidic chip. *Lab Chip* **2011,** *11* (7), 1333-1341.

48. Kovarik, M. L.; Shah, P. K.; Armistead, P. M.; Allbritton, N. L., Microfluidic Chemical Cytometry of Peptide Degradation in Single Drug-Treated Acute Myeloid Leukemia Cells. *Anal. Chem. (Washington, DC, U. S.)* **2013,** *85* (10), 4991-4997.

49. Jiang, D.; Sims, C. E.; Allbritton, N. L., Microelectrophoresis platform for fast serial analysis of single cells. *Electrophoresis* **2010,** *31* (15), 2558-2565.

50. Kovarik, M. L.; Dickinson, A. J.; Roy, P.; Poonnen, R. A.; Fine, J. P.; Allbritton, N. L., Response of single leukemic cells to peptidase inhibitor therapy across time and dose using a microfluidic device. *Integr. Biol.* **2014,** *6* (2), 164-174.

51. Zhao, S.; Li, X.; Liu, Y.-M., Integrated Microfluidic System with Chemiluminescence Detection for Single Cell Analysis after Intracellular Labeling. *Anal. Chem. (Washington, DC, U. S.)* **2009,** *81* (10), 3873-3878.

52. Zhao, S.; Huang, Y.; Liu, Y.-M., Microchip electrophoresis with chemiluminescence detection for assaying ascorbic acid and amino acids in single cells. *J. Chromatogr. A* **2009,** *1216* (39), 6746-6751.

53. Hellmich, W.; Pelargus, C.; Leffhalm, K.; Ros, A.; Anselmetti, D., Single cell manipulation, analytics, and label-free protein detection in microfluidic devices for systems nanobiology. *Electrophoresis* **2005,** *26* (19), 3689-3696.

54. Fu, A. Y.; Chou, H.-P.; Spence, C.; Arnold, F. H.; Quake, S. R., An integrated microfabricated cell sorter. *Analytical Chemistry* **2002,** *74* (11), 2451-2457.

55. Araci, I. E.; Quake, S. R., Microfluidic very large scale integration (mVLSI) with integrated micromechanical valves. *Lab on a Chip* **2012,** *12* (16), 2803-2806.

56. Thorsen, T.; Maerkl, S. J.; Quake, S. R., Microfluidic large-scale integration. *Science* **2002,** *298* (5593), 580-584.

57. Kim, S.; Streets, A. M.; Lin, R. R.; Quake, S. R.; Weiss, S.; Majumdar, D. S., High-throughput single-molecule optofluidic analysis. *Nature Methods* **2011,** *8* (3), 242-245.

58. Munce, N. R.; Li, J.; Herman, P. R.; Lilge, L., Microfabricated System for Parallel Single-Cell Capillary Electrophoresis. *Anal. Chem.* **2004,** *76* (17), 4983-4989.

59. Ling, Y.-Y.; Yin, X.-F.; Fang, Z.-L., Simultaneous determination of glutathione and reactive oxygen species in individual cells by microchip electrophoresis. *Electrophoresis* **2005,** *26* (24), 4759-4766.

60. Kim, H. S.; Devarenne, T. P.; Han, A., A high-throughput microfluidic single-cell screening platform capable of selective cell extraction. *Lab on a Chip* **2015,** *15* (11), 2467-2475.

61. Dickinson, A. J.; Meyer, M.; Pawlak, E. A.; Gomez, S.; Jaspers, I.; Allbritton, N. L., Analysis of sphingosine kinase activity in single natural killer cells from peripheral blood. *Integr Biol (Camb)* **2015,** *7* (4), 392-401.

62. Gao, N.; Li, L.; Shi, Z.; Zhang, X.; Jin, W., High-throughput determination of glutathione and reactive oxygen species in single cells based on fluorescence images in a microchannel. *Electrophoresis* **2007,** *28* (21), 3966-3975.

63. Cole, M. C.; Desai, A. V.; Kenis, P. J. A., Two-layer multiplexed peristaltic pumps for high-density integrated microfluidics. *Sens. Actuators, B* **2011,** *151* (2), 384-393.

64. Davis, J. M.; Giddings, J. C., Statistical theory of component overlap in multicomponent chromatograms. *Anal. Chem.* **1983,** *55* (3), 418-24.

65. Sung, Y.; Tzur, A.; Oh, S.; Choi, W.; Li, V.; Dasari, R. R.; Yaqoob, Z.; Kirschner, M. W., Size homeostasis in adherent cells studied by synthetic phase microscopy. *Proc. Natl. Acad. Sci. U. S. A.* **2013,** *110* (41), 16687-16692,S16687/1-S16687/4.

66. Ignarro, L. J.; Buga, G. M.; Wood, K. S.; Byrns, R. E.; Chaudhuri, G., Endothelium-derived relaxing factor produced and released from artery and vein is nitric oxide. *Proc Natl Acad Sci U S A* **1987,** *84* (24), 9265-9.

67. Bogdan, C., Nitric oxide and the immune response. *Nat. Immunol.* **2001,** *2* (10), 907-916.

68. Kamendi, H.; Dergacheva, O.; Wang, X.; Huang, Z.-G.; Bouairi, E.; Gorini, C.; Mendelowitz, D., NO Differentially Regulates Neurotransmission to Premotor Cardiac Vagal Neurons in the Nucleus Ambiguus. *Hypertension* **2006,** *48* (6), 1137-1142.

69. Das, S.; Kumar, K. N., Nitric oxide: its identity and role in blood pressure control. *Life Sci.* **1995,** *57* (17), 1547-56.

70. Ally, A.; Maher, T. J. In *Nitric oxide: its influence on neurotransmission within the ventrolateral medulla and on cardiovascular responses during static exercise following stroke*, Transworld Research Network: 2010; pp 155-178.

71. Schwentker, A.; Vodovotz, Y.; Weller, R.; Billiar, T. R., Nitric oxide and wound repair: role of cytokines? *Nitric Oxide* **2002,** *7* (1), 1-10.

72. Jiang, M.-Y.; Chen, J.; Wang, J.; Xiao, F.; Zhang, H.-H.; Zhang, C.-R.; Du, D.-S.; Cao, Y.-X.; Shen, L.-L.; Zhu, D.-N., Nitric oxide modulates cardiovascular function in the rat by activating adenosine A2A receptors and inhibiting acetylcholine release in the rostral ventrolateral medulla. *Clin. Exp. Pharmacol. Physiol.* **2011,** *38* (6), 380-386.

73. Zhang, R.-w.; Shen, D.; Sun, W.-w.; Wang, Y.-k.; Bai, J.; Yuan, W.-j.; Wang, W.-z., Multi-effect of central nitric oxide on cardiovascular activity. *Dier Junyi Daxue Xuebao* **2012,** *33* (7), 718-720.

74. Boetker, H. E.; Moeller, N., On NO-the continuing story of nitric oxide, diabetes, and cardiovascular disease. *Diabetes* **2013,** *62* (8), 2645-2647.

75. Green, S. J.; Keefer, L. K. Encapsulated and non-encapsulated nitric oxide generators used as antimicrobial agents. US5814666A, 1998.

76. Tupurani, M. A.; Padala, C.; Kumar, R. G.; Puranam, K.; Kumari, S.; Rani, S. H., Oxidative stress/nitrosative stress in breast cancer. *Int. J. Anal. Bio-Sci.* **2013,** *1* (1), 14-20.

77. Zhao, B., Nitric oxide in neurodegenerative diseases. *Front. Biosci.* **2005,** *10* (1), 454-461.

78. Chazan, D. J.; Parikh, B. R.; Flaherty, B. P.; Anvar, D. J.; Awabdy, B. A. Analyzer for nitric oxide in exhaled breath with multiple-use sensor. EP2237031A2, 2010.

79. Yang, Q.; Zhang, X.; Bao, X.; Lu, H.; Zhang, W.; Wu, W.; Miao, H.; Jiao, B., Single cell determination of nitric oxide release using capillary electrophoresis with laser-induced fluorescence detection. *J. Chromatogr. A* **2008,** *1201* (1), 120-127.

80. Gunasekar, P. G.; Kanthasamy, A. G.; Borowitz, J. L.; Isom, G. E., Monitoring intracellular nitric oxide formation by dichlorofluorescin in neuronal cells. *J. Neurosci. Methods* **1995,** *61* (1,2), 15-21.

81. Zhang, X.; Yang, Q.; Zhang, W.; Hui, Y.; Jiang, P.; Yu, H.; Cai, Y.; Jiao, B. In *Monitoring nitric oxide release in single cells by capillary electrophoresis with laser-induced fluorescence detection*, Monduzzi Editore: 2008; pp 184-189.

82. Yao, D.; Vlessidis, A. G.; Evmiridis, N. P.; Evangelou, A.; Karkabounas, S.; Tsampalas, S., Luminol chemiluminescence reaction: a new method for monitoring nitric oxide in vivo. *Anal. Chim. Acta* **2002,** *458* (2), 281-289.

83. Zhou, L.; Zhang, L.; Liang, G.; Zhou, Y.; Hao, Q., Dynamic monitoring of nitric oxide in vivo release procedure in rats following administration of sodium nitroprusside by Luminol-H2O2 chemiluminescence system. *Huazhong Keji Daxue Xuebao, Yixueban* **2003,** *32* (4), 378-380.

84. Hensley, K.; Kotake, Y.; Moore, D. R.; Sang, H.; Reinke, L. A. In *Real-time, in-vivo measurement of nitric oxide using electron paramagnetic resonance spectroscopic analysis of biliary flow*, Humana Press Inc.: 2003; pp 201-206.

85. Linares, E.; Nakao, L. S.; Augusto, O.; Kadiiska, M. B., EPR studies of in vivo radical production by lipopolysaccharide: potential role of iron mobilized from iron-nitrosyl complexes. *Free Radical Biol. Med.* **2003,** *34* (6), 766-773.

86. Hetrick, E. M.; Schoenfisch, M. H., Analytical chemistry of nitric oxide. *Annu. Rev. Anal. Chem.* **2009,** *2*, 409-433.

87. Bedioui, F.; Quinton, D.; Griveau, S.; Nyokong, T., Designing molecular materials and strategies for the electrochemical detection of nitric oxide, superoxide and peroxynitrite in biological systems. *Phys. Chem. Chem. Phys.* **2010,** *12* (34), 9976-9988.

88. Huang, W.-H.; Ai, F.; Wang, Z.-L.; Cheng, J.-K., Recent advances in single-cell analysis using capillary electrophoresis and microfluidic devices. *J. Chromatogr. B: Anal. Technol. Biomed. Life Sci.* **2008,** *866* (1-2), 104-122.

89. Kikura-Hanajiri, R.; Martin, R. S.; Lunte, S. M., Indirect Measurement of Nitric Oxide Production by Monitoring Nitrate and Nitrite Using Microchip Electrophoresis with Electrochemical Detection. *Anal. Chem.* **2002,** *74* (24), 6370-6377.

90. Fischer, D. J.; Hulvey, M. K.; Regel, A. R.; Lunte, S. M., Amperometric detection in microchip electrophoresis devices: Effect of electrode material and alignment on analytical performance. *Electrophoresis* **2009,** *30* (19), 3324-3333.

91. Hunter, R. A.; Privett, B. J.; Henley, W. H.; Breed, E. R.; Liang, Z.; Mittal, R.; Yoseph, B. P.; McDunn, J. E.; Burd, E. M.; Coopersmith, C. M.; Ramsey, J. M.; Schoenfisch, M. H., Microfluidic amperometric sensor for analysis of nitric oxide in whole blood. *Anal Chem* **2013,** *85* (12), 6066-72.

92. Mainz, E. R.; Gunasekara, D. B.; Caruso, G.; Jensen, D. T.; Hulvey, M. K.; Fracassi da Silva, J. A.; Metto, E. C.; Culbertson, A. H.; Culbertson, C. T.; Lunte, S. M., Monitoring intracellular nitric oxide production using microchip electrophoresis and laser-induced fluorescence detection. *Analytical Methods* **2012,** *4* (2), 414.

93. Droge, W., Free radicals in the physiological control of cell function. *Physiol. Rev.* **2002,** *82* (1), 47-95.

94. Li, J.-M.; Shah, A. M., Endothelial cell superoxide generation: Regulation and relevance for cardiovascular pathophysiology. *Am. J. Physiol.* **2004,** *287* (5, Pt. 2), R1014-R1030.

95. Liu, G.; Sun, G.; Wang, Y.; Wang, D.; Hu, W.; Zhang, J., Association between manganese superoxide dismutase gene polymorphism and breast cancer risk: a meta-analysis of 17,842 subjects. *Mol. Med. Rep.* **2012,** *6* (4), 797-804.

96. Sousa, T.; Pinho, D.; Morato, M.; Marques-Lopes, J.; Fernandes, E.; Afonso, J.; Oliveira, S.; Carvalho, F.; Albino-Teixeira, A., Role of superoxide and hydrogen peroxide in hypertension induced by an antagonist of adenosine receptors. *Eur. J. Pharmacol.* **2008,** *588* (2-3), 267-276.

97. Uttara, B.; Singh, A. V.; Zamboni, P.; Mahajan, R. T., Oxidative stress and neurodegenerative diseases: a review of upstream and downstream antioxidant therapeutic options. *Curr. Neuropharmacol.* **2009,** *7* (1), 65-74.

98. Ma, Z. A.; Zhao, Z.; Turk, J., Mitochondrial dysfunction and β-cell failure in type 2 diabetes mellitus. *Exp. Diabetes Res.* **2012**, 703538, 11 pp.

99. Warner, H. R., Superoxide dismutase, aging, and degenerative disease. *Free Radical Biol. Med.* **1994,** *17* (3), 249-58.

100. Guzik, T. J.; Korbut, R.; Adamek-Guzik, T., Nitric oxide and superoxide in inflammation and immune regulation. *J. Physiol. Pharmacol.* **2003,** *54* (4), 469-487.

101. Zielonka, J.; Kalyanaraman, B., Hydroethidine- and MitoSOX-derived red fluorescence is not a reliable indicator of intracellular superoxide formation: Another inconvenient truth. *Free Radical Biol. Med.* **2010,** *48* (8), 983-1001.

102. Yamazaki, T.; Kawai, C.; Yamauchi, A.; Kuribayashi, F., A highly sensitive chemiluminescence assay for superoxide detection and chronic granulomatous disease diagnosis. *Trop Med Health* **2011,** *39* (2), 41-5.

103. Felix, C. C.; Hyde, J. S.; Sarna, T.; Sealy, R. C., Melanin photoreactions in aerated media: electron spin resonance evidence for production of superoxide and hydrogen peroxide. *Biochem. Biophys. Res. Commun.* **1978,** *84* (2), 335-41.

104. Mukhopadhyay, P.; Rajesh, M.; Yoshihiro, K.; Hasko, G.; Pacher, P., Simple quantitative detection of mitochondrial superoxide production in live cells. *Biochem. Biophys. Res. Commun.* **2007,** *358* (1), 203-208.

105. Gunasekara, D. B.; Hulvey, M. K.; Lunte, S. M.; Fracassi, d. S. J. A., Microchip electrophoresis with amperometric detection for the study of the generation of nitric oxide by NONOate salts. *Anal. Bioanal. Chem.* **2012,** *403* (8), 2377-2384.

106. Lacher, N. A.; Lunte, S. M.; Martin, R. S., Development of a microfabricated palladium decoupler/electrochemical detector for microchip capillary electrophoresis using a hybrid glass/poly(dimethylsiloxane) device. *Anal. Chem.* **2004,** *76* (9), 2482-2491.

107. Lacher, N. A.; Lunte, S. M.; Martin, R. S., Development of a microfabricated palladium decoupler/electrochemical detector for microchip capillary electrophoresis using a hybrid glass/poly(dimethylsiloxane) device. *Anal Chem* **2004,** *76* (9), 2482-91.

108. Takeuchi, K.; Takehara, K.; Ohuchi, T., Diethyldithiocarbamate, a superoxide dismutase inhibitor, reduces indomethacin-induced gastric lesions in rats. *Digestion* **1996,** *57* (3), 201-209.

109. Yan, X.; Grace, W. K.; Yoshida, T. M.; Habbersett, R. C.; Velappan, N.; Jett, J. H.; Keller, R. A.; Marrone, B. L., Characteristics of Different Nucleic Acid Staining Dyes for DNA Fragment Sizing by Flow Cytometry. *Anal. Chem.* **1999,** *71* (24), 5470-5480.

110. Zielonka, J.; Vasquez-Vivar, J.; Kalyanaraman, B., Detection of 2-hydroxyethidium in cellular systems: a unique marker product of superoxide and hydroethidine. *Nat. Protoc.* **2008,** *3* (1), 8-21.

111. Osbourn, D. M.; Lunte, C. E., Cellulose Acetate Decoupler for On-Column Electrochemical Detection in Capillary Electrophoresis. *Analytical Chemistry* **2001,** *73* (24), 5961-5964.

112. Osbourn, D. M.; Lunte, C. E., On-Column Electrochemical Detection for Microchip Capillary Electrophoresis. *Analytical Chemistry* **2003,** *75* (11), 2710-2714.

113. http://www.fibersystems.com/pdf/whitepapers/Basics-of-Fiber-Optics.pdf.

114. Godin, J.; Chen, C.-H.; Cho, S. H.; Qiao, W.; Tsai, F.; Lo, Y.-H., Microfluidics and photonics for bio-system-on-a-chip: a review of advancements in technology towards a microfluidic flow cytometry chip. *J. Biophotonics* **2008,** *1* (5), 355-376.

115. Tang, S. K. Y.; Stan, C. A.; Whitesides, G. M., Dynamically reconfigurable liquid-core liquid-cladding lens in a microfluidic channel. *Lab Chip* **2008,** *8* (3), 395-401.

116. Baylor, M.-E.; Cerjan, B. W.; Pfiefer, C. R.; Boyne, R. W.; Couch, C. L.; Cramer, N. B.; Bowman, C. N.; McLeod, R. R., Monolithic integration of optical waveguide and fluidic channel structures in a thiol-ene/methacrylate photopolymer. *Opt. Mater. Express* **2012,** *2* (11), 1548-1555.

117. Spicer, D.; McMullin, J. N.; Rourke, H., A multi-layer biochip with integrated hollow waveguides. *J. Micromech. Microeng.* **2006,** *16* (8), 1674-1680.

118. Mogensen, K. B.; Petersen, N. J.; Hubner, J.; Kutter, J. P., Monolithic integration of optical waveguides for absorbance detection in microfabricated electrophoresis devices. *Electrophoresis* **2001,** *22* (18), 3930-3938.

119. McMullin, J. N.; Qiao, H.; Goel, S.; Ren, C. L.; Li, D., Integrated optical measurement of microfluid velocity. *Journal of Micromechanics and Microengineering* **2005,** *15* (10), 1810-1816.

120. Pires, N. M.; Dong, T.; Hanke, U.; Hoivik, N., Recent developments in optical detection technologies in lab-on-a-chip devices for biosensing applications. *Sensors (Basel)* **2014,** *14* (8), 15458-79.

121. Guo, F.; Lapsley, M. I.; Nawaz, A. A.; Zhao, Y.; Lin, S. C.; Chen, Y.; Yang, S.; Zhao, X. Z.; Huang, T. J., A droplet-based, optofluidic device for high-throughput, quantitative bioanalysis. *Anal Chem* **2012,** *84* (24), 10745-9.

122. Remmerbach, T. W.; Wottawah, F.; Dietrich, J.; Lincoln, B.; Wittekind, C.; Guck, J., Oral cancer diagnosis by mechanical phenotyping. *Cancer Res* **2009,** *69* (5), 1728-32.

123. Faigle, C.; Lautenschlager, F.; Whyte, G.; Homewood, P.; Martin-Badosa, E.; Guck, J., A monolithic glass chip for active single-cell sorting based on mechanical phenotyping. *Lab Chip* **2015,** *15* (5), 1267-75.

124. Imai, K.; Okazaki, T.; Hata, N.; Taguchi, S.; Sugawara, K.; Kuramitz, H., Simultaneous multiselective spectroelectrochemical fiber-optic sensor: demonstration of the concept using methylene blue and ferrocyanide. *Anal Chem* **2015,** *87* (4), 2375-82.

125. Proctor, A.; Herrera-Loeza, S. G.; Wang, Q.; Lawrence, D. S.; Yeh, J. J.; Allbritton, N. L., Measurement of protein kinase B activity in single primary human pancreatic cancer cells. *Anal Chem* **2014,** *86* (9), 4573-80.

126. Wang, H.; Udukala, D. N.; Samarakoon, T. N.; Basel, M. T.; Kalita, M.; Abayaweera, G.; Manawadu, H.; Malalasekera, A.; Robinson, C.; Villanueva, D.; Maynez, P.; Bossmann, L.; Riedy, E.; Barriga, J.; Wang, N.; Li, P.; Higgins, D. A.; Zhu, G.; Troyer, D. L.; Bossmann, S. H., Nanoplatforms for highly sensitive fluorescence detection of cancer-related proteases. *Photochem Photobiol Sci* **2014,** *13* (2), 231-40.

127. Nelson, A. R.; Borland, L.; Allbritton, N. L.; Sims, C. E., Myristoyl-based transport of peptides into living cells. *Biochemistry* **2007,** *46* (51), 14771-81.

128. Saleh, B. E.; Teich, M. C.; Masters, B. R., Fundamentals of photonics. *Journal of Biomedical Optics* **2008,** *13* (4), 9901.

129. Niu, J.; Xu, J., Coupling efficiency of laser beam to multimode fiber. *Optics Communications* **2007,** *274* (2), 315-319.

130. Liu, C.; Cui, D.; Chen, X., Development of an integrated direct-contacting optical-fiber microchip with light-emitting diode-induced fluorescence detection. *J Chromatogr A* **2007,** *1170* (1-2), 101-6.

131. Culbertson, C. T.; Jacobson, S. C.; Michael Ramsey, J., Diffusion coefficient measurements in microfluidic devices. *Talanta* **2002,** *56* (2), 365-373.

132. Buzzi, F.; Xu, L.; Zuellig, R. A.; Boller, S. B.; Spinas, G. A.; Hynx, D.; Chang, Z.; Yang, Z.; Hemmings, B. A.; Tschopp, O., Differential effects of protein kinase B/Akt isoforms on glucose homeostasis and islet mass. *Molecular and cellular biology* **2010,** *30* (3), 601-612.

133. Welsh, G.; Hers, I.; Berwick, D.; Dell, G.; Wherlock, M.; Birkin, R.; Leney, S.; Tavare, J., Role of protein kinase B in insulin-regulated glucose uptake. *Biochemical Society Transactions* **2005,** *33* (2), 346-349.

134. Duronio, V., The life of a cell: apoptosis regulation by the PI3K/PKB pathway. *Biochemical Journal* **2008,** *415* (3), 333-344.

135. Scheid, M. P.; Woodgett, J. R., PKB/AKT: functional insights from genetic models. *Nature reviews Molecular cell biology* **2001,** *2* (10), 760-768.

136. Song, G.; Ouyang, G.; Bao, S., The activation of Akt/PKB signaling pathway and cell survival. *Journal of cellular and molecular medicine* **2005,** *9* (1), 59-71.

137. Dickinson, A. J.; Hunsucker, S. A.; Armistead, P. M.; Allbritton, N. L., Single-cell sphingosine kinase activity measurements in primary leukemia. *Anal Bioanal Chem* **2014,** *406* (27), 7027-36.

138. Meredith, G. D.; Sims, C. E.; Soughayer, J. S.; Allbritton, N. L., Measurement of kinase activation in single mammalian cells. *Nature biotechnology* **2000,** *18* (3), 309-312.

139. Nelson, A. R.; Borland, L.; Allbritton, N. L.; Sims, C. E., Myristoyl-based transport of peptides into living cells. *Biochemistry* **2007,** *46* (51), 14771-14781.

140. Bechara, C.; Sagan, S., Cell-penetrating peptides: 20 years later, where do we stand? *FEBS Lett* **2013,** *587* (12), 1693-702.

141. Roper, M. G., Cellular Analysis Using Microfluidics. *Analytical chemistry* **2015,** *88* (1), 381-394.

142. Price, A. K.; Culbertson, C. T., Chemical analysis of single mammalian cells with microfluidics. *Analytical chemistry* **2007,** *79* (7), 2614-2621.

143. Price, A. K.; Paegel, B. M., Discovery in Droplets. *Analytical chemistry* **2015,** *88* (1), 339-353.

144. Sadeghi, J.; Ghasemi, A. H. B.; Latifi, H., A label-free infrared opto-fluidic method for real-time determination of flow rate and concentration with temperature cross-sensitivity compensation. *Lab on a Chip* **2016,** *16* (20), 3957-3968.

145. Piyasena, M. E.; Austin Suthanthiraraj, P. P.; Applegate, R. W., Jr.; Goumas, A. M.; Woods, T. A.; Lopez, G. P.; Graves, S. W., Multinode acoustic focusing for parallel flow cytometry. *Anal Chem* **2012,** *84* (4), 1831-9.

146. Oakey, J.; Applegate Jr, R. W.; Arellano, E.; Carlo, D. D.; Graves, S. W.; Toner, M., Particle focusing in staged inertial microfluidic devices for flow cytometry. *Analytical chemistry* **2010,** *82* (9), 3862-3867.

147. Golden, J. P.; Kim, J. S.; Erickson, J. S.; Hilliard, L. R.; Howell, P. B.; Anderson, G. P.; Nasir, M.; Ligler, F. S., Multi-wavelength microflow cytometer using groove-generated sheath flow. *Lab Chip* **2009,** *9* (13), 1942-50.

148. Otto, O.; Rosendahl, P.; Mietke, A.; Golfier, S.; Herold, C.; Klaue, D.; Girardo, S.; Pagliara, S.; Ekpenyong, A.; Jacobi, A.; Wobus, M.; Toepfner, N.; Keyser, U. F.; Mansfeld, J.; Fischer-Friedrich, E.; Guck, J., Real-time deformability cytometry: on-the-fly cell mechanical phenotyping. *Nat. Methods* **2015,** *12* (3), 199-202.

149. Travagliati, M.; Girardo, S.; Pisignano, D.; Beltram, F.; Cecchini, M., Easy Monitoring of Velocity Fields in Microfluidic Devices Using Spatiotemporal Image Correlation Spectroscopy. *Anal. Chem. (Washington, DC, U. S.)* **2013,** *85* (17), 8080-8084.

150. Wu, T.-F.; Mei, Z.; Lo, Y.-H., Optofluidic device for label-free cell classification from whole blood. *Lab Chip* **2012,** *12* (19), 3791-3797.

151. Sommer, C.; Quint, S.; Spang, P.; Walther, T.; Bassler, M., The equilibrium velocity of spherical particles in rectangular microfluidic channels for size measurement. *Lab Chip* **2014,** *14* (13), 2319-2326.

152. Cizmar, T.; Mazilu, M.; Dholakia, K., In situ wavefront correction and its application to micromanipulation. *Nat. Photonics* **2010,** *4* (6), 388-394.

153. Bianchi, S.; Di Leonardo, R., A multi-mode fiber probe for holographic micromanipulation and microscopy. *Lab Chip* **2012,** *12* (3), 635-639.

154. Chun, B.; Ladd, A. J. C., Inertial migration of neutrally buoyant particles in a square duct: An investigation of multiple equilibrium positions. *Phys. Fluids* **2006,** *18* (3), 031704/1-031704/4.

155. Zeng, L. Interaction between a spherical particle and wall-bounded flows at finite Reynolds number. 2007.

156. Zeng, L.; Najjar, F.; Balachandar, S.; Fischer, P., Forces on a finite-sized particle located close to a wall in a linear shear flow. *Phys. Fluids* **2009,** *21* (3), 033302/1-033302/18.

157. Humphry, K. J.; Kulkarni, P. M.; Weitz, D. A.; Morris, J. F.; Stone, H. A., Axial and lateral particle ordering in finite Reynolds number channel flows. *Phys. Fluids* **2010,** *22* (8), 081703/1-081703/4.

158. Zhou, J.; Papautsky, I., Fundamentals of inertial focusing in microchannels. *Lab Chip* **2013,** *13* (6), 1121-1132.

159. Patabadige, D. E. W.; Sadeghi, J.; Kalubowilage, M.; Bossmann, S. H.; Culbertson, A. H.; Latifi, H.; Culbertson, C. T., Integrating Optical Fiber Bridges in Microfluidic Devices to Create Multiple Excitation/Detection Points for Single Cell Analysis. *Analytical Chemistry* **2016,** *88* (20), 9920-9925.

160. Rodríguez-Ruiz, I.; Ackermann, T. N.; Muñoz-Berbel, X.; Llobera, A., Photonic Lab-on-a-Chip: Integration of Optical Spectroscopy in Microfluidic Systems. *Analytical Chemistry* **2016,** *88* (13), 6630-6637.

161. Seow, Y. C.; Liu, A. Q.; Chin, L. K.; Li, X. C.; Huang, H. J.; Cheng, T. H.; Zhou, X. Q., Different curvatures of tunable liquid microlens via the control of laminar flow rate. *Applied Physics Letters* **2008,** *93* (8), 084101.

162. Seow, Y. C.; Lim, S. P.; Lee, H. P., Micro-light distribution system via optofluidic cascading prisms. *Microfluidics and Nanofluidics* **2011,** *11* (4), 451.

163. Seow, Y. C.; Lim, S. P.; Lee, H. P., Optofluidic variable-focus lenses for light manipulation. *Lab on a Chip* **2012,** *12* (19), 3810-3815.

164. Yang, Y.; Liu, A. Q.; Chin, L. K.; Zhang, X. M.; Tsai, D. P.; Lin, C. L.; Lu, C.; Wang, G. P.; Zheludev, N. I., Optofluidic waveguide as a transformation optics device for lightwave bending and manipulation. *Nat. Commun.* **2012,** *3* (Jan.), 1662/1-1662/7,S1662/1-S1662/4.

165. Snyder, A. W.; Love, J., *Optical waveguide theory*. Springer Science & Business Media: 2012.

166. Ma, J.; Bock, W. J., Dramatic performance enhancement of evanescent-wave multimode fiber fluorometer using non-Lambertian light diffuser. *Opt Express* **2007,** *15* (25), 16457-70.

167. Ma, J.; Bock, W. J.; Cusano, A., Insights into tunnelling rays: outperforming guided rays in fiber-optic sensing device. *Opt Express* **2009,** *17* (9), 7630-9.

168. Sadeghi, J.; Patabadige, D. E. W.; Culbertson, A. H.; Latifi, H.; Culbertson, C. T., Out-of-plane integration of a multimode optical fiber for single particle/cell detection at multiple points on a microfluidic device with applications to particle/cell counting, velocimetry, size discrimination and the analysis of single cell lysate injections. *Lab on a Chip* **2017,** *17* (1), 145-155.

169. Wu, D.; Xu, J.; Niu, L.-G.; Wu, S.-Z.; Midorikawa, K.; Sugioka, K., In-channel integration of designable microoptical devices using flat scaffold-supported femtosecond-laser microfabrication for coupling-free optofluidic cell counting [Erratum to document cited in CA162:267894]. *Light: Sci. Appl.* **2015,** *4* (2), e275.

170. Wang, H.-Y.; Lu, C., Microfluidic chemical cytometry based on modulation of local field strength. *Chem. Commun. (Cambridge, U. K.)* **2006,** (33), 3528-3530.

171. Bao, N.; Le, T. T.; Cheng, J.-X.; Lu, C., Microfluidic electroporation of tumor and blood cells: observation of nucleus expansion and implications on selective analysis and purging of circulating tumor cells. *Integr. Biol.* **2010,** *2* (2-3), 113-120.

Appendix A - Copyright Permissions

1. Copyright Permissions of Figures 1.13 and 1.17.

THE AMERICAN ASSOCIATION FOR THE ADVANCEMENT OF SCIENCE LICENSE TERMS AND CONDITIONS

Feb 26, 2017

This Agreement between Damith Patabadige ("You") and The American Association for the Advancement of Science ("The American Association for the Advancement of Science") consists of your license details and the terms and conditions provided by The American Association for the Advancement of Science and Copyright Clearance Center.

License Number	4056660674242
License date	Feb 26, 2017
Licensed Content Publisher	The American Association for the Advancement of Science
Licensed Content Publication	Science
Licensed Content Title	Monolithic Microfabricated Valves and Pumps by Multilayer Soft Lithography
Licensed Content Author	Marc A. Unger,Hou-Pu Chou,Todd Thorsen,Axel Scherer,Stephen R. Quake
Licensed Content Date	Apr 7, 2000
Licensed Content Volume	288
Licensed Content Issue	5463
Volume number	288
Issue number	5463
Type of Use	Thesis / Dissertation
Requestor type	Scientist/individual at a research institution
Format	Print and electronic
Portion	Figure
Number of figures/tables	2
Order reference number	
Title of your thesis / dissertation	Developing multilayer microfluidic platforms and advancing laser induced fluorescent detection and electrochemical detection to analyze intracellular protein kinases, reactive nitrogen and oxygen species in single cells
Expected completion date	Mar 2017
Estimated size(pages)	180
Requestor Location	Damith Patabadige 1545 International CT M32 MANHATTAN, KS 66502 United States Attn: Damith Patabadige
Billing Type	Invoice
Billing Address	Damith Patabadige 1545 International CT M32 MANHATTAN, KS 66502

2. Copyright Permission for Chapter 2.

JOHN WILEY AND SONS LICENSE TERMS AND CONDITIONS

Feb 12, 2017

This Agreement between Damith Patabadige ("You") and John Wiley and Sons ("John Wiley and Sons") consists of your license details and the terms and conditions provided by John Wiley and Sons and Copyright Clearance Center.

License Number	4046631329265
License date	Feb 12, 2017
Licensed Content Publisher	John Wiley and Sons
Licensed Content Publication	Electrophoresis
Licensed Content Title	High-throughput microfluidic device for single cell analysis using multiple integrated soft lithographic pumps
Licensed Content Author	Damith E. W. Patabadige,Tom Mickleburgh,Lorin Ferris,Gage Brummer,Anne H. Culbertson,Christopher T. Culbertson
Licensed Content Date	Mar 17, 2016
Licensed Content Pages	8
Type of use	Dissertation/Thesis
Requestor type	Author of this Wiley article
Format	Print and electronic
Portion	Full article
Will you be translating?	No
Title of your thesis / dissertation	Developing multilayer microfluidic platforms and advancing laser induced fluorescent detection and electrochemical detection to analyze intracellular protein kinases, reactive nitrogen and oxygen species in single cells
Expected completion date	Mar 2017
Expected size (number of pages)	180
Requestor Location	Damith Patabadige 1545 International CT M32 MANHATTAN, KS 66502 United States Attn: Damith Patabadige
Publisher Tax ID	EU826007151
Billing Type	Invoice
Billing Address	Damith Patabadige 1545 International CT M32 MANHATTAN, KS 66502 United States Attn: Damith Patabadige
Total	0.00 USD
Terms and Conditions	

3. Copyright Permission for Chapter 4.

RightsLink®

Home | Account Info | Help

Title:	Integrating Optical Fiber Bridges in Microfluidic Devices to Create Multiple Excitation/Detection Points for Single Cell Analysis
Author:	Damith E. W. Patabadige, Jalal Sadeghi, Madumali Kalubowilage, et al
Publication:	Analytical Chemistry
Publisher:	American Chemical Society
Date:	Oct 1, 2016

Logged in as: Damith Patabadige
LOGOUT

PERMISSION/LICENSE IS GRANTED FOR YOUR ORDER AT NO CHARGE

This type of permission/license, instead of the standard Terms & Conditions, is sent to you because no fee is being charged for your order. Please note the following:

- Permission is granted for your request in both print and electronic formats, and translations.
- If figures and/or tables were requested, they may be adapted or used in part.
- Please print this page for your records and send a copy of it to your publisher/graduate school.
- Appropriate credit for the requested material should be given as follows: "Reprinted (adapted) with permission from (COMPLETE REFERENCE CITATION). Copyright (YEAR) American Chemical Society." Insert appropriate information in place of the capitalized words.
- One-time permission is granted only for the use specified in your request. No additional uses are granted (such as derivative works or other editions). For any other uses, please submit a new request.

BACK | CLOSE WINDOW

4. Copyright Permission for Chapter 5.

Out-of-plane integration of a multimode optical fiber for single particle/cell detection at multiple points on a microfluidic device with applications to particle/cell counting, velocimetry, size discrimination and the analysis of single cell lysate injections

J. Sadeghi, D. E. W. Patabadige, A. H. Culbertson, H. Latifi and C. T. Culbertson, *Lab Chip*, 2017, **17**, 145
DOI: 10.1039/C6LC01161F